OC SCHEMES FOR INCOMPRESSIBLE VISCOUS FLOWS: APPLICATION AND DEVELOPMENT

by

Jiten C. Kalita

Department of Mathematics

Indian Institute of Technology, Guwahati, INDIA

August 2001


भारतीय प्रौद्योगिकी संस्थान गुवाहाटी
Indian Institute of Technology Guwahati

HOC SCHEMES FOR INCOMPRESSIBLE VISCOUS FLOWS: APPLICATION AND DEVELOPMENT

A Thesis Submitted

for the Award of the Degree of

Doctor of Philosophy

by

Jiten Chandra Kalita

to the

DEPARTMENT OF MATHEMATICS

INDIAN INSTITUTE OF TECHNOLOGY, GUWAHATI

August, 2001


भारतीय प्रौद्योगिकी संस्थान गुवाहाटी
Indian Institute of Technology Guwahati

C E R T I F I C A T E

It is certified that the work contained in the thesis entitled **HOC Schemes for Incompressible Viscous Flows: Application and Development** by **Jiten Chandra Kalita**, a student in the department of Mathematics, Indian Institute of Technology, Guwahati for the award of the degree of Doctor of Philosophy has been carried out under our supervision and that this work has not been submitted elsewhere for a degree.

Dr. Durga Charan Dalal
Assistant Professor
Department of Mathematics
Indian Institute of Technology, Guwahati

Dr. Anoop Kumar Dass
Associate Professor
Department of Mechanical Engineering
Indian Institute of Technology, Guwahati

August 2001

भारतीय प्रौद्योगिकी संस्थान गुवाहाटी
Indian Institute of Technology Guwahati

DEDICATED TO MY MOTHER

for her 3D's,

Determination, Devotion and Discipline.

Acknowledgments

This part of my dissertation has provided me with a rare opportunity of not having to substantiate any of my comments by analytical, numerical or experimental proof. This indeed has come as a breath of fresh air after the tedious, monotonous and machinery ritual of PhD work. However, I assure that it has come from the core of my heart, which I wish, will be treated as a tribute to the people without whom I would have never been able to accomplish the feat of producing a dissertation.

It is quite common and on the expected line to thank the thesis supervisor(s) for his/her (their) support, guidance, and technical advice. Notwithstanding, it is the extraordinary circumstances that they took me under their wings for which I am indebted to both my supervisors Dr. D. C. Dalal and Dr. Anoop K. Dass. I am really grateful to Dr. Dalal for patiently keeping me on the track, and Dr. Dass for imbibing the value of scientific thinking and making me realize my true potential. It was a great learning experience and I thoroughly enjoyed working under them.

Dr. Y. V. S. S. Sanyasiraju, now in the Department of Mathematics, IIT Madras, introduced me to the wonderful intrigues of the Computer World. He deserves a special thank. I am also thankful to Dr. Anupam Dewan and Dr. Subhash C. Misra of Mechanical Engineering Department of IIT Guwahati; to the former for the confidence he imparted on me during the compulsory course that was totally foreign to me and proved very handy in my research later on, and to the latter for his eagerness to extend a helping hand at every opportunity.

I owe a huge debt of gratitude to the present and past members of the IITG Computer Center, especially to Ashok, Prabhakar and Rupa for making me feel at home despite their huge load of work. In the same vein I also thank Kalyan and Pinakeswar, my co-researchers from day one; I still cherish the memory of their enchanting companies. I am also grateful to my friend Dr. Swaroop

Nandan Bora, on whom I leaned many a time for obtaining some valuable papers whenever he was on tour, and which of course he obliged every time without hesitation.

All my family members have immensely contributed towards the smooth completion of my PhD. Their hearty wishes and blessings from the backstage has always been a great moral booster for me. I take this opportunity to convey my gratefulness to my parents whom I am really very proud of. I would also like to thank my elder sisters Bharati, Deepali and Pranita, and my brother-in-laws Mr. Monomohan Medhi and Mr. Tarit Paine for their pampering love and care. The loving encouragements from Mr. Mukul Mahant (Khura), who has been like a father to me has always been a constant source of inspiration. Words are not enough to convey my thanks to him. Special mention must also be made for my father-in-law Dr. Tarakeswar Choudhury; it was his persuasion that pushed me to research, which otherwise I would have never set off to undertake.

Finally, I would like to thank my wife Deepshikha for her love, support, encouragement and patience throughout the period of my PhD work despite her poor health after surviving two near fatal surgeries. Never during this period she complained about the attention she needed the most, which unfortunately, I could not properly provide. I can't thank her enough.

The last two years of this work was supported by the University Grants Commission, India under the Faculty Development Programme in the 9th plane period.

Jiten Chandra Kalita

Indian Institute of Technology
Guwahati

Abstract

This work is concerned with higher-order compact (HOC) schemes for convection-diffusion equations in general and incompressible viscous flows in particular. A fully compact and fully higher-order accurate scheme is developed for the standard buoyancy driven square cavity problem through $O(h^4)$ compact approximation of the derivative source term and zero-gradient temperature boundary conditions of identical accuracy at the adiabatic walls. The scheme produces highly accurate results even for very high laminar Rayleigh numbers for which no other HOC results are seen. The HOC treatment of the derivative source term also opens up new possibilities. A parametrized class of implicit HOC schemes is then developed for the unsteady two-dimensional (2D) convection-diffusion equations. They efficiently capture both transient and steady solutions of linear and nonlinear convection-diffusion equations with Dirichlet as well as Neumann boundary conditions. The results obtained for flows of varying complexities governed by the 2D incompressible Navier-Stokes equations are in excellent agreement with analytical and established numerical results. One of the schemes is then applied to compute double-diffusive natural convection in a vertical porous annulus between two concentric cylinders. This is perhaps the first instance of application of an HOC scheme to flows involving both heat and mass transfer. A transformation-free HOC finite difference scheme is then proposed for the steady 2D convection-diffusion equation on nonuniform Cartesian grids. Apart from avoiding usual computational complexities associated with conventional transformation techniques, the method, for a certain class of problems, computes highly accurate solution with smaller number of grid points with resultant saving of memory and CPU time. In particular it is seen to be very effective in the computation of wall-bounded viscous flows as not only does it compute high-*Re* lid-driven cavity flows very accurately, but also is seen to capture some new flow features. For the backward-facing step flow problem, the method produces solutions which are in much better agreement with experiment compared with other numerical results.

Contents

List of Figures

List of Tables

Nomenclature

a	diffusion coefficient
A	aspect ratio
c	convection coefficient along x-direction
C	Courant number $\left(\frac{c\Delta t}{a}\right)$
d	convection coefficient along y-direction
D	solutal diffusivity
f	forcing function
g	acceleration due to gravity
h	mesh step length in x-direction
H	cavity size (height)
i, j	indices along x- and y-directions respectively
k	mesh step length in y-direction
K	permeability of porous medium
L	Characteristic length
Le	Lewis number $\left(\frac{\alpha}{D}\right)$
n	normal direction
N	buoyancy ratio $\left(\frac{\beta_S(S_h - S_c)}{\beta_T(T_h - T_c)}\right)$
$\overline{Nu}$	the average Nusselt number
$Nu_{\frac{1}{2}}$	the average Nusselt number on vertical mid plane
Nu_0	the average Nusselt number on vertcal wall
Nu_{0max}	the maximum value of the local Nusselt number on vertical wall
Nu_{0min}	the minimum value of the local Nusselt number on vertical wall

Nu_x	Nusselt number at a distance x from the hot wall through any line parallel to y axis
p	pressure
Pe	Peclect number $\left(\frac{ch}{a}\right)$
Pr	Prandtl Number $\left(\frac{\nu}{\alpha}\right)$
$Q(x,y)$	local heat flux in a horizontal direction at any point (x,y)
r	radial co-ordinate
Ra	Rayleigh number $\left(\frac{g\beta_T(T_h - T_c)H^3}{\nu\alpha}\right)$
Re	Reynolds number $\left(\frac{U_0L}{\nu}\right)$
Re_c	Cell Reynolds number $\left(\frac{ch}{a}\right)$
s	source term
S	concentration
S_c, S_h	cold and hot wall concentrations
$\overline{Sh}$	average Sherwood number
t	time
T	temperature
T_c, T_h	cold and hot wall temperatures
T_0	reference temperature
u	horizontal (in Cartesian) or radial (in cylindrical polar co-ordinates) velocity component
v	vertical velocity component in Cartesian co-ordinates
u_{max}	the maximum horizontal velocity at vertical mid plane
U_0	reference velocity
v_{max}	the maximum vertical velocity at horizontal mid plane
w	axial velocity component in cylindrical polar co-ordinates
x, y	Cartesian horizontal and vertical co-ordinates
z	axial cylindrical co-ordinate
α	thermal diffusivity
β_S	coefficient of solutal expansion
β_T	coefficient of thermal expansion
δ_t^+	forward time difference operator

δ_x, δ_y	central difference operators in x- and y-directions respectively
δ_x^+, δ_y^+	forward difference operators in x- and y-directions respectively
δ_x^-, δ_y^-	backward difference operators in x- and y-directions respectively
ϵ	porosity of porous medium
κ	radius ratio
λ	clustering parameter
λ_r	relaxation parameter
μ	weighted average parameter
ν	kinematic viscosity
ρ	density
σ	heat capacity
τ_{ij}	truncation error at the (i, j)th point
ϕ	typical transport variable
ψ, ψ_{mid}	stream-function and its value at mid-point
ω	vorticity

Chapter 1

INTRODUCTION

1.1 Background

Many physical systems, especially those involving fluid flow, are described in terms of mathematical models that include convective and diffusive transport of some variables. These models consist of the governing equations in the form of ordinary or partial differential equations (ODEs or PDEs). As a great number of such model equations like the Navier-Stokes (N-S) equations do not possess analytical solutions, one has to resort to numerical methods. Amongst the popular methods that have been used quite frequently in computational fluid dynamics (CFD) is the finite difference method. Here, the basic methodology involves discretizing the problem domain by setting up a grid (preferably structured) and then approximating the derivatives appearing in the governing equations by difference quotients at each grid point. Such approximation yields a system of algebraic equations which can then be solved with some matrix solution algorithm.

The most common finite difference representation of the derivatives are based on Taylor series expansion of the variables at the grid points. The leading term in the truncation error (TE) of this expansion determines the order of accuracy of the scheme. For example, if this TE is asymptotically proportional to h^m, where h is the distance between two successive grid points, the difference scheme is said to be accurate of order m or shortly $O(h^m)$. The $O(h^2)$ central difference schemes, because of their easy and straight-forwardness in application, have for quite some time been a popular choice for constructing discrete approximations to linear PDEs. Such methods are known to yield quite good results on reasonable meshes if the solution is well behaved. But for certain problems, such as the convection dominated flows, the solution may exhibit oscillatory behaviour if the mesh is not sufficiently refined. However, mesh refinement invariably brings in additional points into the system resulting in an increased system size and consequently more memory and CPU time are required to solve such problems on a computer. Again discretization on a non-compact stencil (generally associated with higher-order accurate methods) increases the band-width of the coefficient matrix. Both mesh refinement and increased matrix band-width ultimately result in increased arithmetic operations. Thus neither a lower-order accurate method on a fine mesh nor a higher-order accurate one on a non-compact stencil could be computationally cost-effective. Therefore, there is a need for the development of schemes which are higher-order accurate and also compact at the same time.

A compact finite difference scheme is one which utilizes grid points located only directly adjacent to the node about which the differences are taken. In addition, if the scheme has an order of accuracy greater than two, it is termed a higher-order compact (HOC) method. The higher-order accuracy of the HOC methods combined with the compactness of the difference stencils yields highly accurate numerical solutions on relatively coarser grids with greater computational efficiency. There exists several mechanisms through which finite difference schemes can achieve higher-order compactness. For example, Gupta *et al.* [26] apply series expansion to the differential equations whereas Dennis and Hudson [20] employ a transformation that involves expanding the exponential of a definite integral of the convective coefficient of the PDE concerned. Some other HOC works that can be cited are the discrete weighted mean approximation approach of Gartland [22], Noye and Tan's [45, 46] weighted modified PDE method, the 4th order compact scheme of Tang and Fornberg [40], and high order upwind schemes of Wilkes [76], Yanwen [78] and Sesterhenn [59].

Another way of obtaining higher-order compactness is by using the original differential equation to substitute for the leading TE terms of the standard central difference approximation. This is the mechanism that has been adopted throughout the present work. This idea was first implemented by Lax and Wendroff [5, 6, 30] on the time dependent hyperbolic PDEs. They used the original PDE to approximate the second-order time derivative in a Taylor series expansion, thus raising the time accuracy from $O(\Delta t)$ to $O[(\Delta t)^2]$. The spatial implementation of this temporal Lax-Wendroff idea was first proposed by Mackinnon and Carey [41]. Similar research was carried out further by Mackinnon and Johnson [42] in order to develop schemes for two-dimensional (2D) steady-state convection-diffusion problems. These schemes maintain high order of accuracy besides exhibiting the property of smoothing artificial oscillations [42]. At about the same time Abarbanel and Kumar [1] independently developed a spatially 4th and temporally 2nd order accurate scheme for the Euler equations. These schemes are similar to those developed by Dukowicz [21] and Wong [77] though they were achieved in a different manner. Recently Spotz and Carey [66,67] have extended the idea of Mackinnon and Johnson [42] to the stream-function vorticity (ψ-ω) formulation of the 2D N-S equations. Some other HOC works are the recent studies in 3D convection-diffusion and Poisson equations by Ananthakrishnaih [4], Spotz and Carey [68], Gupta and Kouatchou [25] and Zhang [79].

1.2 Motivation

A careful study of the works discussed so far reveals a plethora of issues concerning HOC schemes and their applicability to convection-diffusion problems in general and incompressible viscous flows in particular. The merits of HOC schemes discussed earlier do not come for free as existence of higher derivatives is a prerequisite [67]. In this context, it seems important to develop HOC schemes and to examine how the schemes behave when applied to flows involving difficult physics like multiplicity of scales, separated viscous flows at high Reynolds numbers (*Re*'s) etc. Also involved are some interesting numerical linear algebraic issues. For example, the benefits that can be derived from the use of advanced iterative algorithms like Conjugate Gradient (CG), Biconjugate Gradient (BiCG) and hybrid BiCG etc. [37,62] to solve the algebraic equations resulting from HOC discretization is an issue needing attention. Many flows in nature and technology are of convection-diffusion type, many a time involving heat and mass transfer. These flows offer tough challenges to any computational algorithm especially at high Reynolds and Rayleigh numbers, and not much HOC computation for such flows is seen. Thus, work in the development and application of HOC algorithms for these problems is a challenging one and is replete with many interesting possibilities. These are the major motivating factors behind this work.

1.3 Objectives

The main aim of the present work is to develop some HOC finite difference algorithms for the 2D linear and nonlinear convection-diffusion equations with special emphasis to incompressible viscous flows. Also intended to examine is whether some already existing HOC algorithms can be modified and then applied to flow problems to which they were not applied earlier. Another objective is to examine the possibility of broadening the scope of applicability of HOC algorithms to hitherto unexplored problems and situations of heat transfer, fluid flow and mass transfer.

1.4 The Work

First an HOC scheme for the ψ-ω form of the N-S equations [67], in modified form, is applied to the standard steady-state natural convection in a square cavity problem [34]. Apart from developing a 4th order compact Neumann boundary condition for temperature at the adiabatic walls, the derivative source term in the vorticity equation is also approximated compactly up to identical order of accuracy. These new developments, besides getting assimilated easily into the solution procedure also have the potential of being employed to other unexplored situations. The present computation can be called *fully* compact and higher-order accurate as the scheme, boundary conditions and the source term treatment are all fourth order accurate and compact. This is in contrast to perhaps the only example [20] of HOC computation of this problem which uses non-compact boundary condition and lower-order approximation to the derivative source term for the vorticity-equation. The present method is not only robust as evidenced from computations at difficult Rayleigh numbers, but also accurate as is seen from comparisons with reliable existing results.

A class of HOC schemes is then developed for the 2D unsteady convection-diffusion equations with variable convection coefficients [35]. Unlike the earlier HOC schemes [42, 67], the present class of schemes is free from the restrictive condition that the grid aspect ratio has to be unity. These schemes are first or second order accurate in time depending on the choice of a weighted average parameter and 4th order accurate in space. For a certain range of the parameter, the schemes are unconditionally stable. They efficiently compute both transient and steady-state linear and nonlinear convection-diffusion. To bring out different aspects of the schemes, they are used to compute the transient solutions of three 2D linear and nonlinear convection-diffusion problems and the time marching steady solution of the 2D lid-driven cavity flow problem. The results obtained in all four cases are in excellent agreement with the analytical as well as established numerical results. Again one of these schemes, namely, $(9, 9)$ is employed to study the double-diffusive natural convection in a vertical porous annulus. This is perhaps the first instance in which an HOC algorithm has been applied to a heat-mass transfer problem. The results compare very well with numerical results wherever available.

The most significant contribution of this work, however, is the development of an HOC finite difference scheme for the 2D steady-state convection-diffusion on nonuniform grids without transformation [36]. Conventional finite difference methods on nonuniform grids involve transformation between physical and computational space. In a significant departure from this convention, the present method completely eliminates transformation, bringing in remarkable simplicity and efficiency to the solution procedure. Dispensing with transformation brings the additional benefit of decrease in computational effort as the method deals with smaller number of terms at each grid point. Because of clustering, the method is seen to produce accurate solution of complex wall-bounded flows with significantly small number of grid points with resultant economy. For instance, a 31×31 grid is found to be good enough to capture the flow details including the tertiary vortices for the lid-driven cavity problem up to $Re = 1000$. For the same problem, the method accurately computes flows at much higher Re's and reveals some hitherto unreported flow features. Computations are carried out also for the much-examined backward-facing step flow and significantly, the results are much closer to the experimental compared with any other numerical results in literature. Formulations for the scheme are also developed for orthogonal curvilinear co-ordinate systems (see Appendix C).

An important task in CFD is to efficiently solve the sparse linear systems arising from the discretized PDEs. The coefficient matrix resulting from the HOC discretization of the PDEs is not generally diagonally dominant. In situations like this, conventional iterative methods such as Gauss-Seidel cannot be applied to solve the algebraic systems. This problem is circumvented by employing various advanced iterative solvers like Conjugate Gradient (CG) algorithm for the pure diffusion in the uniform formulation and, Biconjugate Gradient (BiCG), Biconjugate Gradient Stabilized (BiCGStab) and hybrid BiCGStab algorithms at other situations. Moreover, for the cases studied, the present HOC discretizations provide matrices that are fairly well-conditioned and hence the complexity of constructing an efficient pre-conditioner is avoided throughout the work.

1.5 Organization of the Thesis

The present dissertation has been arranged in seven chapters. Chapter 2 briefly discusses the theoretical aspects of the HOC methodology for 2D steady-state convection-diffusion in the present context. Chapter 3 describes the fully HOC method and its application to the thermally-driven cavity flow problem. Chapter 4 describes the class of transient HOC schemes developed in details with an analysis of the diffusive and anti-diffusive natures of the schemes, stability analysis and numerous applications. Chapter 5 includes the details of application of the $(9,9)$ scheme developed in Chapter 4 to a heat-mass transfer problem, namely, the double-diffusive natural convection in a vertical porous annulus. Development and application of the HOC finite difference scheme on nonuniform grid without transformation for steady-state 2D convection-diffusion is discussed in Chapter 6. Chapter 7 summarizes and comments on the whole work and discusses scope for future work.

Chapter 2

THEORETICAL ASPECTS OF HOC SCHEMES

This chapter briefly describes the development of HOC schemes [42,66] for 2D steady-state convection-diffusion on uniform grids. The technique employed is the use of the original PDE, as mentioned earlier, to replace some of the derivatives.

2.1 2D Steady-State Convection-Diffusion

The 2D steady-state convection-diffusion equation for a transport variable ϕ on some domain may be written as

$$-a\nabla^2\phi + u(x,y)\frac{\partial \phi}{\partial x} + v(x,y)\frac{\partial \phi}{\partial y} = s(x,y), \tag{2.1}$$

where $a(>0)$ is a constant diffusion coefficient, ∇^2 is the Laplacian operator given by $\nabla^2 = \dfrac{\partial^2}{\partial x^2} + \dfrac{\partial^2}{\partial y^2}$, u and v respectively are the convection velocities in x- and y-directions and s is the source term such as the body force. This equation is representative of almost all the fluid dynamics problems involving the convection and diffusion of many flow variables such as mass, heat, energy, vorticity etc. With proper choice of a, u, v and s, it can also be used to represent the complete steady-state 2D N-S equation.

Non-dimensionalization of the governing equations many a time simplifies the task of flow simulation. This can be accomplished for equation (2.1) by choosing a characteristic length L, a characteristic velocity U_0 and a characteristic value Φ of ϕ (say, for example on the boundary) and letting

$$\phi^* = \frac{\phi}{\Phi}, \quad u^* = \frac{u}{U_0}, \quad v^* = \frac{v}{U_0}, \quad x^* = \frac{x}{L} \quad \text{and} \quad y^* = \frac{y}{L}. \tag{2.2}$$

On omitting the asterisks for the sake of convenience, the non-dimensional convection-diffusion equation can be written as

$$-\nabla^2 \phi + c(x,y)\frac{\partial \phi}{\partial x} + d(x,y)\frac{\partial \phi}{\partial y} = f(x,y), \tag{2.3}$$

where the diffusion coefficient is now set to unity so that the magnitudes of $c(x,y) = \dfrac{U_0 L}{a} u(x,y)$ and $d(x,y) = \dfrac{U_0 L}{a} v(x,y)$ determine the ratio of convection to diffusion and $f(x,y) = \dfrac{L^2}{a\Phi} s(x,y)$ may be called the forcing function. The term $\dfrac{U_0 L}{a}$ is known differently for different fluid flow situations. In most of the viscous fluid dynamics problems it is called the Reynolds number Re and in the field of heat transfer, the Péclect number Pe. This Re or Pe plays a crucial role on the solution procedure as well as the physics of the problems. Throughout the present study, it is assumed that c, d, f and ϕ are sufficiently smooth which paves the way for HOC formulation of the 2D convection-diffusion equation.

2.2 HOC Formulation

In order to construct an HOC formulation for equation (2.3), the solution domain is chosen in such a way that it can be divided into some rectangular sub-regions. Each sub-region is then further divided into uniform meshes of square cells of which each vertex serves as a node and the distance between two successive nodes is h, a constant. If $x_0 \leq x \leq x_m, \quad y_0 \leq y \leq y_n$ is the rectangular domain and $\phi_{ij} = \phi(x_i, y_j) = \phi(x_0 + ih, y_0 + jh)$, the central difference approximation to (2.3) yields

$$-\delta_x^2\phi_{ij} - \delta_y^2\phi_{ij} + c\delta_x\phi_{ij} + d\delta_y\phi_{ij} - \tau_{ij} = f_{ij}, \tag{2.4}$$

where the truncation error is given by

$$\tau_{ij} = \frac{h^2}{12}\left[2\left(c\frac{\partial^3\phi}{\partial x^3} + d\frac{\partial^3\phi}{\partial y^3}\right) - \left(\frac{\partial^4\phi}{\partial x^4} + \frac{\partial^4\phi}{\partial y^4}\right)\right]_{ij} + O(h^4) \tag{2.5}$$

To obtain a fourth order compact formulation for (2.3), each of the derivatives of the leading term of (2.5) are compactly approximated to $O(h^2)$. In order to accomplish this, the original PDE (2.3) is treated as an auxiliary relation that can be differentiated to yield expressions for higher derivatives. For example differentiation of (2.3) yields

$$\frac{\partial^3\phi}{\partial x^3} = -\frac{\partial^3\phi}{\partial x\partial y^2} + c\frac{\partial^2\phi}{\partial x^2} + \frac{\partial c}{\partial x}\frac{\partial\phi}{\partial x} + d\frac{\partial^2\phi}{\partial x\partial y} + \frac{\partial d}{\partial x}\frac{\partial\phi}{\partial y} - \frac{\partial f}{\partial x} \tag{2.6}$$

$$\begin{aligned}\frac{\partial^4\phi}{\partial x^4} &= -\frac{\partial^4\phi}{\partial x^2\partial^2 y} + c\frac{\partial^3\phi}{\partial x^3} + 2\frac{\partial c}{\partial x}\frac{\partial^2\phi}{\partial^2 x} + \frac{\partial^2 c}{\partial x^2}\frac{\partial\phi}{\partial x} + d\frac{\partial^3\phi}{\partial^2 x\partial y}\\ &+ 2\frac{\partial d}{\partial x}\frac{\partial^2\phi}{\partial x\partial y} + \frac{\partial^2 d}{\partial x^2}\frac{\partial\phi}{\partial y} - \frac{\partial^2 f}{\partial x^2}\end{aligned} \tag{2.7}$$

$$\frac{\partial^3\phi}{\partial y^3} = -\frac{\partial^3\phi}{\partial x^2\partial y} + c\frac{\partial^2\phi}{\partial x\partial y} + \frac{\partial c}{\partial y}\frac{\partial\phi}{\partial x} + d\frac{\partial^2\phi}{\partial^2 y} + \frac{\partial d}{\partial y}\frac{\partial\phi}{\partial y} - \frac{\partial f}{\partial y} \tag{2.8}$$

$$\begin{aligned}\frac{\partial^4\phi}{\partial y^4} &= -\frac{\partial^4\phi}{\partial x^2\partial^2 y} + c\frac{\partial^3\phi}{\partial x\partial^2 y} + 2\frac{\partial c}{\partial y}\frac{\partial^2\phi}{\partial x\partial y} + \frac{\partial^2 c}{\partial y^2}\frac{\partial\phi}{\partial x} + d\frac{\partial^3\phi}{\partial y^3}\\ &+ 2\frac{\partial d}{\partial y}\frac{\partial^2\phi}{\partial^2 y} + \frac{\partial^2 d}{\partial y^2}\frac{\partial\phi}{\partial y} - \frac{\partial^2 f}{\partial y^2}\end{aligned} \tag{2.9}$$

Substitution of equations (2.6)-(2.9) into equation (2.5) at the (i,j)th node and some simplifications, yield

$$\tau_{ij} = \frac{h^2}{12}\left[-2\left\{\frac{\partial^4\phi}{\partial x^2\partial y^2} + c\frac{\partial^3\phi}{\partial x\partial y^2} + d\frac{\partial^3\phi}{\partial x^2\partial y} + \left(\frac{\partial c}{\partial y} + \frac{\partial d}{\partial x} - cd\right)\frac{\partial^2\phi}{\partial x\partial y}\right\} + \right.$$

$$
\begin{aligned}
&+ \left(c^2 - 2\frac{\partial c}{\partial x}\right)\frac{\partial^2 \phi}{\partial x^2} + \left(d^2 - 2\frac{\partial d}{\partial y}\right)\frac{\partial^2 \phi}{\partial y^2} - \left(\frac{\partial^2 c}{\partial x^2} + \frac{\partial^2 c}{\partial y^2} - c\frac{\partial c}{\partial x} - d\frac{\partial c}{\partial y}\right)\frac{\partial \phi}{\partial x} \\
&- \left(\frac{\partial^2 d}{\partial x^2} + \frac{\partial^2 d}{\partial y^2} - c\frac{\partial d}{\partial x} - d\frac{\partial d}{\partial y}\right)\frac{\partial \phi}{\partial y} - \left.\left(\frac{\partial^2 f}{\partial x^2} + \frac{\partial^2 f}{\partial y^2} - c\frac{\partial f}{\partial x} - d\frac{\partial f}{\partial y}\right)\right]_{ij} \\
&+ O(h^4) \qquad (2.10)
\end{aligned}
$$

All the derivatives and cross-derivatives appearing in the RHS of (2.10) have $O(h^2)$ approximations. For example

$$
\left.\frac{\partial^4 \phi}{\partial x^2 \partial^2 y}\right|_{ij} = \delta_x^2 \delta_y^2 \phi_{ij} - \frac{h^2}{12}\left[\frac{\partial^6 \phi}{\partial x^4 \partial^2 y} + \frac{\partial^6 \phi}{\partial x^2 \partial^4 y}\right]_{ij} + O(h^4) \qquad (2.11)
$$

The derivatives appearing in the RHS of equation (2.10) are substituted by these $O(h^2)$ approximations following which the fourth order accurate HOC scheme for equation (2.3) becomes

$$
\begin{aligned}
-\alpha_{ij}\delta_x^2\phi_{ij} &- \beta_{ij}\delta_y^2\phi_{ij} + C_{ij}\delta_x\phi_{ij} + D_{ij}\delta_y\phi_{ij} \\
&- \frac{h^2}{6}\left[\delta_x^2\delta_y^2 - c_{ij}\delta_x\delta_y^2 - d_{ij}\delta_x^2\delta_y - \gamma_{ij}\delta_x\delta_y\right]\phi_{ij} = F_{ij}, \qquad (2.12)
\end{aligned}
$$

where δ_x and δ_y are the first and δ_x^2 and δ_y^2 are the second order central difference operators along x- and y-directions respectively and the coefficients α_{ij}, β_{ij}, γ_{ij}, C_{ij}, D_{ij} and F_{ij} are as follows:

$$
\alpha_{ij} = 1 + \frac{h^2}{12}(c_{ij}^2 - 2\delta_x c_{ij}), \qquad (2.13)
$$

$$
\beta_{ij} = 1 + \frac{h^2}{12}(d_{ij}^2 - 2\delta_y d_{ij}), \qquad (2.14)
$$

$$
\gamma_{ij} = \delta_y c_{ij} - c_{ij}d_{ij} + \delta_x d_{ij}, \qquad (2.15)
$$

$$
C_{ij} = c_{ij} + \frac{h^2}{12}(\delta_x^2 + \delta_y^2 - c_{ij}\delta_x - d_{ij}\delta_y)c_{ij}, \qquad (2.16)
$$

$$
D_{ij} = d_{ij} + \frac{h^2}{12}(\delta_x^2 + \delta_y^2 - c_{ij}\delta_x - d_{ij}\delta_y)d_{ij}, \qquad (2.17)
$$

$$
F_{ij} = f_{ij} + \frac{h^2}{12}(\delta_x^2 + \delta_y^2 - c_{ij}\delta_x - d_{ij}\delta_y)f_{ij}. \qquad (2.18)
$$

It is to be noted here that as $p, q \leq 2$ for the terms of the type $\dfrac{\partial^{p+q}\phi}{\partial x^p \partial y^q}$ on the RHS of (2.10), the central difference approximation to those terms do not

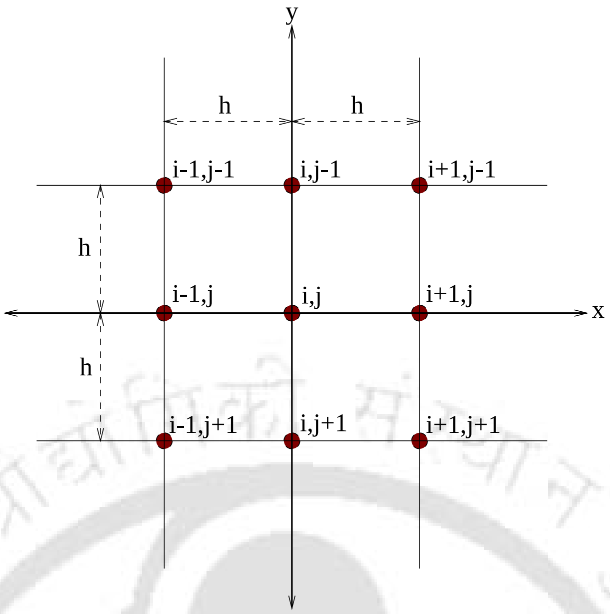

Figure 2.1: The 9-point HOC stencil.

extend beyond one mesh length away from the point about which differences are taken. Therefore, the HOC computational stencil is always restricted to a maximum of nine points as shown in Fig. 2.1. Thus, the sparse coefficient matrix resulting from this HOC discretization is of band-width nine. The issue of using efficient iterative solvers for this system and the related numerical issues will be addressed at appropriate places in the next chapters.

Chapter 3

FULLY COMPACT HIGHER-ORDER SCHEME FOR BUOYANCY DRIVEN CAVITY FLOWS

3.1 Introduction

HOC schemes seen so far for viscous fluid flow problems based on the strategy described in Chapter 2 suffered from some drawbacks. For example, HOC approximation to the source term which appears in derivative form in many problems was not available. Issues such as this are addressed in this chapter giving rise to some new developments. These developments are then combined with an existing HOC scheme for the stream-function-vorticity (ψ-ω) form of the N-S equations to compute the flow in the standard buoyancy driven square cavity [1].

The problem of buoyancy driven square cavity with adiabatic horizontal and differentially heated vertical walls has been the topic of extensive studies in the past few decades. Along with the lid-driven cavity problem, it has become

---

[1] This study has been published in *Physical Review E* [34].

one of the most popular means for testing and validating numerical algorithms and computer codes. Some reasons for this are: (i) its simple geometry with no singularities throughout the cavity except at the corners and (ii) the availability of experimental and numerical data on this problem. The problem is also attractive because of its relevance in varied applications such as nuclear reactor insulation, ventilation of rooms, solar energy collection, crystal growth of liquids, pneumatic transport etc.

Till date, the second order (spatially) accurate schemes, particularly the central difference schemes have been used in a large number of CFD problems because of their straight-forwardness in application. In keeping with this trend, in most of the previous attempts to tackle this problem, the schemes were at most second order accurate in space. Time marching approach was used in majority of the cases [17, 19] to reach the steady-state solution. A second order ADI scheme was used by Wilkes *et al.* [75] to produce results up to a Grashof number of 10^5; De Vahl Davis [18] presented the benchmark solutions for this problem for $Ra = 10^3$ to 10^6 through a second order finite difference scheme and Richardson extrapolation; Chenoweth and Paolucci [14] used an FTCS explicit predictor corrector method, Hortman *et al.* [31] a finite volume multigrid method, and Ramaswamy *et al.* [54] a second order finite element method. The regime of high Rayleigh number was considered by Le Quéré [52] using a second order Chebychev polynomial approach and Janssen and Henkes [32] with a finite volume discretization with fourth order central interpolation scheme for the convective derivatives. Recently Tagawa *et al.* [72] carried out numerical calculations with different schemes including Utopia and Kawamura-Kawahara scheme for low Prandtl number regime. A new pseudo-vorticity-velocity formulation and stream-function-vorticity (ψ-ω) method have also been proposed by Ho *et al.* [29] and Comini *et al.* [16] respectively. In perhaps the only previous example [20] where an HOC method was used for the problem, computation were carried out upto a Rayleigh number of 10^5. The work used $O(h^4)$ discretization of the governing equations, but the boundary treatment was not compact and the derivative source term treatment was not higher order accurate. The present work computes the laminar solution of the problem starting with a moderate value of $Ra = 10^3$ and going upto a value as high as 10^7 (with Boussinesq approximation, the flow becomes unstable at an Ra very close to 2×10^8 [14, 52]) with the fourth order accurate HOC scheme described in Chapter 2. The temperature gradient source term in the vorticity equation is also discretized using a $O(h^4)$ compact scheme and smoothly integrated to the solution procedure. This strategy seems to have the potential of being usefully employed in similar situations, especially, to the pressure gradient term in the extension of HOC to the primitive variable formulation of the N-S equations. Also, the boundary conditions for vorticity and temperature are compact and $O(h^4)$. In particular a compact temperature Neumann boundary condition has been developed adopting a novel approach. Because of compactness and higher order accuracy, this treatment may be taken as the model for similar computations. Thus unlike the previous attempts, the present method is fully compact and fully higher order accurate with associated advantages. Another attractive feature of the computation is the use of CG [37] and hybrid BiCGStab [62] algorithms for solving the linear algebraic equations and this improves the convergence behaviour of the algorithm. As expected, the results are very accurate and even coarse grid results compare very well with previous computations. Overall, besides opening up new possibilities, the method may be considered an efficient one for computation of flow for this physical configuration.

3.2 The Problem

The problem considered here is the 2D incompressible steady-state flow of a Boussinesq fluid of Prandtl number (Pr) 0.71 in an upright square cavity of side H (Figure 3.1). Both the vertical walls are isothermal; the left wall at temperature T_h is hotter than the right wall at temperature T_c. Both the horizontal walls are insulated. Natural convection starts owing to the temperature difference between the left and right walls. Body forces are present in the form of gravitational force which acts in the negative y-direction. The

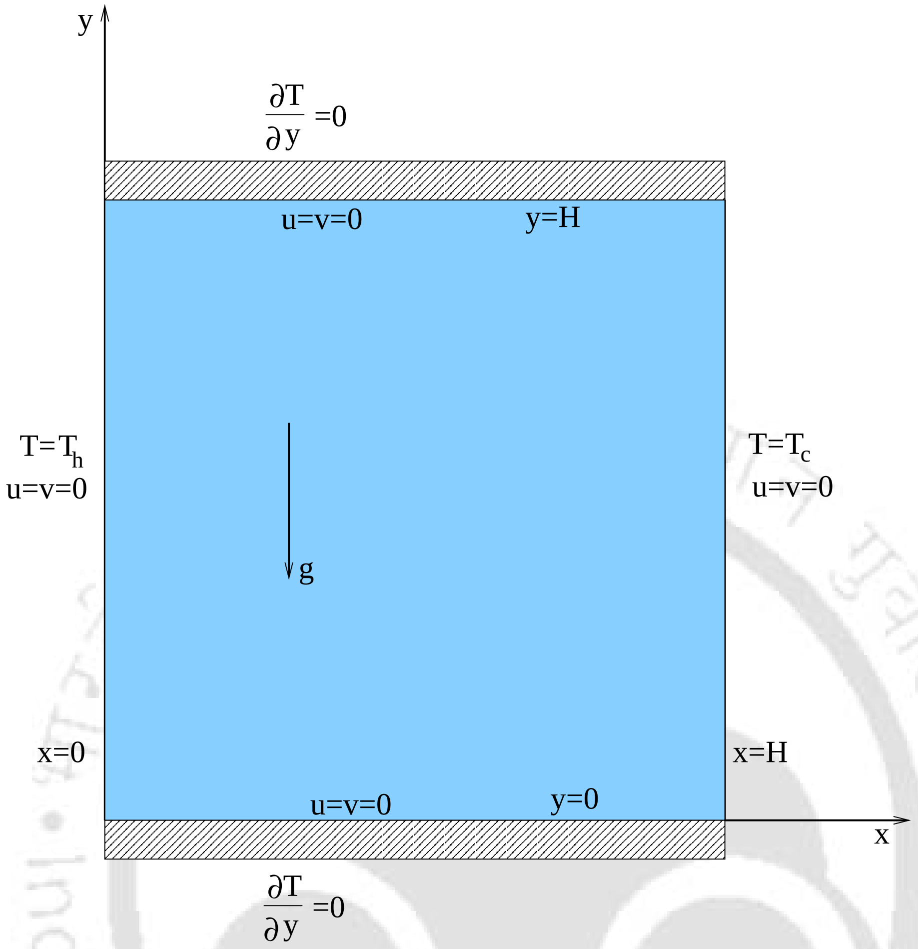

Figure 3.1: *Schematic view of the differentially heated square cavity.*

governing equations of the problem can be written as:

$$\frac{\partial u}{\partial x}+\frac{\partial v}{\partial y}=0, \tag{3.1}$$

$$u\frac{\partial u}{\partial x}+v\frac{\partial u}{\partial y}=-\frac{1}{\rho}\frac{\partial p}{\partial x}+\nu\nabla^2 u, \tag{3.2}$$

$$u\frac{\partial v}{\partial x}+v\frac{\partial v}{\partial y}=-\frac{1}{\rho}\frac{\partial p}{\partial y}+g\beta_T(T-T_0)+\nu\nabla^2 v, \tag{3.3}$$

$$u\frac{\partial T}{\partial x}+v\frac{\partial T}{\partial y}=\alpha\nabla^2 T, \tag{3.4}$$

where u, v, T, ρ, p, ν, α and β_T are the velocity components along x- and y-axes, temperature, density, pressure, kinematic viscosity, thermal diffusivity and the coefficient of thermal expansion of the fluid respectively. T_0 is a reference temperature, g is the acceleration due to gravity and $\nabla^2 \equiv \frac{\partial^2}{\partial x^2} + \frac{\partial^2}{\partial y^2}$. The boundary conditions for the vertical walls are:

$$\begin{aligned} u &= v = 0, \quad T = T_h \quad \text{at} \quad x = 0 \quad \text{and} \\ u &= v = 0, \quad T = T_c \quad \text{at} \quad x = H \quad \forall \quad y, \end{aligned} \tag{3.5}$$

and for the horizontal walls are:

$$u = v = 0, \quad \frac{\partial T}{\partial y} = 0 \quad \text{at} \quad y = 0 \quad \text{and} \quad y = H \quad \forall \quad x. \tag{3.6}$$

To make the above system dimensionless, we introduce the following non-dimensional variables:

$$\begin{aligned} x^* &= \frac{x}{H}, \quad y^* = \frac{y}{H}, \quad u^* = \frac{uH}{\alpha}, \quad v^* = \frac{vH}{\alpha}, \quad T^* = \frac{T - T_0}{T_h - T_c}, \quad \text{and} \\ p^* &= \frac{pH^2}{\rho\alpha^2}. \end{aligned} \tag{3.7}$$

The dimensionless form of the equations (3.1)-(3.4) on dropping the asterisks become

$$\frac{\partial u}{\partial x} + \frac{\partial v}{\partial y} = 0, \tag{3.8}$$

$$u\frac{\partial u}{\partial x} + v\frac{\partial u}{\partial y} = -\frac{\partial p}{\partial x} + Pr\nabla^2 u, \tag{3.9}$$

$$u\frac{\partial v}{\partial x} + v\frac{\partial v}{\partial y} = -\frac{\partial p}{\partial y} + RaPrT + Pr\nabla^2 v, \tag{3.10}$$

$$u\frac{\partial T}{\partial x} + v\frac{\partial T}{\partial y} = \nabla^2 T, \tag{3.11}$$

where $Ra = g\beta_T(T_h - T_c)H^3/\nu\alpha$ and $Pr = \nu/\alpha$ are the dimensionless parameters mentioned earlier. Now introducing dimensionless vorticity ω and stream-function ψ, defined by

$$\omega = \frac{\partial u}{\partial y} - \frac{\partial v}{\partial x}, \tag{3.12}$$

and

$$u = \frac{\partial \psi}{\partial y}, \quad v = -\frac{\partial \psi}{\partial x}, \tag{3.13}$$

the equations (3.8)-(3.11) can be written as

$$u\frac{\partial \omega}{\partial x} + v\frac{\partial \omega}{\partial y} = Pr\nabla^2\omega + RaPr\frac{\partial T}{\partial x}, \tag{3.14}$$

$$\nabla^2\psi = -\omega, \tag{3.15}$$

$$u\frac{\partial T}{\partial x} + v\frac{\partial T}{\partial y} = \nabla^2 T. \tag{3.16}$$

If the reference temperature T_0 is taken as being equal to T_c, the dimensionless boundary conditions become:

$$\begin{aligned} u &= v = \psi = 0, \quad T = 1 \quad \text{at} \quad x = 0 \quad \text{and} \\ u &= v = \psi = 0, \quad T = 0 \quad \text{at} \quad x = 1 \quad \forall \quad y, \end{aligned} \tag{3.17}$$

and

$$u = v = \psi = 0, \quad \frac{\partial T}{\partial y} = 0 \quad \text{at} \quad y = 0 \quad \text{and} \quad y = 1 \quad \forall \quad x. \tag{3.18}$$

The vorticity boundary conditions are derived from equations (3.13)-(3.15).

The Nusselt number characterizes the rate of heat transfer across the cavity. The local Nusselt number in the horizontal direction at any point in the cavity is

$$Q(x, y) = uT - \frac{\partial T}{\partial x}. \tag{3.19}$$

Through any line parallel to the y-axis, this is given by

$$Nu_x = \int_0^1 Q(x, y)dy. \tag{3.20}$$

Finally, integrating Nu_x along the horizontal direction, the average Nusselt number is computed by

$$\overline{Nu} = \int_0^1 Nu_x dx. \tag{3.21}$$

3.3 Discretization and Related Issues

As stated earlier, discretization of the governing equations in the the present study are carried out by the HOC scheme described in Chapter 2. This was also used in ref. [67] for the ψ-ω form of the 2D steady-state N-S equations.

3.3.1 Discretization of the Governing Equations

For the vorticity equation (3.14), ϕ, c, d and f in equation (2.3) are replaced by ω, $\dfrac{u}{Pr}$, $\dfrac{v}{Pr}$ and $Ra\dfrac{\partial T}{\partial x}$ respectively. In the HOC scheme outlined in Chapter 2, it is assumed that the forcing function is either known analytically or its discrete approximation is available. However, the forcing function in the vorticity equation here is not explicitly known and is in derivative form. It may be mentioned that in the earlier HOC simulation of the present physical configuration [20] (using a mechanism different from the one used here), although the overall accuracy of the scheme was fourth, the approximation to this derivative source term was only second order accurate. In the following, we proceed to obtain a compact fourth order accurate approximation of this term applying again the mechanism of using the original PDE.

$$\left.\frac{\partial T}{\partial x}\right|_{ij} = \left[\delta_x T - \frac{h^2}{6}\frac{\partial^3 T}{\partial x^3}\right]_{ij} + O(h^4). \tag{3.22}$$

From equation (3.16),

$$\begin{aligned}\left.\frac{\partial^3 T}{\partial x^3}\right|_{ij} &= \left[-\frac{\partial^3 T}{\partial x \partial y^2} + u\frac{\partial^2 T}{\partial x^2} + \frac{\partial u}{\partial x}\frac{\partial T}{\partial x} + v\frac{\partial^2 T}{\partial x \partial y} + \frac{\partial v}{\partial x}\frac{\partial T}{\partial y}\right]_{ij}, \\ &= \left[-\delta_x\delta_y^2 T + u\delta_x^2 T + \delta_x u \delta_x T + v\delta_x\delta_y T + \delta_x v \delta_y T\right]_{ij} + O(h^2).\end{aligned} \tag{3.23}$$

Substituting equation (3.23) into equation (3.22) yields

$$\left.\frac{\partial T}{\partial x}\right|_{ij} = \delta_x T_{ij} + \frac{h^2}{6}\left[\delta_x\delta_y^2 T - u\delta_x^2 T - \delta_x u\delta_x T - v\delta_x\delta_y T - \delta_x v\delta_y T\right]_{ij} + O(h^4). \tag{3.24}$$

Also for equation (3.15), $\phi = \psi$, $c = d = 0$ and $f = \omega$. Once ω and ψ are obtained, the velocities u and v can easily be calculated in the following way:

$$u_{ij} = \left.\frac{\partial \psi}{\partial y}\right|_{ij} = \left[\delta_y\psi - \frac{h^2}{6}\frac{\partial^3\psi}{\partial y^3}\right]_{ij} + O(h^4),$$

and using equation (3.15),

$$u_{ij} \;=\; \delta_y\psi_{ij} - \frac{h^2}{6}\left[-\frac{\partial\omega}{\partial y} - \frac{\partial^3\psi}{\partial x^2\partial y}\right]_{ij} + O(h^4),$$

$$= \quad \delta_y \psi_{ij} + \frac{h^2}{6}[\delta_y \omega + \delta_x^2 \delta_y \psi]_{ij} + O(h^4). \tag{3.25}$$

Likewise for the y-component of velocity,

$$v_{ij} = -\delta_x \psi_{ij} - \frac{h^2}{6}[\delta_x \omega + \delta_x \delta_y^2 \psi]_{ij} + O(h^4). \tag{3.26}$$

Finally, for the equation (3.16) $\phi = T, \quad c = u, \quad d = v, \quad f = 0.$

For the calculation of heat flux $Q(x, y)$ appearing in equation (3.19) across the cavity, except at $x = 0$ and $x = 1$, the fourth order approximation of $\dfrac{\partial T}{\partial x}$ is computed using equation (3.24). At the vertical boundaries, in addition to the standard two point first order formula, the third and fourth order Jensen formulae [64] have also been used. The Nusselt numbers Nu_x and $\overline{Nu}$ are calculated through numerical integration using Simpson's rule.

It may be mentioned that the treatment of the first order derivative source term mentioned earlier can easily be extended to second order derivatives as well. One such situation arises in the solution of pressure Poisson equation at the end of a ψ-ω computation. However, the more important point is that through this source term treatment, an HOC scheme for the primitive variable form of the 2D N-S equations can be constructed as the pressure gradient term in the momentum equation and the source term in the pressure Poisson equation can now be handled.

3.3.2 HOC Wall Boundary Conditions

The stream-function ψ equals zero on the boundaries. At the corners, both u and v do not vary in the x- and y-directions and therefore the vorticity is equal to zero. Using forward differencing on the left wall, equation (3.13) yields,

$$\begin{aligned} v_{1,j} &= -\left.\frac{\partial \psi}{\partial x}\right|_{1,j}, \\ &= -\left[\delta_x^+ \psi - \frac{h}{2}\frac{\partial^2 \psi}{\partial x^2} - \frac{h^2}{6}\frac{\partial^3 \psi}{\partial x^3} - \frac{h^3}{24}\frac{\partial^4 \psi}{\partial x^4}\right]_{1,j} + O(h^4). \end{aligned} \tag{3.27}$$

As $v_{1,j}$ equals zero, using equation (3.15), we have

$$\begin{aligned} 0 &= -\left[\delta_x^+\psi + \frac{h}{2}\left(\omega + \frac{\partial^2\psi}{\partial y^2}\right) + \frac{h^2}{6}\left(\frac{\partial\omega}{\partial x} + \frac{\partial^3\psi}{\partial x\partial y^2}\right) + \frac{h^3}{24}\left(\frac{\partial^2\omega}{\partial x^2} + \frac{\partial^4\psi}{\partial x^2\partial y^2}\right)\right]_{1,j} \\ &+ O(h^4). \end{aligned}$$

Also in view of the fact that $\frac{\partial^2\psi}{\partial y^2} = \frac{\partial}{\partial y}(u) = 0$, $\frac{\partial^3\psi}{\partial x\partial y^2} = \frac{\partial^2 v}{\partial y^2} = 0$ on the left wall and $\frac{\partial^4\psi}{\partial x^2\partial y^2} = \frac{\partial^3}{\partial x\partial y^2}(\frac{\partial\psi}{\partial x}) = -\frac{\partial^3 v}{\partial x\partial y^2}$ [using (3.13)], the above relation becomes

$$0 = \left[-\delta_x^+\psi - \frac{h}{2}\omega - \frac{h^2}{6}\left(\delta_x^+\omega - \frac{h}{2}\frac{\partial^2\omega}{\partial x^2}\right) - \frac{h^3}{24}\left(\frac{\partial^2\omega}{\partial x^2} - \frac{\partial^3 v}{\partial x\partial y^2}\right)\right]_{1,j} + O(h^4).$$

As $u = v = 0$ on the walls, equation (3.14) yields $\nabla^2\omega + Ra\frac{\partial T}{\partial x} = 0$ and finally from the above, the following fourth order accurate expression is obtained on the left wall:

$$\left[-\delta_x^+\psi - \frac{h}{2}\omega - \frac{h^2}{6}\delta_x^+\omega + \frac{h^3}{24}\left(-\delta_y^2\omega - Ra\delta_x^+T\right) + \frac{h^3}{24}\delta_x^+\delta_y^2 v\right]_{1,j} = 0. \qquad (3.28)$$

Similarly on the right wall:

$$\left[-\delta_x^-\psi + \frac{h}{2}\omega - \frac{h^2}{6}\delta_x^-\omega + \frac{h^3}{24}\left(\delta_y^2\omega + Ra\delta_x^-T\right) - \frac{h^3}{24}\delta_x^-\delta_y^2 v\right]_{m,j} = 0. \qquad (3.29)$$

On the bottom wall:

$$\left[\delta_y^+\psi + \frac{h}{2}\omega + \frac{h^2}{6}\delta_y^+\omega + \frac{h^3}{24}\left(\delta_x^2\omega + Ra\delta_x T\right) + \frac{h^3}{24}\delta_x^2\delta_y^+ u\right]_{i,1} = 0. \qquad (3.30)$$

On the top wall:

$$\left[\delta_y^-\psi - \frac{h}{2}\omega + \frac{h^2}{6}\delta_y^-\omega - \frac{h^3}{24}\left(\delta_x^2\omega + Ra\delta_x T\right) - \frac{h^3}{24}\delta_x^2\delta_y^- u\right]_{i,m} = 0. \qquad (3.31)$$

Here space indices vary from 1 to m in both x- and y-directions.

On the top and bottom walls, we now proceed to develop a fourth order accurate temperature boundary condition. These two walls are insulated and at a typical node (i,j), we may write

$$0 = \frac{\partial T}{\partial y} = \left[\delta_y T - \frac{h^2}{6}\frac{\partial^3 T}{\partial y^3}\right]_{ij} + O(h^4).$$

As on the boundaries $\nabla^2 T = 0$, the last relation yields

$$0 = \left[\delta_y T + \frac{h^2}{6}\delta_x^2 \delta_y T\right]_{ij} + O(h^4).$$

Thus the finite difference approximation of the temperature equation on the insulated boundaries are:

$$T_{i+1,j+1} + T_{i-1,j+1} + 4T_{i,j+1} = T_{i+1,j-1} + T_{i-1,j-1} + 4T_{i,j-1}. \tag{3.32}$$

Again HOC discretization of the energy equation (3.16) at the walls are given by

$$\begin{aligned} T_{i+1,j+1} &+ T_{i-1,j+1} + 4(T_{i+1,j} + T_{i,j+1} + T_{i-1,j}) \\ &+ (T_{i+1,j-1} + T_{i-1,j-1} + 4T_{i,j-1}) - 20T_{ij} = 0. \end{aligned} \tag{3.33}$$

From equations (3.32) and (3.33), it follows that, for the lower boundary,

$$T_{i+1,2} + T_{i-1,2} + 4T_{i,2} + 2(T_{i+1,1} + T_{i-1,1}) - 10T_{i,1} = 0, \tag{3.34}$$

and for the upper boundary,

$$T_{i+1,m-1} + T_{i-1,m-1} + 4T_{i,m-1} + 2(T_{i+1,m} + T_{i-1,m}) - 10T_{i,m} = 0. \tag{3.35}$$

This new approach used to develop the temperature boundary conditions on the insulated walls can also be extended to similar physical situations for a flow variable ϕ, where, on the boundary, $\dfrac{\partial \phi}{\partial n} = 0$ and $\nabla^2 \phi = 0$ (n being the direction normal to the boundary). One important situation of this nature could be the pressure Poisson equation with zero pressure gradient boundary conditions, when HOC algorithm is attempted to be extended to the primitive variable formulation of the N-S equations.

3.4 Numerical Issues

The nonlinearity of the governing equations necessitates an iterative solution procedure. We use a decoupled algorithm where vorticity, stream-function and temperature are solved in sequence separately, lagging the appropriate terms. The successive iterates for the temperature have been slightly over-relaxed and that for stream-function and vorticity have been under-relaxed. That is to say, if ϕ' is the unrelaxed update of ϕ^n, then ϕ^{n+1} is given by

$$\phi^{n+1} = \lambda_r \phi' + (1 - \lambda_r)\phi^n,$$

where λ_r is the relaxation factor and the superscripts n and $n+1$ are iteration indices.

The HOC discretization of the stream-function equation yields coefficient matrices which are symmetric and positive definite and therefore, CG [37] algorithm has been used for them. On the other hand, those for the vorticity and temperature equations provide matrices that are non-symmetric and hence, for them, a hybrid BiCGStab [62] algorithm has been employed.

For computational advantage, the computed solution for a lower Ra can be used as the initial guess for a higher Ra. The vorticity, stream-function and temperature equations are solved in that order. The CG and hybrid BiCGStab iterations used for solving these equations to a certain accuracy are termed as inner iterations. The process of iteratively solving the three equations once may be termed as one outer iteration which is to be repeated till convergence is achieved. It may be noted that the number of inner iterations needed to meet a particular stopping criterion generally reduces with the progress of outer iterations. If the systems associated with ψ-, ω- and T-equations are represented by $A\mathbf{z} = \mathbf{b}$, the inner iterations are terminated here as soon as the residual $\|A\mathbf{z} - \mathbf{b}\|_2$ (where $\|.\|_2$ is the l_2 norm) falls below 10^{-10}. Convergence is considered to be achieved when the maximum difference between two successive iterates for all of ψ, ω and T falls below 10^{-10}.

It may be noted that for an $n \times n$ grid, A is an $n^2 \times n^2$ matrix and, $\mathbf{z}$ and

b are n^2-component vectors. However, the actual storage required for A is much less than $n^2 \times n^2$ words, as the algorithm requires the storage of only the non zero elements of A. Number of non zero entries of A for ω-, ψ- and T-equations are $9n^2 - 20n + 24, 9n^2 - 32n + 32$ and $9n^2 - 22n + 12$ respectively. A condition number analysis based on power method for eigenvalues, shows that the matrices are well conditioned, the value of the condition number generally being less than 1.3. This is the reason why no need for pre-conditioning was felt while using the CG and hybrid BiCGStab algorithms. All computations in this work were carried out on a HP C 200 machine using a sequential code.

3.5 Results and Discussion

The results of the present computations for a fluid of $Pr = 0.71$ with Ra ranging from a moderate to a high laminar regime ($Ra = 10^3$ to 10^7) are presented in this section through tables and graphs. Tables 3.1, 3.2 and 3.3 compare the computed values (on a 81×81 grid) of the absolute value of the stream-function ψ at the mid-point of the cavity $|\psi_{mid}|$, the average Nusselt number $\overline{Nu}$ and the maximum vertical velocity at the horizontal mid-plane v_{max} respectively with some well established results and the agreement with most of them is found to be excellent. Tables 3.4-3.7 present the results for $Ra = 10^3$ to 10^6 respectively on grids of sizes 21×21, 41×41 and 81×81. Table 3.8 shows the results for $Ra = 10^7$ on a 81×81 grid. The quantities presented here are: $|\psi_{mid}|$, the maximum horizontal velocity u_{max} on the ver-

Table 3.1: *Comparisons for* $|\psi_{mid}|$.

Ra	10^3	10^4	10^5	10^6	10^7
De Vahl Davis [18]	1.174	5.071	9.111	16.32	$--$
Ramaswamy *et al.* [54]	1.170	5.099	9.217	16.68	29.436
Le Quéré [52]	$--$	$--$	$--$	16.38	29.362
Dennis [20]	1.175	5.074	9.113	$--$	$--$
Present	1.175	5.080	9.123	16.42	29.382

Table 3.2: *Comparisons for* $\overline{Nu}$.

Ra	10^3	10^4	10^5	10^6	10^7
Chenoweth *et al.* [14]	1.118	2.244	4.520	8.822	16.82
De Vahl Davis [18]	1.118	2.243	4.519	8.800	$--$
Le Quéré [52]	$--$	$--$	$--$	8.825	16.52
Hortmann *et al.* [31]	$--$	2.245	4.521	8.825	$--$
Saitoh *et al.* [57]	$--$	2.242	$--$	8.712	$--$
Ball *et al.* [8]	1.118	2.244	4.522	8.825	16.52
Ho *et al.* [29]	1.118	2.248	4.528	8.824	16.52
Comini *et al.* [16]	$--$	$--$	4.503	8.825	16.53
Present	1.118	2.245	4.522	8.829	16.52

Table 3.3: *Comparisons for* v_{max}.

Ra	10^3	10^4	10^5	10^6	10^7
Chenoweth *et al.* [14]	3.695	19.62	68.63	220.8	699.0
De Vahl Davis [18]	3.697	19.62	68.63	219.4	$--$
Ramaswamy *et al.* [54]	$--$	19.62	68.64	232.97	717.04
Le Quéré [52]	$--$	$--$	$--$	220.56	699.2
Saitoh *et al.* [57]	$--$	19.62	$--$	216.76	$--$
Ho it et al. [29]	3.697	19.63	68.63	219.86	705.3
Hortmann *et al.* [31]	$--$	19.63	68.64	220.46	$--$
Dennis [20]	3.698	19.63	68.64	$--$	$--$
Present	3.697	19.61	68.61	221.66	696.2

tical mid-plane together with its location, v_{max} together with its location, $\overline{Nu}$, the average Nusselt number $Nu_{\frac{1}{2}}$ on the vertical mid-plane of the cavity, the average Nusselt number Nu_0 on the hot wall, the maximum value of the local Nusselt number Nu_{0max} on the hot wall and the minimum value of the local Nusselt number Nu_{0min} on the hot wall together with its location.

Table 3.9 shows the percentage errors of different variables due to refinement of grid from 41×41 to 81×81. The grid-independence of the results is evident from this and Tables 3.4-3.7 as the variation in results is insignificantly small with grid refinement. Owing to high order (viz. fourth) accuracy of both

Table 3.4: *The solutions for* $Ra = 10^3$.

Grid size	$\lvert\psi_{mid}\rvert$	u_{max} (y)	v_{max} (x)	$\overline{Nu}$	$Nu_{\frac{1}{2}}$	Nu_0	Nu_{0max} (y)	Nu_{0min} (y)
21 × 21	1.178	3.647 (0.800)	3.675 (0.200)	1.116	1.120	1.115	1.494 (0.100)	0.697 (1.000)
41 × 41	1.176	3.642 (0.800)	3.699 (0.175)	1.117	1.118	1.117	1.503 (0.100)	0.693 (1.000)
81 × 81	1.175	3.650 (0.813)	3.697 (0.175)	1.118	1.118	1.118	1.505 (0.088)	0.692 (1.000)

Table 3.5: *The solutions for* $Ra = 10^4$.

Grid size	$\lvert\psi_{mid}\rvert$	u_{max} (y)	v_{max} (x)	$\overline{Nu}$	$Nu_{\frac{1}{2}}$	Nu_0	Nu_{0max} (y)	Nu_{0min} (y)
21 × 21	5.165	16.312 (0.800)	19.520 (0.150)	2.246	2.259	2.219	3.451 (0.150)	0.599 (1.000)
41 × 41	5.097	16.265 (0.825)	19.662 (0.125)	2.245	2.249	2.239	3.511 (0.150)	0.588 (1.000)
81 × 81	5.080	16.203 (0.825)	19.613 (0.125)	2.245	2.246	2.243	3.526 (0.150)	0.586 (1.000)

Table 3.6: *The solutions for* $Ra = 10^5$.

Grid size	$\lvert\psi_{mid}\rvert$	u_{max} (y)	v_{max} (x)	$\overline{Nu}$	$Nu_{\frac{1}{2}}$	Nu_0	Nu_{0max} (y)	Nu_{0min} (y)
21 × 21	9.172	36.375 (0.850)	66.326 (0.050)	4.507	4.502	4.321	7.001 (0.100)	0.809 (1.000)
41 × 41	9.142	35.156 (0.850)	68.138 (0.075)	4.522	4.523	4.479	7.519 (0.100)	0.748 (1.000)
81 × 81	9.123	34.825 (0.850)	68.606 (0.063)	4.522	4.522	4.512	7.670 (0.088)	0.733 (1.000)

the scheme and the boundary conditions, high quality solutions are obtained with as coarse a grid as 21 × 21. The Nusselt numbers which are presented

Table 3.7: *The solutions for* $Ra = 10^6$.

Grid size	$\lvert\psi_{mid}\rvert$	u_{max} (y)	v_{max} (x)	$\overline{Nu}$	$Nu_{\frac{1}{2}}$	Nu_0	Nu_{0max} (y)	Nu_{0min} (y)
21 × 21	15.542	63.635 (0.850)	213.397 (0.050)	8.491	8.357	7.399	11.557 (0.150)	1.267 (1.000)
41 × 41	16.442	66.515 (0.850)	210.696 (0.050)	8.815	8.807	8.525	15.761 (0.050)	1.095 (1.000)
81 × 81	16.420	65.332 (0.850)	221.658 (0.038)	8.829	8.829	8.763	17.018 (0.050)	1.007 (1.000)

Table 3.8: *The solutions for* $Ra = 10^7$.

Grid size	$\lvert\psi_{mid}\rvert$	u_{max} (y)	v_{max} (x)	$\overline{Nu}$	$Nu_{\frac{1}{2}}$	Nu_0	Nu_{0max} (y)	Nu_{0min} (y)
81 × 81	29.382	155.82 (0.863)	696.24 (0.025)	16.52	16.51	16.08	34.925 (0.025)	1.509 (1.000)

Table 3.9: *Percentage errors.*

Ra	$\lvert\psi_{mid}\rvert$	u_{max}	v_{max}	$\overline{Nu}$	$Nu_{\frac{1}{2}}$	Nu_0	Nu_{0max}	Nu_{0min}
10^3	0.05	0.03	0.01	0.09	0.00	0.09	0.13	0.14
10^4	0.33	0.39	0.25	0.00	0.13	0.18	0.43	0.34
10^5	0.21	0.95	0.68	0.00	0.02	0.73	0.66	2.05
10^6	0.13	1.81	4.95	0.16	0.25	2.72	7.39	8.74

Table 3.10: *Effect of order of accuracy of* $\frac{\partial T}{\partial x}$ *at* $x = 0$ *and 1 on* Nu*'s.*

Ra	Order	$\overline{Nu}$	$Nu_{\frac{1}{2}}$	Nu_0	Nu_{0max} (y)	Nu_{0min} (y)
10^3	$O(h^3)$	1.118	1.118	1.118	1.505 (0.088)	0.692 (1.000)
	$O(h^4)$	1.117	1.116	1.118	1.505 (0.088)	0.692 (1.000)
10^4	$O(h^3)$	2.245	2.246	2.245	3.527 (0.150)	0.587 (1.000)
	$O(h^4)$	2.244	2.245	2.245	3.528 (0.150)	0.587 (1.000)
10^5	$O(h^3)$	4.522	4.522	4.530	7.710 (0.088)	0.737 (1.000)
	$O(h^4)$	4.521	4.522	4.538	7.730 (0.088)	0.737 (1.000)
10^6	$O(h^3)$	8.831	8.829	8.967	17.789 (0.038)	1.022 (1.000)
	$O(h^4)$	8.830	8.829	9.028	17.980 (0.038)	1.024 (1.000)
10^7	$O(h^3)$	16.530	16.515	17.668	42.369 (0.025)	1.561 (1.000)
	$O(h^4)$	16.532	16.515	17.846	42.175 (0.025)	1.565 (1.000)

in Tables 3.4-3.8 are calculated using the first order approximation to $\frac{\partial T}{\partial x}$ at the vertical walls. The same Nusselt numbers estimated through the use of the third and fourth order Jensen formulae [64] are presented in Table 3.10. Comparisons amongst these Nusselt numbers clearly shows that except for the values of Nu_0 and Nu_{0max} calculated with the first order formula at $Ra = 10^7$, all the other estimates are in very close agreement, in particular, the values calculated with third and fourth order formulae. Table 3.11 gives the CPU time for the computations carried out.

Figure 3.2 shows the streamlines, the vorticity contours, isotherms and the Nusselt number distribution in the cavity for $Ra = 10^3$. Figures 3.3-3.6 show

Table 3.11: *CPU time (sec) for different Ra's.*

	Grid		
Ra	21 × 21	41 × 41	81 × 81
10^3	5.66	30.75	2114.60
10^4	9.17	53.50	4051.81
10^5	25.49	909.45	7209.11
10^6	575.00	2210.90	10811.23
10^7	− − −	− − −	72843.52

the same for $Ra = 10^4$, 10^5, 10^6 and 10^7 respectively. (Of the three numbers of the first three parts of the these figure captions, the number to the left of the parantheses represents the minimum contour value whereas the one at right represents the maximum and the number within the parantheses is the uniform interval at which the contours are plotted.) The contours and distributions bear very close resemblance with similar figures presented by De Vahl Davis [18], Le Quéré [52], Ramaswamy *et al.* [54], Chenoweth and Paolucci [14] and Hortmann *et al.* [31].

De Vahl Davis [18] obtained his results using an FTCS scheme of second order spatial accuracy in conjunction with Richardson extrapolation; similarly Chenoweth and Paolucci [14] used a second order accurate method followed by three point Richardson extrapolation and claimed their results to be sixth order accurate. It may however be noted that these extrapolated solutions are obtained only at those nodes that are shared by different levels of grids. Previously, need to use extrapolation to obtain higher order accurate solution using a lower order accurate scheme was probably necessitated by the absence of well-examined HOC schemes. In contrast, the present work obtains high quality solutions with a fourth order HOC scheme on a single coarse grid. The computations use De Vahl Davis' non-dimensionalization to obtain reasonably accurate solution even for a Rayleigh number as high as 10^7, although Le Quéré [52] remarked that De Vahl Davis' dimensionless form is inappropriate

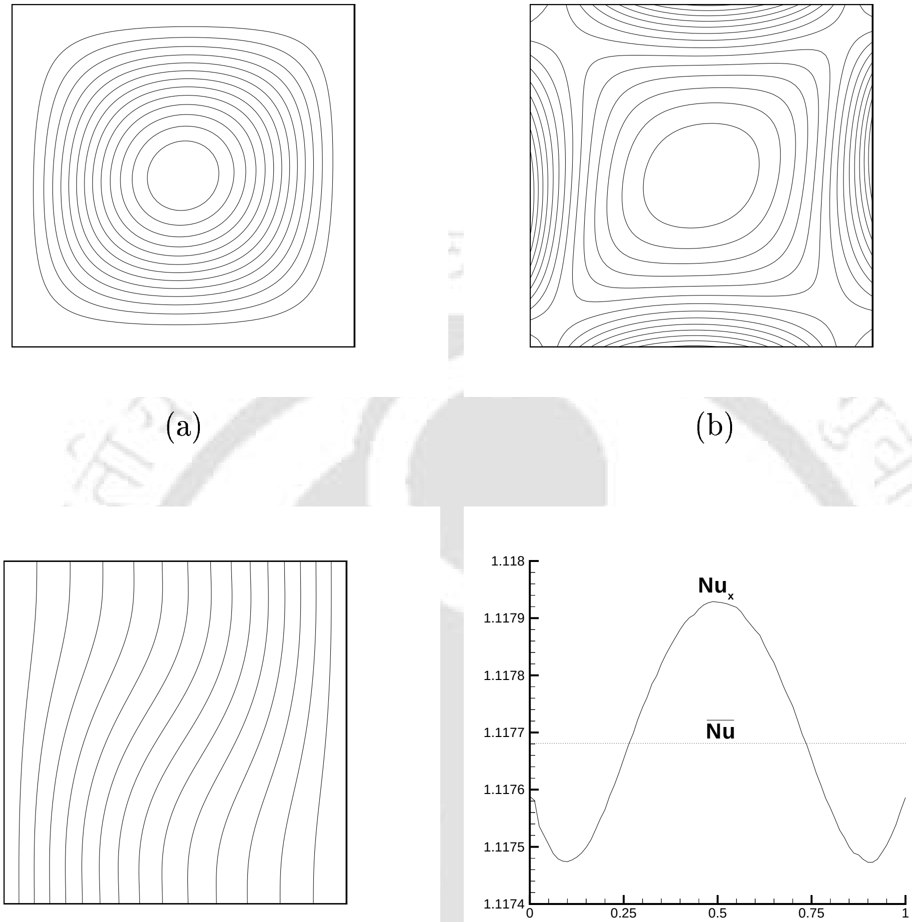

(a) (b)

(c) (d)

Figure 3.2: *For* $Ra = 10^3$, *(a) streamlines, at -1.175 (0.078) 0, (b) vorticity contours, at -32.02 (5.55) 51.25, (c) isotherms, at 0 (0.0625) 1 and (d) the Nusselt number distribution across the cavity.*

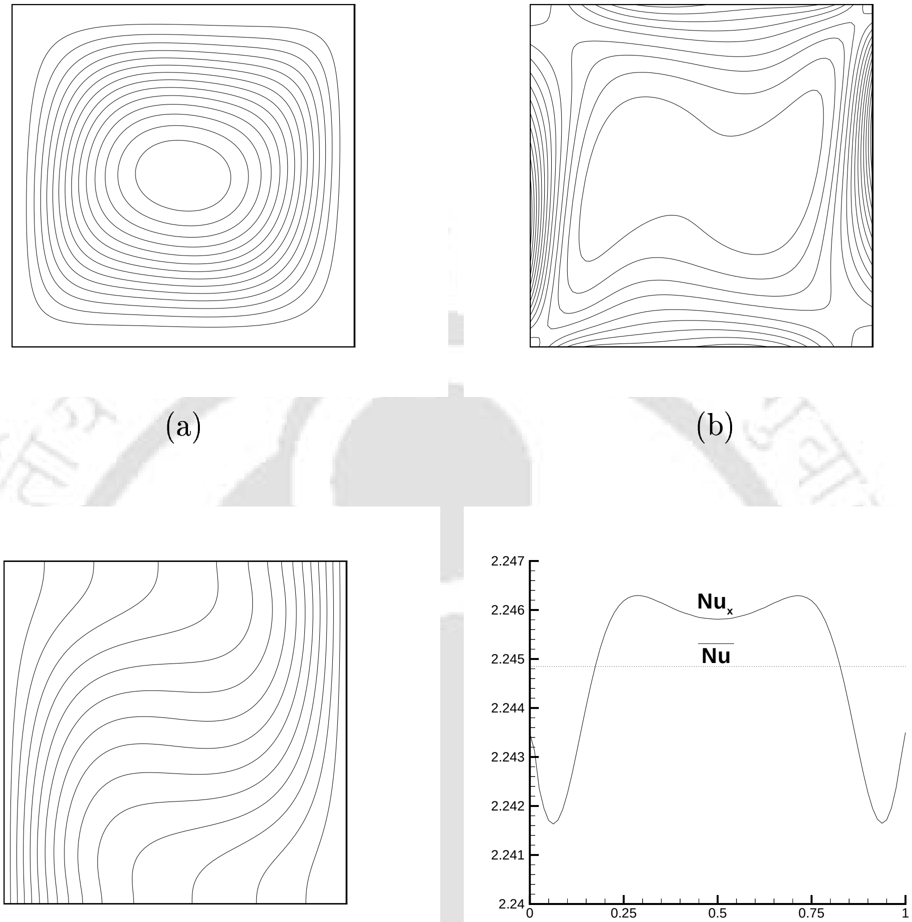

(a) (b)

(c) (d)

Figure 3.3: *For* $Ra = 10^4$, *(a) streamlines, at -5.079 (0.34) 0, (b) vorticity contours, at -124.90 (36.80) 427.17, (c) isotherms, at 0 (0.0625) 1 and (d) the Nusselt number distribution across the cavity.*

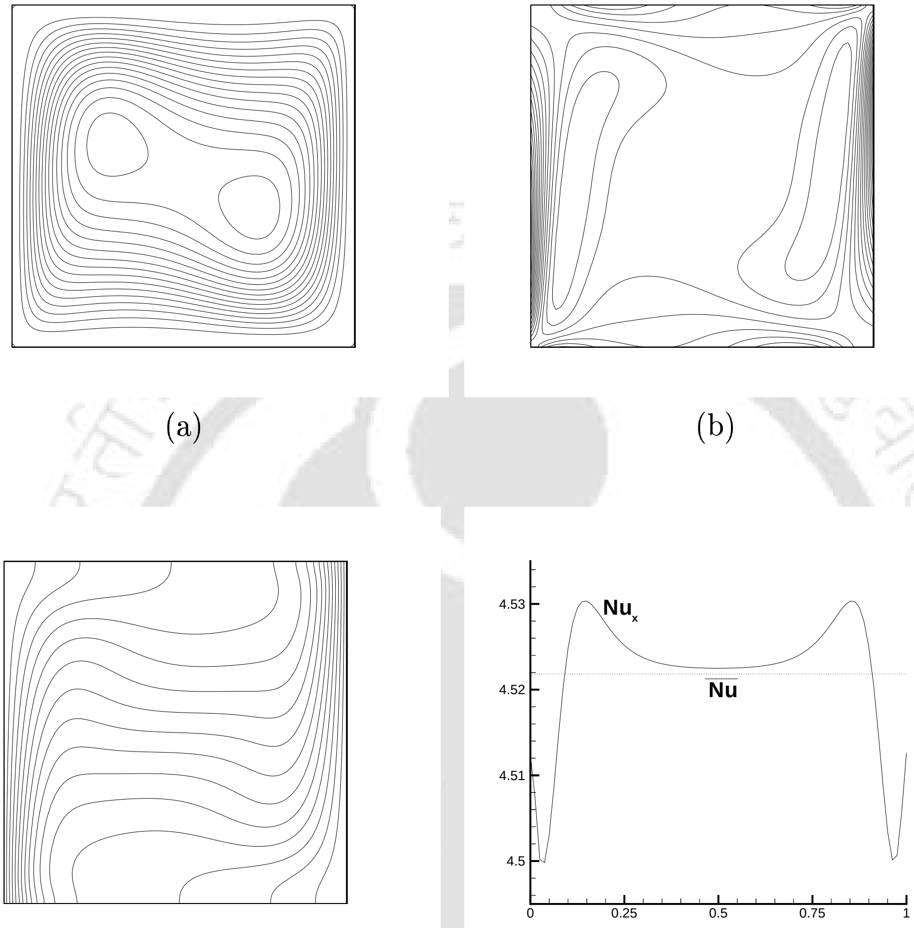

(a) (b)

(c) (d)

Figure 3.4: *For* $Ra = 10^5$, *(a) streamlines, at -9.633 (0.60) 0, (b) vorticity contours, at -606.95 (205.07) 2622.89, (c) isotherms, at 0 (0.0625) 1 and (d) the Nusselt number distribution across the cavity.*

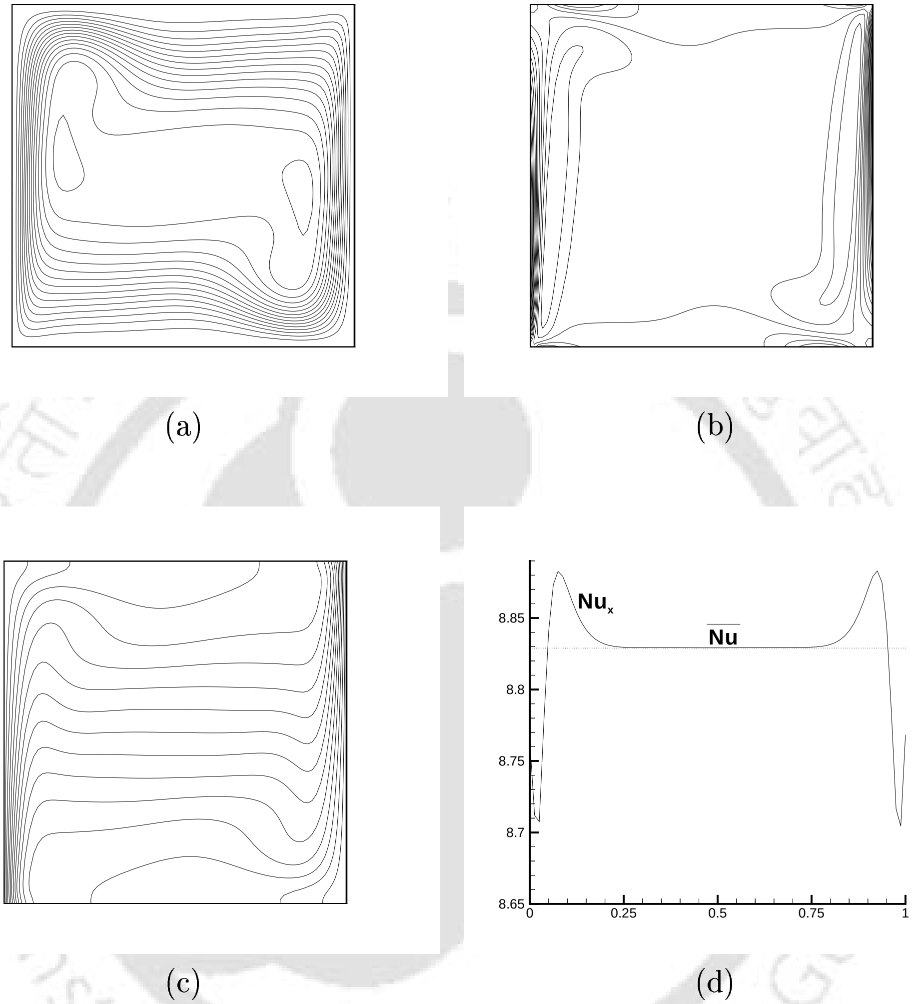

(a) (b)

(c) (d)

Figure 3.5: *For* $Ra = 10^6$, *(a) streamlines, at -16.86 (1.105) 0, (b) vorticity contours, at -3288.5 (1246.35) 1528.8, (c) isotherms, at 0 (0.0625) 1 and (d) the Nusselt number distribution across the cavity.*

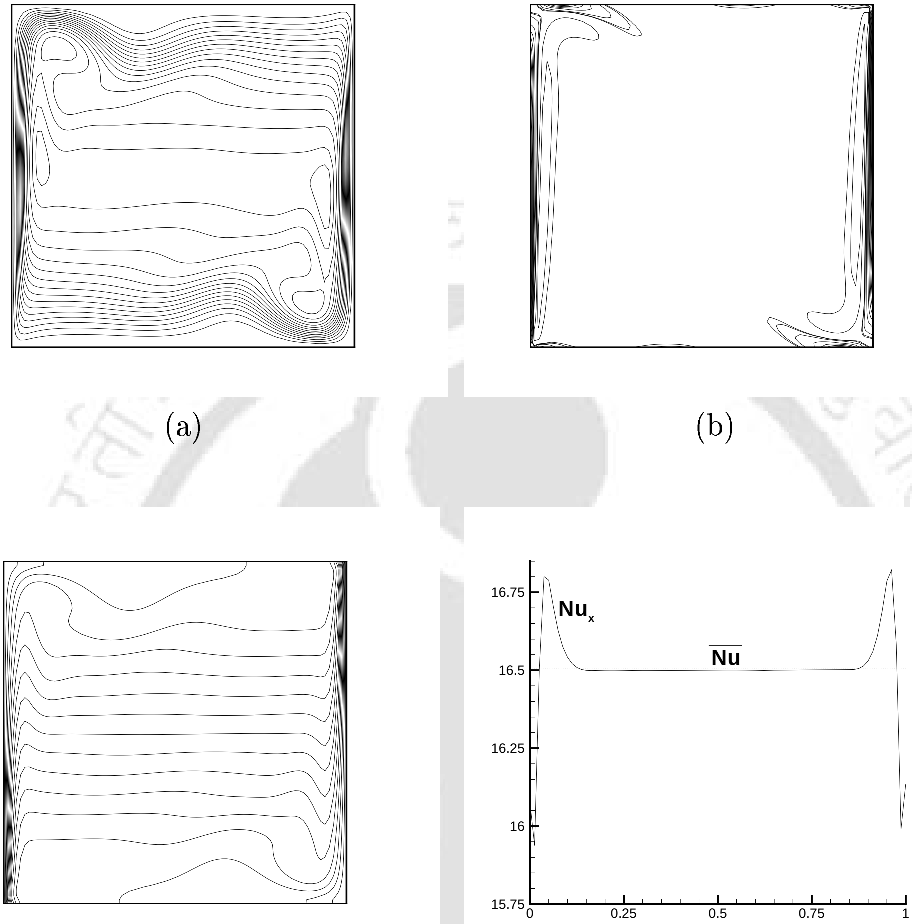

(a) (b)

(c) (d)

Figure 3.6: *For* $Ra = 10^7$, *(a) streamlines, at -30.32 (2.10) 0.049, (b) vorticity contours, at -18610 (6495.26) 86313.5, (c) isotherms, at 0 (0.0625) 1 and (d) the Nusselt number distribution across the cavity.*

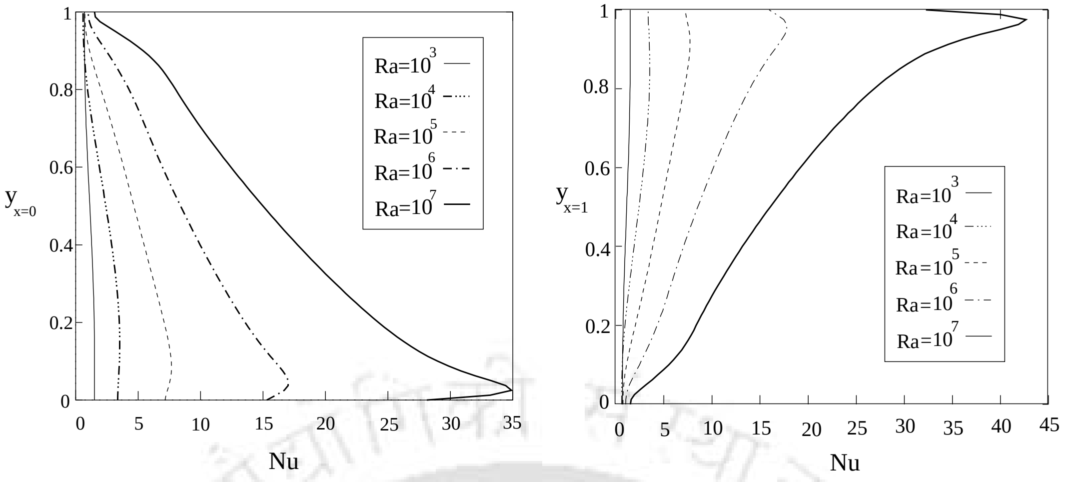

(a) (b)

Figure 3.7: *The (a) hot and (b) cold wall Nusselt number for different Ra.*

for the Rayleigh number regime beyond 10^6 and used a slightly different scaling.

For the range of Rayleigh numbers considered here, there is generally a centro symmetry of velocity, vorticity and temperature distribution. This is obvious from the streamlines and vorticity contours and the isotherms in parts (a), (b) and (c) of Figures 3.2-3.6. Secondary vortices appear at $Ra = 10^5$ and persist for higher Ra's. At $Ra = 10^7$, recirculation regions are seen to appear at the upper left and lower right corners (Figure 3.6 (a)). From part (b) of Figures 3.2-3.6, on the vertical walls, boundary layer thickness is seen to progressively decrease as Ra increases. Figure 3.7 shows the variations of local Nusselt numbers along the hot [(a)] and the cold [(b)] walls. It is seen from the figures that while the location of the maximum local Nusselt number at the hot wall progressively moves downwards as Ra increases, for the cold wall, the opposite happens. These observations tally with those of earlier investigators.

3.6 Conclusion

This work is concerned about fully HOC method for problems like the thermally driven square cavity with adiabatic horizontal walls and differentially heated vertical walls. The present study deals with flows in the region of Ra's varying from 10^3 to 10^7. In the previous (probably the only) example of HOC computation [20] for this problem, the difficult cases of $Ra = 10^6$ and 10^7 have not been studied. Also, the boundary conditions are not compact and the derivative source term that appears in the vorticity equation (viz. $\dfrac{\partial T}{\partial x}$) has been resolved at least to second order accuracy. The present work, besides including the results for the high Rayleigh numbers of $Ra = 10^6$ and 10^7, employes an algorithm which is uniformly fourth order accurate and compact in the discretization of the governing equations, treatment of the boundary conditions and source term resolution. This is the reason why the solution procedure may be termed as fully compact higher order method with the associated advantages. The no-heat-flux boundary condition at the adiabatic walls has been imposed through a special strategy taking care to maintain compactness at higher accuracy. The work also achieves higher-order compact resolution of the source term and its easy assimilation to the solution procedure. Another fact that we come across in course of the work is that Le Quéré's [52] observation about De Vahl Davis' non-dimensionalization [18] being not adequate beyond $Ra = 10^6$ may not be correct as computation has been carried out here with the same non-dimensionalization with sufficient accuracy. Also, in course of the estimation of the hot wall Nusselt numbers, De Vahl Davis [18] observed that varying the order of approximation of the finite difference formulae produced significantly different values. But in the present calculations, close agreement amongst the Nusselt numbers estimated through approximation of $\dfrac{\partial T}{\partial x}$ at the vertical walls with formulae of three different orders show that the solutions obtained by the present method are indeed very accurate. Finally, use of CG and hybrid BiCGStab algorithms to solve the symmetric and non-symmetric algebraic systems at every outer iteration makes the solution procedure robust. The method also has the advantage that the fully HOC method used provides matrices that are well-conditioned and hence the complexity of constructing an efficient pre-conditioner is avoided.

Chapter 4

HOC SCHEMES FOR TRANSIENT CONVECTION-DIFFUSION

4.1 Introduction

This chapter describes the development of a class of higher order compact schemes with weighted time discretization for the 2D unsteady convection-diffusion equation with variable convection coefficients [1]. The unsteady form of the 2D convection-diffusion equation (2.3) in Chapter 2 can be written as

$$b\frac{\partial \phi}{\partial t} - \nabla^2 \phi + c(x,y,t)\frac{\partial \phi}{\partial x} + d(x,y,t)\frac{\partial \phi}{\partial y} = f(x,y,t), \qquad (4.1)$$

where $b(>0)$ is a constant, c and d are as defined in Chapter 2, and f is a forcing function analogous to the one in equation (2.3). The only difference between the convection coefficients c, d and the forcing function f in equation (4.1) and those in equation (2.3) is that they are now dependent on time t as well.

---

[1] Published in *Int. J. Num. Meth. Fluids [35].*

There have been attempts earlier also to develop HOC schemes for transient problems. Several explicit or partially implicit higher-order schemes were developed for the unsteady incompressible N-S equations by Hirsh [28] and Rai and Moin [53], and for compressible N-S equations by Lele [39]. Abarbanel and Kumar [1], at about the same time, proposed some explicit schemes based on the HOC approach for the Euler equations. These schemes are spatially fourth and temporally second order accurate. Recently a second order time accurate explicit scheme for 2D advection dominated flows has been presented by Balzano [9]. Explicit schemes, though very easy to implement, have a severe stability limit to the time step [5, 6, 63]. On the other hand, implicit schemes can be applied to obtain time-accurate solution of an inherently unsteady flow or time marching steady-state solution with a larger time step. Several higher-order implicit schemes for the one dimensional (1D) time dependent convection-diffusion problems were developed by Noye and Tan [45]. Later on, they also developed a 9-point scheme of third order spatial and second order temporal accuracy for the 2D convection-diffusion equations with constant coefficients [46]. The 2D fourth order accurate 9-point HOC scheme proposed in ref. [67] was extended by Spotz to solve the unsteady 1D convection-diffusion and 2D diffusion equations [65]. Few other schemes that have been developed for the unsteady 2D N-S equations are the implicit higher-order accurate schemes of Strikwerda [71], the upwind compact schemes of Yanwen *et al.* [78] and Sesterhenn [59], and the implicit weighted essentially non-oscillatory scheme of Chen *et al.* [13]. Some of these schemes (for example, [71]), however, could not adequately capture the high Reynolds number regime of incompressible viscous flows.

The present work proposes a class of implicit HOC schemes for the 2D unsteady convection-diffusion in line with the steady-state scheme of ref. [42]. In the process it also removes, for the first time, the restriction of usual HOC schemes [42, 67] of having to use a grid aspect ratio of unity. The schemes accommodate Dirichlet as well as Neumann boundary condition easily. They solve very accurately and efficiently the unsteady 2D convection-diffusion problems including 2D incompressible N-S equations. One of the most important factors that determines the merit of a scheme for transient problems is the time-wise accuracy [6, 11] and the proposed schemes are temporally first or second and spatially fourth order accurate. To test the robustness, accuracy and efficiency of the schemes, they are applied to five pertinent test cases for which numerical and/or analytical results are available. The first one serves as a perfect example to illustrate inherent features of the schemes like diffusion and anti-diffusion and their suppression. It is evident from the next two test cases that the proposed schemes accurately capture the transient flow of problems governed by the 2D incompressible N-S equations even for a Reynolds number as high as 10000. Also being implicit in nature, they capture the steady-state time marching solutions very efficiently as can be seen from the last two cases. Grid independence studies and error analysis has been carried out wherever necessary. Comparison with analytical and established numerical results shows excellent agreement.

4.2 Discretization and Numerical Procedure

For the HOC formulation (2.12) described in Chapter 2, the uniform mesh size was the same in both x- and y-directions. In other words, the grid aspect ratio had to be necessarily equal to unity. In this section, an HOC scheme is first developed for the steady-state convection-diffusion equation on a grid free from this restriction. Assuming the problem domain to be rectangular and constructing on it a uniform rectangular mesh of steps h and k in the x- and y-directions respectively, the truncation error τ_{ij} of the CDS approximation (2.5) of (2.3) is given by

$$\tau_{ij} = \left[\frac{h^2}{12}\left(2c\frac{\partial^3\phi}{\partial x^3} - \frac{\partial^4\phi}{\partial x^4}\right) + \frac{k^2}{12}\left(2d\frac{\partial^3\phi}{\partial y^3} - \frac{\partial^4\phi}{\partial y^4}\right)\right]_{ij} + O(h^4, k^4) \qquad (4.2)$$

As in Chapter 2, each of the derivatives in the leading TE term are compactly approximated to $O(h^2, k^2)$ using the original PDE (2.3). Finally, the $O(h^4, k^4)$

approximation to equation (2.3) is obtained as

$$\begin{aligned} &- \alpha_{ij}\delta_x^2\phi_{ij} - \beta_{ij}\delta_y^2\phi_{ij} + C_{ij}\delta_x\phi_{ij} + D_{ij}\delta_y\phi_{ij} \\ &- \frac{h^2+k^2}{12}[\delta_x^2\delta_y^2 - c_{ij}\delta_x\delta_y^2 - d_{ij}\delta_x^2\delta_y - \gamma_{ij}\delta_x\delta_y]\phi_{ij} = F_{ij}, \end{aligned} \tag{4.3}$$

where the coefficients $\alpha_{ij}, \beta_{ij}, \gamma_{ij}, C_{ij}, D_{ij}$ and F_{ij} are as follows:

$$\alpha_{ij} = 1 + \frac{h^2}{12}(c_{ij}^2 - 2\delta_x c_{ij}), \tag{4.4}$$

$$\beta_{ij} = 1 + \frac{k^2}{12}(d_{ij}^2 - 2\delta_y d_{ij}), \tag{4.5}$$

$$\gamma_{ij} = \frac{2}{h^2+k^2}\left(h^2\delta_x d_{ij} + k^2\delta_y c_{ij}\right) - c_{ij}d_{ij}, \tag{4.6}$$

$$C_{ij} = \left[1 + \frac{h^2}{12}(\delta_x^2 - c_{ij}\delta_x) + \frac{k^2}{12}(\delta_y^2 - d_{ij}\delta_y)\right] c_{ij}, \tag{4.7}$$

$$D_{ij} = \left[1 + \frac{h^2}{12}(\delta_x^2 - c_{ij}\delta_x) + \frac{k^2}{12}(\delta_y^2 - d_{ij}\delta_y)\right] d_{ij}, \tag{4.8}$$

$$F_{ij} = \left[1 + \frac{h^2}{12}(\delta_x^2 - c_{ij}\delta_x) + \frac{k^2}{12}(\delta_y^2 - d_{ij}\delta_y)\right] f_{ij}, \tag{4.9}$$

As before, sufficient smoothness is assumed for ϕ, c, d and f.

For unsteady case, equation (4.1) will be similar to equation (2.3), but the coefficients c and d are functions of x, y and t, and the expression on the right hand side becomes $f(x,y,t) - b\frac{\partial\phi}{\partial t}$. Using forward difference for $\frac{\partial\phi}{\partial t}$ with a time step Δt, we approximate the unsteady equation (4.1) as

$$\begin{aligned} b\delta_t^+\phi_{ij}^n \quad &+ \overbrace{b\left[\frac{h^2}{12}(\delta_x^2 - c_{ij}\delta_x) + \frac{k^2}{12}(\delta_y^2 - d_{ij}\delta_y)\right]\delta_t^+\phi_{ij}^n} \\ &- \alpha_{ij}\delta_x^2\phi_{ij}^n - \beta_{ij}\delta_y^2\phi_{ij}^n + C_{ij}\delta_x\phi_{ij}^n + D_{ij}\delta_y\phi_{ij}^n \\ &- \frac{h^2+k^2}{12}[\delta_x^2\delta_y^2 - c_{ij}\delta_x\delta_y^2 - d_{ij}\delta_x^2\delta_y - \gamma_{ij}\delta_x\delta_y]\,\phi_{ij}^n = F_{ij}, \end{aligned} \tag{4.10}$$

where δ^+ denotes the forward difference operator and the superscript n stands for the time level. The coefficients α_{ij}, β_{ij}, γ_{ij}, C_{ij}, D_{ij} and F_{ij} are the same as those appearing in equations (4.4)-(4.9) and are to be calculated at the nth time level. Equation (4.10) can be rewritten as

$$\sum_{k_1=-1}^{1}\sum_{k_2=-1}^{1} w_{i+k_1,j+k_2}\ \phi_{i+k_1,j+k_2}^{n+1} = \sum_{k_1=-1}^{1}\sum_{k_2=-1}^{1} w'_{i+k_1,j+k_2}\ \phi_{i+k_1,j+k_2}^{n} + 12F_{ij}, \tag{4.11}$$

where

$$w_{i+k_1,j+k_2} = q_{i+k_1,j+k_2},\ w'_{i+k_1,j+k_2} = 12p_{i+k_1,j+k_2} + q_{i+k_1,j+k_2},$$

with $\lambda_1 = \dfrac{\Delta t}{h^2}$, $\lambda_2 = \dfrac{\Delta t}{k^2}$ and

$$p_{i-1,j-1} = \frac{\lambda_1+\lambda_2}{2}\left(-\frac{1}{6} - \frac{c_{ij}h}{12} - \frac{d_{ij}k}{12} + \frac{\gamma_{ij}hk}{24}\right), \qquad q_{i-1,j-1} = 0,$$

$$p_{i,j-1} = -\lambda_2\beta_{ij} - \frac{\lambda_2 D_{ij}k}{2} + \frac{\lambda_1+\lambda_2}{6} + \frac{d_{ij}k\,(\lambda_1+\lambda_2)}{12}, \qquad q_{i,j-1} = b(1+\frac{d_{ij}k}{2}),$$

$$p_{i+1,j-1} = \frac{\lambda_1+\lambda_2}{2}\left(-\frac{1}{6} + \frac{c_{ij}h}{12} - \frac{d_{ij}k}{12} - \frac{\gamma_{ij}hk}{24}\right), \qquad q_{i+1,j-1} = 0,$$

$$p_{i-1,j} = -\lambda_1\alpha_{ij} - \frac{\lambda_1 C_{ij}h}{2} + \frac{\lambda_1+\lambda_2}{6} + \frac{c_{ij}h\,(\lambda_1+\lambda_2)}{12}, \qquad q_{i-1,j} = b(1+\frac{c_{ij}h}{2}),$$

$$p_{ij} = 2\lambda_1\alpha_{ij} + 2\lambda_2\beta_{ij} - \frac{\lambda_1+\lambda_2}{3}, \qquad q_{ij} = 8b,$$

$$p_{i+1,j} = -\lambda_1\alpha_{ij} + \frac{\lambda_1 C_{ij}h}{2} + \frac{\lambda_1+\lambda_2}{6} - \frac{c_{ij}h(\lambda_1+\lambda_2)}{12}, \qquad q_{i+1,j} = b(1-\frac{c_{ij}h}{2}),$$

$$p_{i-1,j+1} = \frac{\lambda_1+\lambda_2}{2}\left(-\frac{1}{6} - \frac{c_{ij}h}{12} + \frac{d_{ij}k}{12} - \frac{\gamma_{ij}hk}{24}\right), \qquad q_{i-1,j+1} = 0,$$

$$p_{i,j+1} = -\lambda_2\beta_{ij} + \frac{\lambda_2 D_{ij}k}{2} + \frac{\lambda_1+\lambda_2}{6} - \frac{d_{ij}k\,(\lambda_1+\lambda_2)}{12}, \qquad q_{i,j+1} = b(1-\frac{d_{ij}k}{2}),$$

$$p_{i+1,j+1} = \frac{\lambda_1+\lambda_2}{2}\left(-\frac{1}{6} + \frac{c_{ij}h}{12} + \frac{d_{ij}k}{12} + \frac{\gamma_{ij}hk}{24}\right), \qquad q_{i+1,j+1} = 0.$$

A weighted average parameter μ is now introduced through the use of the forward time approximation of $\frac{\partial \phi}{\partial t}$ such that $t_\mu = (1-\mu)t^n + \mu t^{n+1}$ for $0 \le \mu \le 1$. Varying μ provides a class of integrators; for example, forward Euler for $\mu = 0$, backward Euler for $\mu = 1$ and Crank-Nicholson for $\mu = 0.5$. Consequently, the coefficients $w_{i+k_1,j+k_2}$ and $w'_{i+k_1,j+k_2}$ in equation (4.11) can be written as $w_{i+k_1,j+k_2} = 12\mu p_{i+k_1,j+k_2} + q_{i+k_1,j+k_2}$ and $w'_{i+k_1,j+k_2} = 12(\mu-1)p_{i+k_1,j+k_2} + q_{i+k_1,j+k_2}$ respectively, and F_{ij}^n on the right hand side of (4.11) takes the form $\mu F_{ij}^{n+1} + (1-\mu)F_{ij}^n$. With these replacements, (4.11) becomes the HOC finite-difference approximation for the unsteady 2D convection-diffusion equation with fourth order spatial accuracy. All the schemes arising in this way are implicit because of the operator under the brace in equation (4.10). The accuracy of the schemes are $O\left((\Delta t)^s, h^4, k^4\right)$, with $s = 1$ or 2. Again, it should be noted that for $\mu = 0$, the difference stencil requires 9 points in the nth and 5 points in the $(n+1)$th time level resulting in what may be called a (9,5) scheme. Similarly, a (9,9) and a (5,9) scheme are obtained for $\mu = 0.5$ and $\mu = 1$ respectively. The HOC stencils emerging in this way have been illustrated in Figure 4.1.

The system of equations (4.11) can be written in the matrix form as

$$A\mathbf{\Phi^{n+1}} = \mathbf{f}(\mathbf{\Phi^n}), \tag{4.12}$$

where the coefficient matrix A is an asymmetric sparse matrix. For a grid of size $m \times n$, A has a dimension mn, and $\mathbf{\Phi^{n+1}}$ and $\mathbf{f}(\mathbf{\Phi^n})$ are mn-component vectors. Partitioning A, $\mathbf{\Phi^{n+1}}$ and $\mathbf{f}(\mathbf{\Phi^n})$ into sub-matrices corresponding to the interior and boundaries, equation (4.12) can be written as

$$\begin{pmatrix} A_L & 0 & 0 & 0 & 0 \\ 0 & A_B & 0 & 0 & 0 \\ 0 & 0 & A_D & 0 & 0 \\ 0 & 0 & 0 & A_T & 0 \\ 0 & 0 & 0 & 0 & A_R \end{pmatrix} \begin{pmatrix} \mathbf{\Phi_L^{n+1}} \\ \mathbf{\Phi_B^{n+1}} \\ \mathbf{\Phi_D^{n+1}} \\ \mathbf{\Phi_T^{n+1}} \\ \mathbf{\Phi_R^{n+1}} \end{pmatrix} = \begin{pmatrix} \mathbf{f}(\mathbf{\Phi_L^n}) \\ \mathbf{f}(\mathbf{\Phi_B^n}) \\ \mathbf{f}(\mathbf{\Phi_D^n}) \\ \mathbf{f}(\mathbf{\Phi_T^n}) \\ \mathbf{f}(\mathbf{\Phi_R^n}) \end{pmatrix},$$

where L, R, B and T stand respectively for the left, right, bottom and top boundaries of the domain and D for the interior region. The block square matrices A_B and A_T are of order m, A_L and A_R are of order $(n-2)$, and A_D is of order $(m-2)(n-2)$. If boundary conditions are of Dirichlet type or

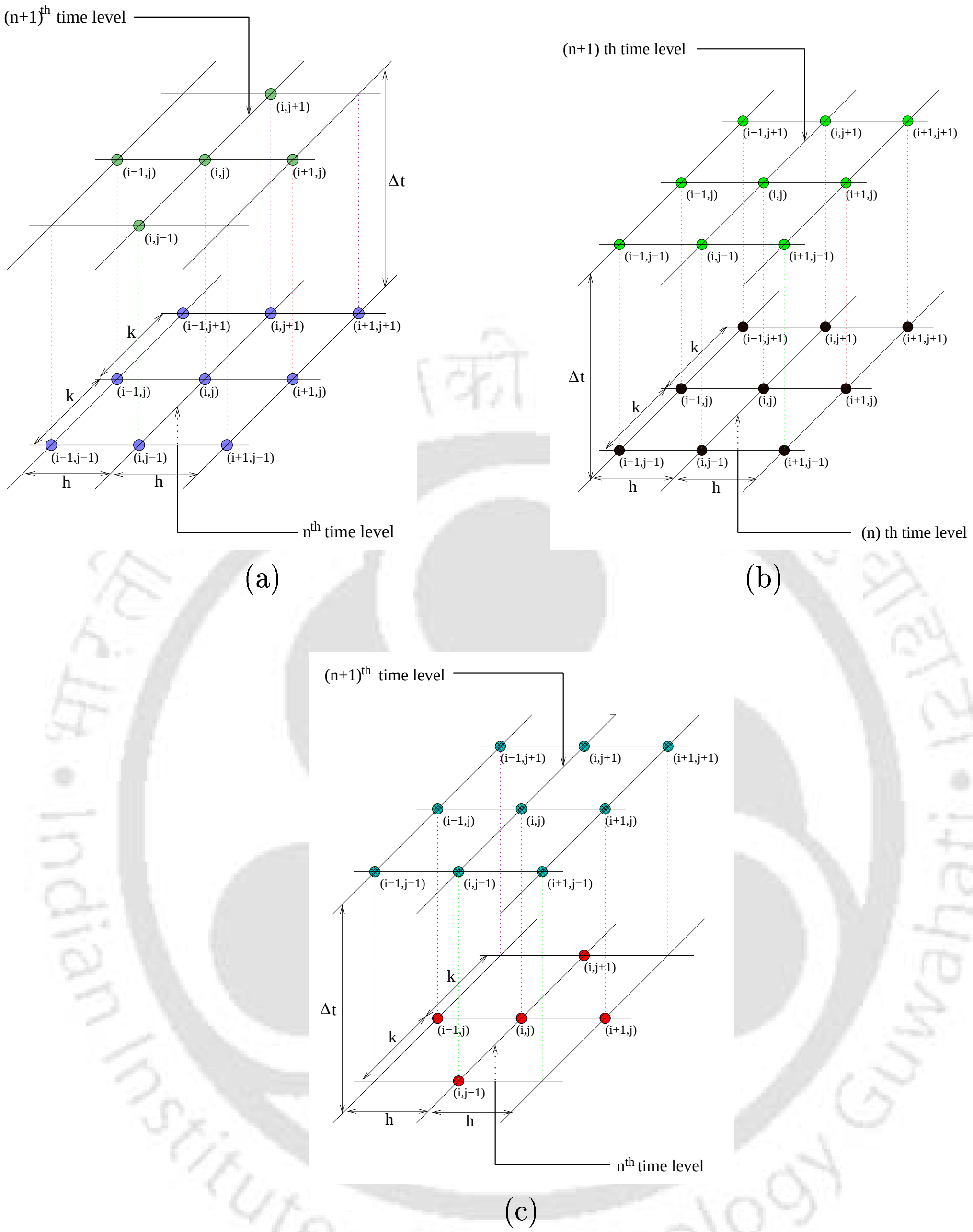

(a) (b)

(c)

Figure 4.1: *Unsteady HOC stencils for (a)* $\mu = 0$, $\mu = 0.5$ *and* $\mu = 1.0$.

they result in explicit expressions for the transport variables, the sub-matrices representing the boundary conditions are identity matrices. For an implicit expression, they will be sparse matrices with the number of non-zero entries in a particular row depending upon the order of the scheme. The matrix A_D which has at most nine non-zero entries in a particular row has the form shown below. In matrix A, 0's are rectangular null matrices of orders ranging from

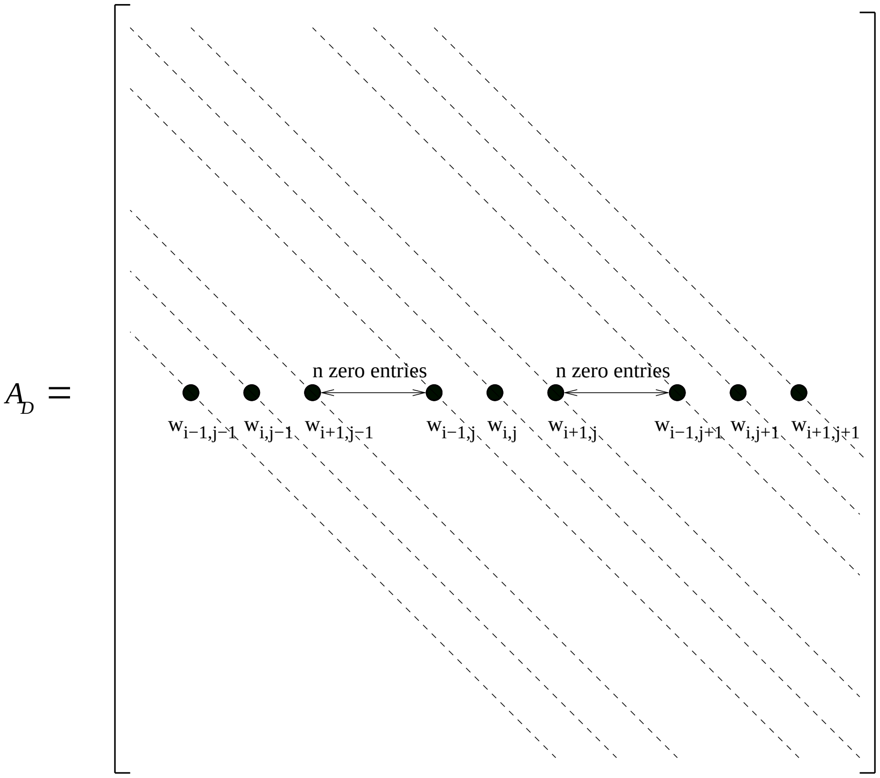

$m \times (n-2)$ to $m \times (m-2)(n-2)$. The details of the elements of the column vectors on the left hand side are as follows:

$$\mathbf{\Phi_L} = [\phi_{1,2},\ \ldots\ ,\phi_{1,n-1}]^{\mathcal{T}}, \quad \mathbf{\Phi_B} = [\phi_{1,1},\ \ldots\ ,\phi_{m,1}]^{\mathcal{T}},$$
$$\mathbf{\Phi_T} = [\phi_{1,n},\ \ldots\ ,\phi_{m,n}]^{\mathcal{T}}, \quad \mathbf{\Phi_R} = [\phi_{m,2},\ \ldots\ ,\phi_{m,n-1}]^{\mathcal{T}}$$

and

$$\mathbf{\Phi_D} = [\phi_{2,2}, \ldots, \phi_{m-1,2},\ \phi_{2,3}, \ldots, \phi_{m-1,3},\ \ldots,$$
$$\phi_{2,n-1}, \ldots, \phi_{m-1,n-1}]^{\mathcal{T}}.$$

On the right hand side, the $(n-2)$-component vectors $\mathbf{f}(\mathbf{\Phi^n_L})$ and $\mathbf{f}(\mathbf{\Phi^n_R})$, and the m-component vectors $\mathbf{f}(\mathbf{\Phi^n_B})$ and $\mathbf{f}(\mathbf{\Phi^n_T})$ correspond to the boundaries whereas the entries of the $(m-2)(n-2)$-component vector $\mathbf{f}(\mathbf{\Phi^n_D})$ are given by the right hand side of equation (4.11). Thus $\mathbf{f}(\mathbf{\Phi^n})$ being known in terms of the current transport variables, equation (4.12) can be solved with an iterative method for the transport variables in the next time level. As mentioned earlier, the coefficient matrix arising from the present HOC discretization is not diagonally dominant and conventional iterative methods such as Gauss-Seidel cannot be used. In order to solve this system of equations, conjugate gradient method (**CG**) [37] for pure diffusion (when $c = d = 0$) and a hybrid biconjugate gradient stabilized method (**BiCGStab**) [62] for convection-diffusion have been employed without any pre-conditioning. For a problem having Dirichlet or explicitly expressed boundary conditions, A will have at most $2[m+n-2]+9\times(m-2)(n-2)$ non-zero entries. Consequently, the matrix-vector product $A\mathbf{\Phi^{n+1}}$ required by the iterative solvers involves $2[m+n-2]+81\times(m-2)(n-2)$ arithmetic operations only.

4.3 Stability Analysis

A von Neumann linear stability analysis of the schemes is now performed assuming the convective coefficients c and d to be constants and forcing function f to be zero for a particular HOC stencil with the (i,j)th node at the centre. If $\phi^n_{ij} = B^n e^{I\theta_x i} e^{I\theta_y j}$, where $I = \sqrt{-1}$, B^n is the amplitude at time level n, and $\theta_x (= 2\pi h/\Lambda_1)$ and $\theta_y (= 2\pi k/\Lambda_2)$ are phase angles with wavelengths Λ_1 and Λ_2 respectively, the amplification factor $\xi (= \dfrac{B^{n+1}}{B^n})$, for stability, has to satisfy the relation

$$|\xi|^2 - 1 \leq 0.$$

Now ξ can be found by substituting the expression for ϕ^n_{ij} and ϕ^{n+1}_{ij} in equation (4.11) and the stability criteria of the schemes becomes (details given in Appendix A)

$$(1-2\mu) \leq \frac{2b}{\Lambda_1(8+h^2c^2)+\Lambda_2(8+k^2d^2)}. \tag{4.13}$$

Introducing Courant numbers $C_x = \dfrac{c\Delta t}{bh}$, $C_y = \dfrac{d\Delta t}{bk}$ and cell Reynolds numbers $Re_h = ch$, $Re_k = dk$, we obtain

$$(1-2\mu)\left[C_x Re_h^{-1}\left(8+Re_h^2\right)+C_y Re_k^{-1}\left(8+Re_k^2\right)\right] \le 2 \qquad (4.14)$$

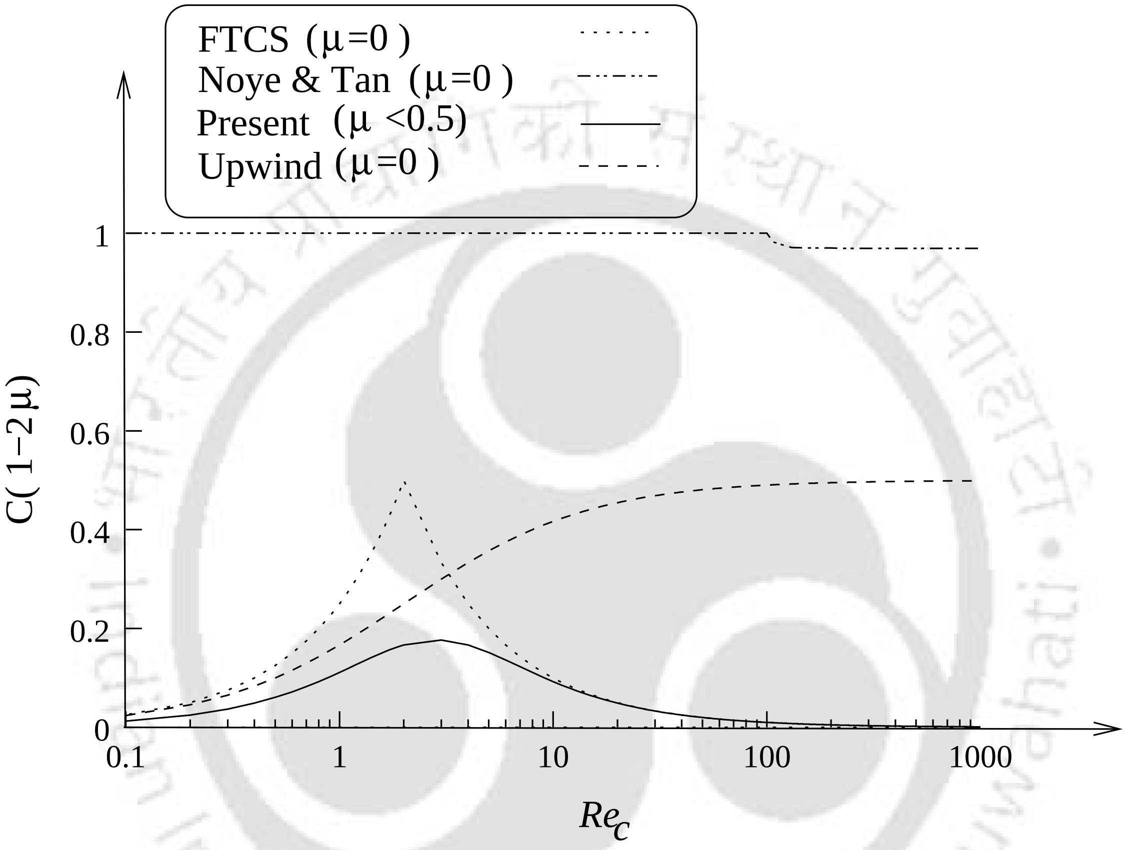

Figure 4.2: *The regions of von Neumann stability for different schemes.*

In particular, if $Re_h = Re_k = Re_c$ and $C_x = C_y = C$, these yield the stability condition

$$C(1-2\mu) \le \frac{Re_c}{8+Re_c^2}. \qquad (4.15)$$

It is seen that a scheme is conditionally stable for $0 \le \mu < 0.5$. The region of stability for this particular case represented by (4.15) together with that of other schemes, viz. upwind, FTCS, and $(9,9)$ scheme of Noye and Tan [46] are shown in Figure 4.2. Here, a scheme is stable in the region below its curve. Though the conditional stability criterion is restrictive, particularly for large Re_c, for $0.5 \leq \mu \leq 1$, the scheme is unconditionally stable for all values of Re_c.

4.4 Numerical Test Cases

In order to study the validity and effectiveness of the proposed schemes, they are applied to three unsteady and two steady 2D test problems. The unsteady problems considered are (i) the convection-diffusion of a Gaussian pulse, (ii) the flow decayed by viscosity and (iii) the Taylor's vortex problem. The remaining two problems, where nonlinearity is very high and steady-state is arrived at in a time marching fashion are, (iv) the lid-driven square cavity flow and (v) the flow due to double-diffusive natural convection in a vertical porous annulus. The last problem will be described in details in Chapter 5. As the first three problems have analytical solutions, Dirichlet boundary conditions have been used for them, whereas for the remaining two, both Dirichlet and Neumann boundary conditions have been applied.

4.4.1 Problem 1

Consider equation (4.1) with $f = 0$ and constant convective coefficients in the square $0 \leq x,\ y \leq 2$ with initial condition given, as in [46], by

$$\phi(x,y,0) = exp\left[-b((x-0.5)^2 + (y-0.5)^2)\right] \tag{4.16}$$

An analytical solution to this problem is

$$\phi(x,y,t) = \frac{1}{4t+1} exp\left[-\frac{b}{4t+1}((x-ct-0.5)^2 + (y-dt-0.5)^2)\right] \tag{4.17}$$

The initial condition is a Gaussian pulse centred at $(0.5, 0.5)$ with pulse height 1. The boundary conditions have been taken from the analytical solution given

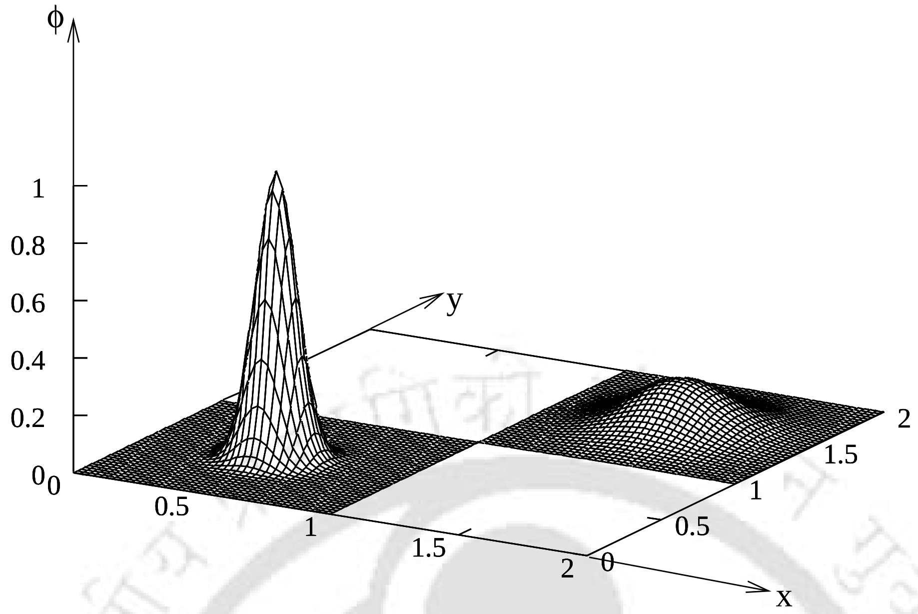

Figure 4.3: *The initial and the numerical [$(9,9)$, $\Delta t = 0.00625$] pulse at t=1.25.*

by equation (4.17). For the sake of comparison of our results with those of Noye and Tan [46], we have chosen $b = 100$ and $c = d = 80$.

The initial pulse and the pulse at $t = 1.25$ found numerically through the present scheme are shown in Figure 4.3. A remarkably similar picture is obtained from the analytical solution (Figure 4.4) where at $t = 1.25$ the Gaussian pulse moves to a position centred at $(1.5, 1.5)$ with a pulse height of $\frac{1}{6}$.

The average and the maximum absolute errors of different schemes including the present ones along with their CPU times have been presented in Table 4.1. Using the modified equivalent partial differential equation (MEPDE) [46] approach, it is found that if the time step is not small enough, the present (9,5) and (5,9) schemes are not adequate to capture the original pulse. This fact is also reflected in Figures 4.5 (a) and 4.6 (a). Table 4.2 depicts, at $t = 1.25$,

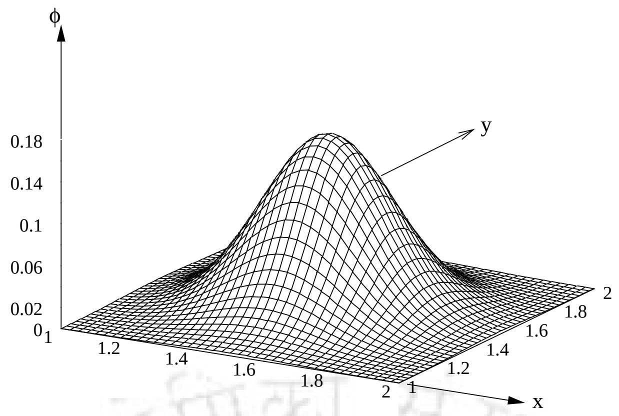

(a)

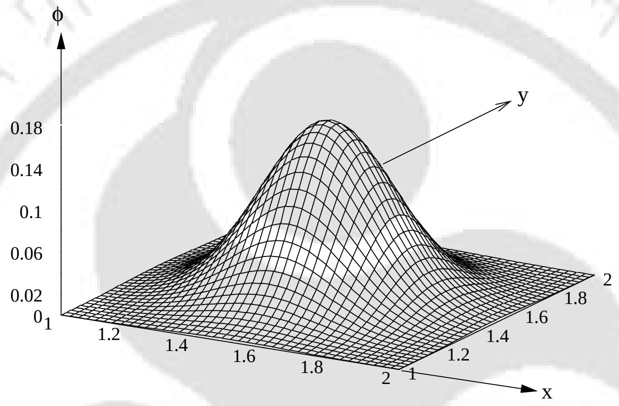

(b)

Figure 4.4: *Surface plots of the (a) exact and (b) numerical [*$(9,9)$, $\Delta t = 0.00625$*] approximation to the pulse in the subregion* $1 \leq x,\ y \leq 2$ *at* $t = 1.25$.

Table 4.1: *Errors and CPU times for Problem 1 at* $t = 1.25$ *with* $\Delta t = 0.0125$ *and* $h = k = 0.025$.

Method	Average$\lvert error \rvert$	Maximum$\lvert error \rvert$	CPU time (secs)
FTCS	3.94×10^{-3}	1.21×10^{-1}	1.67
Upwind	2.65×10^{-3}	6.63×10^{-2}	3.34
Noye and Tan	1.43×10^{-5}	4.84×10^{-4}	−−
Present (9,5)	1.49×10^{-3}	3.74×10^{-2}	16.34
Present (5,9)	1.02×10^{-3}	2.25×10^{-2}	11.74
Present (9,9)	1.59×10^{-5}	4.48×10^{-4}	8.78

the pulse height for different schemes and time steps. At the same instant, the location of the centre of the pulse is $(1.5, 1.5)$, the same as that of the exact pulse, for all computations in Table 4.2. As seen from the same table, and Figures 4.5 (a) and 4.7 (a), the first order time accurate (9,5) scheme shows a pulse height higher than the exact because of the presence of in-built numerical

Table 4.2: *The pulse height at* $t = 1.25$ *with different time steps schemes.*

Method	Δt	Pulse height
(9,5)	0.00625	0.202492
	0.00025	0.167553
	0.0001	0.166852
(5,9)	0.00625	0.144447
	0.0001	0.165983
	0.00005	0.166210
(9,9)	0.0125	0.166863
	0.00625	0.166540
	0.0001	0.166656
Analytical		0.166667

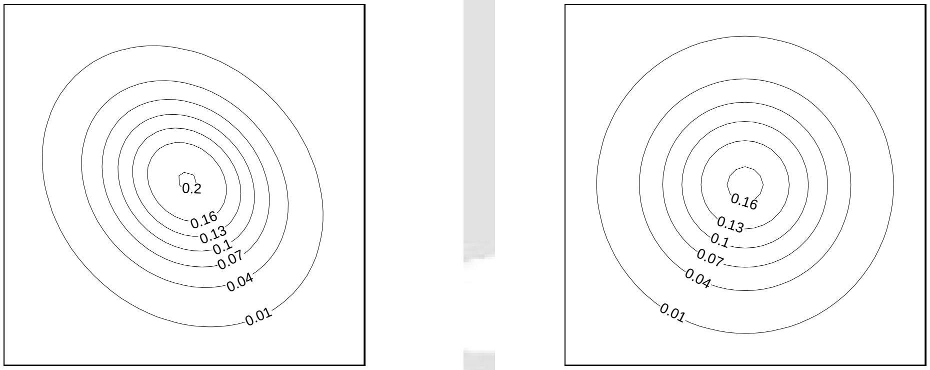

(a) (b)

Figure 4.5: *Contour plots of the pulse in the subregion* $1 \leq x,\ y \leq 2$ *at* $t = 1.25$ *for* $(9, 5)$ *scheme with (a)* $\Delta t = 0.00625$ *and (b)* $\Delta t = 0.0001$.

anti-diffusion. To be precise, as seen from Figure 4.5 (a), the anti-diffusion

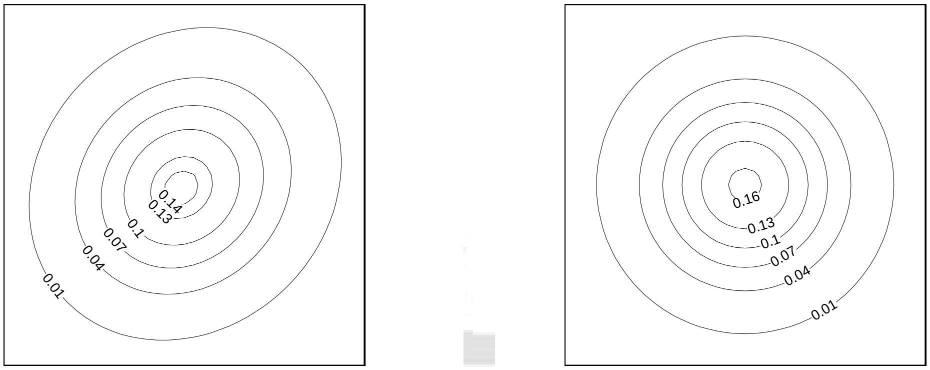

(a) (b)

Figure 4.6: *Contour plots of the pulse in the subregion* $1 \leq x,\ y \leq 2$ *at* $t = 1.25$ *for* $(5, 9)$ *scheme with (a)* $\Delta t = 0.00625$ *and (b)* $\Delta t = 0.0001$.

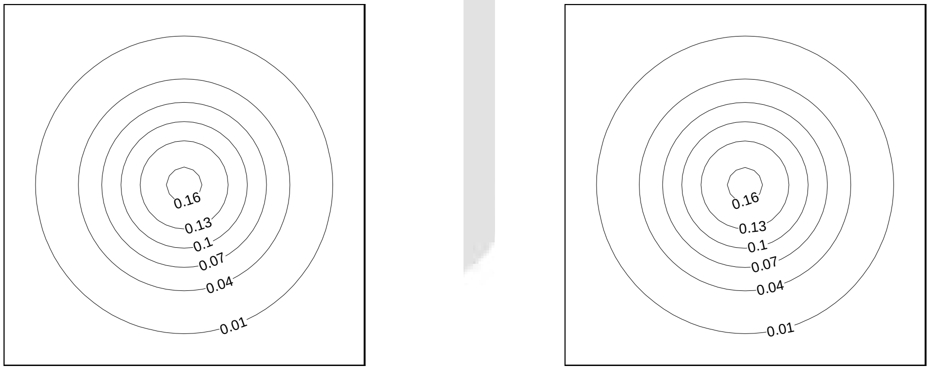

(a) (b)

Figure 4.7: *Contour plots of the pulse in the subregion* $1 \leq x,\ y \leq 2$ *at* $t = 1.25$, *(a) exact and (b) for the* $(9, 9)$ *scheme with* $\Delta t = 0.00625$.

is prominent along the diagonal parallel to $y = x$, whereas little change in diffusion is noticed along the diagonal parallel to $y = -x$. This asymmetry in diffusivity produces elliptic contours. On the other hand, the in-built numerical diffusion in the (5,9) scheme explains the lower pulse height seen from Table 4.2, and Figures 4.6 (a) and 4.7 (a). From Figure 4.6 (a), it is clear that there is additive numerical diffusion along $y = x$, whereas diffusion along $y = -x$ remains largely unaffected. Table 4.2 shows that the magnitudes of numerical diffusivity and anti-diffusivity decrease with the reduction in time step and with smaller values, highly accurate solutions can be obtained. This is illustrated by the computed contours of Figures 4.5 (b) and 4.6 (b), and the exact contours of Figure 4.5 (a). The (9,9) scheme gives a remarkably accurate solution even with a relatively larger time step $\Delta t = 0.00625$, yielding a pulse which is almost indistinguishable from the exact one as seen from Table 4.2 and, Figures 4.4 and 4.7. This is also reflected by Table 4.3 which tracks the exact and numerical pulse height at positions $(0.5, 0.5)$ and $(1.5, 1.5)$ with the relative errors. It will be worthwhile to compare the time-wise efficiency of the present $(9, 9)$ scheme with the $(9, 9)$ scheme of Noye and Tan [46] as both the schemes are implicit and second order accurate in time. The CPU time ratio of the $(9, 9)$ scheme of ref. [46] to FTCS scheme is approximately 447 (30851:69) whereas the same for the present $(9, 9)$ scheme to FTCS is 5.257 (Table 4.1). This clearly shows the superior time-wise efficiency of the present scheme.

Table 4.3: *Numerical and exact values of* ϕ *at different time levels with* $\Delta t = 0.00125$ *and* $h = k = .025$ *at the points* $(0.5, 0.5)$ *and* $(1.5, 1.5)$.

Time	ϕ_{nu} at (0.5,0.5)	ϕ_{ex} at (0.5,0.5)	% error	ϕ_{nu} at (1.5,1.5)	ϕ_{ex} at (1.5,1.5)	% error
0.125	0.175741	0.175731	0.006	0.000000	0.000000	0.000
0.250	0.009231	0.009158	0.797	0.000000	0.000000	0.000
0.375	0.000307	0.000299	2.675	0.000000	0.000000	0.000
0.625	0.000000	0.000000	0.000	0.000000	0.000000	0.000
0.750	0.000000	0.000000	0.000	0.000088	0.000084	4.762
0.875	0.000000	0.000000	0.000	0.004108	0.004070	0.933
1.000	0.000000	0.000000	0.000	0.040355	0.040379	0.059
1.125	0.000000	0.000000	0.000	0.126160	0.126390	0.181
1.250	0.000000	0.000000	0.000	0.166428	0.166667	0.143

In the next three examples, the results obtained only through the (9,9) scheme have been presented, although sufficiently accurate results are obtained using the other two schemes as well.

4.4.2 Problem 2

The problem of flow decayed by viscosity [15, 71, 78] is governed by the 2D N-S equations, which in non-dimensional form for an incompressible flow can be written as

$$\frac{\partial u}{\partial x}+\frac{\partial v}{\partial y}=0, \tag{4.18}$$

$$\frac{\partial u}{\partial t}+u\frac{\partial u}{\partial x}+v\frac{\partial u}{\partial y}=-\frac{\partial p}{\partial x}+\frac{1}{Re}\nabla^2 u, \tag{4.19}$$

$$\frac{\partial v}{\partial t}+u\frac{\partial v}{\partial x}+v\frac{\partial v}{\partial y}=-\frac{\partial p}{\partial y}+\frac{1}{Re}\nabla^2 v, \tag{4.20}$$

in the square $0 \leq x, y \leq \pi$. Here u and v are the velocities in the directions x and y, Re is the Reynolds number, and p the pressure. The initial conditions are

$$u(x,y,0)=-\cos x\sin y \quad \text{and} \quad v(x,y,0)=\sin x\cos y, \tag{4.21}$$

and boundary conditions at $x=0$, $x=\pi$, $y=0$ and $y=\pi$ are given by the following relations

$$u=-\cos x\sin y\; e^{-\frac{2t}{Re}} \quad \text{and} \quad v=\sin x\cos y\; e^{-\frac{2t}{Re}}. \tag{4.22}$$

The analytical solution of this problem is

$$u=-\cos x\sin y\; e^{-\frac{2t}{Re}},\;\; v=\sin x\cos y\; e^{-\frac{2t}{Re}} \text{ and } p=-\frac{1}{4}(\cos 2x+\sin 2y)\; e^{-\frac{4t}{Re}}. \tag{4.23}$$

Introducing stream-function ψ and vorticity ω, equations (4.18)-(4.20) can be rewritten as

$$\frac{\partial \omega}{\partial t}+u\frac{\partial \omega}{\partial x}+v\frac{\partial \omega}{\partial y}=\frac{1}{Re}\nabla^2\omega, \tag{4.24}$$

$$\nabla^2\psi=-\omega, \tag{4.25}$$

where the initial and boundary conditions for ψ and ω can be derived from equations (4.21) and (4.22). The pressure when needed, is obtained by solving the pressure Poisson equation,

$$\nabla^2 p = 2\left(\frac{\partial u}{\partial y}\frac{\partial v}{\partial x} - \frac{\partial u}{\partial x}\frac{\partial v}{\partial y}\right), \tag{4.26}$$

derived from equations (4.18)-(4.20).

Table 4.4: *Numerical and exact values of u and v at $\left(\frac{\pi}{4}, \frac{\pi}{10}\right)$ at different time levels, Re and grid sizes with $\Delta t = .01$.*

	u			v		
	Grid		Exact	Grid		Exact
	21×21	41×41		21×21	41×41	
$Re = 50$						
$t = 0.1$	-0.217643	-0.217636	-0.217636	0.669812	0.669814	0.669814
$t = 0.5$	-0.214222	-0.214184	-0.214181	0.659179	0.659182	0.659182
$t = 1.0$	-0.210011	-0.209945	-0.209940	0.646122	0.646129	0.646129
$Re = 10^2$						
$t = 0.1$	-0.218086	-0.218072	-0.218071	0.671153	0.671155	0.671155
$t = 0.5$	-0.216417	-0.216339	-0.216334	0.665802	0.665807	0.665807
$t = 1.0$	-0.214328	-0.214191	-0.214181	0.659168	0.659181	0.659182
$Re = 10^3$						
$t = 0.1$	-0.218523	-0.218473	-0.218464	0.672376	0.672364	0.672364
$t = 1.0$	-0.218684	-0.218155	-0.218071	0.671153	0.671154	0.671155
$t = 5.0$	-0.216842	-0.216435	-0.216334	0.665801	0.665807	0.665807
$Re = 10^4$						
$t = 0.1$	-0.218544	-0.218523	-0.218506	0.672511	0.672490	0.672485
$t = 1.0$	-0.219246	-0.218652	-0.218464	0.672383	0.672368	0.672364
$t = 5.0$	-0.218786	-0.218428	-0.218290	0.671832	0.671827	0.671826

Results for different time steps and grid sizes are shown in the Tables 4.4-4.6. Table 4.4 shows the numerical values (for grid sizes 21×21 and 41×41) of u and v for four Reynolds numbers, viz. 50, 100, 1000 and 10000, at different time levels at the point $\left(\frac{\pi}{4}, \frac{\pi}{10}\right)$ together with the exact solutions. The comparison of pressure obtained numerically (on 21×21, 41×41 and 81×81 grids) with the exact pressure at the mid-point at $t = 0.1$ for Reynolds numbers 100, 1000 and

Table 4.5: *Numerical and exact values of mid-point pressure for different Re at* $t = 0.1$ *for different grid sizes with* $\Delta t = .001$.

Re	Grid			Exact
	21×21	41×41	81×81	
100	0.495202	0.497305	0.497829	0.498004
1000	0.496933	0.499091	0.499624	0.499800
10000	0.497101	0.499273	0.499817	0.499998

Table 4.6: *Numerical and exact values of vorticity at different times for different grid sizes for* $Re = 10000$ *with* $\Delta t = .05$.

Time	Grid		Exact
	21×21	41×41	
0.1	1.344416	1.344832	1.344970
1.0	1.342599	1.344190	1.344728
5.0	1.342201	1.343248	1.343653

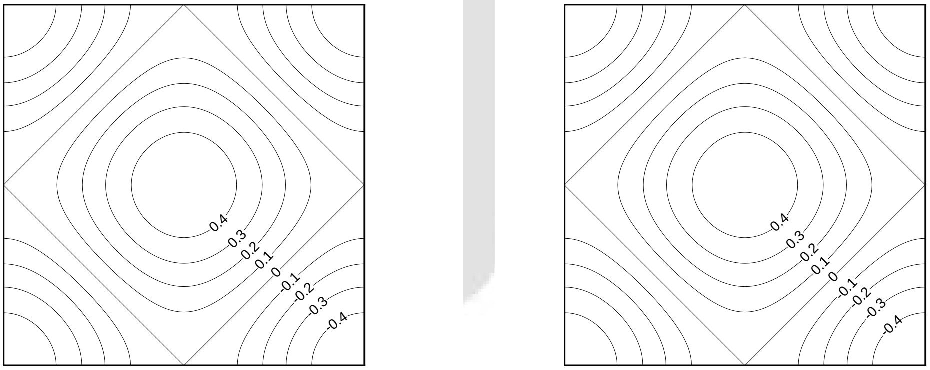

(a) (b)

Figure 4.8: *Pressure contours for* $Re = 100$ *at* $t = 0.1$ *for the (a) numerical and (b) exact results.*

10000 are shown in Table 4.5 and similar results for vorticity [at point $\left(\frac{\pi}{4}, \frac{\pi}{10}\right)$] are presented in Table 4.6 for $Re = 10000$ at three time levels $t = 0.1$,1.0 and

5.0 (on 21 × 21 and 41 × 41 grids) with $\Delta t = 0.05$. Figures 4.8 and 4.9 show the pressure and vorticity contours obtained through the present scheme for

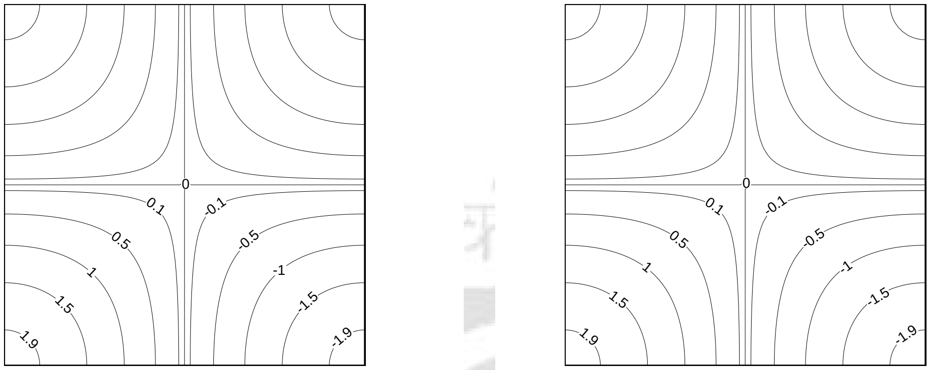

(a) (b)

Figure 4.9: *Vorticity contours for* $Re = 100$ *at* $t = 0.1$ *for the (a) numerical and (b) exact results.*

$Re = 100$ at time $t = 0.1$ along with their exact contours. It is seen from these figures that the exact and numerical contours are almost indistinguishable. Obviously, grid independence is achieved with a grid as coarse as 21 × 21. It has been observed that physically realistic results can be obtained even with a 11 × 11 grid. Strikwerda [71] mentions that his scheme is inadequate to provide realistic pictures of flows for Reynolds number higher than 100. However the present schemes are free from such limitations and results have been presented even for Reynolds number as high as 10000 (Tables 4.4-4.6).

4.4.3 Problem 3

In this example, the Taylor's vortex problem [13, 78] has been considered with the following initial conditions

$$u(x,y,0) = -\cos(Nx)\sin(Ny) \text{ and } v(x,y,0) = \sin(Nx)\cos(Ny) \;\forall\; 0 \le x, y \le 2\pi. \tag{4.27}$$

The exact solution of this problem is given by

$$u = -\cos(Nx)\sin(Ny)\, e^{-2N^2t/Re} \quad \text{and} \quad v = \sin(Nx)\cos(Ny)\, e^{-2N^2t/Re}, \tag{4.28}$$

where N is an integer. Figure 4.10 depicts the computed Taylor's vorticity

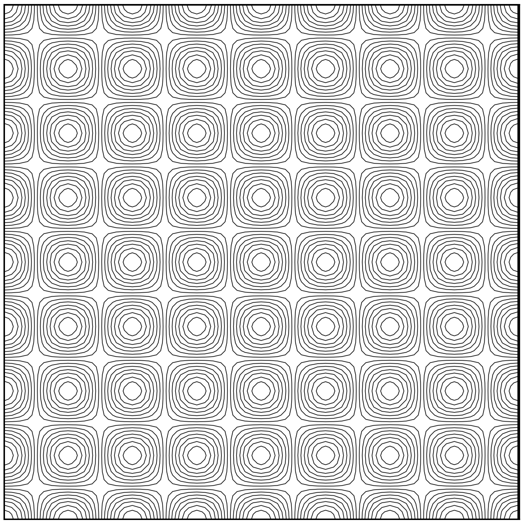

Figure 4.10: *Vorticity contours for the Taylor's vortex at $t = 2$ for $N = 4$ and $Re = 1000$ with $\Delta t = 0.01$.*

contours for $h = \dfrac{2\pi}{64}$, $Re = 1000$ and $N = 4$ at $t = 2$ with $\Delta t = 0.01$. The variations of the horizontal velocity along the vertical centreline and the vertical velocity along the horizontal centreline at time $t = 10$ and $Re = 100$ for N=1, 2 and 4, along with the exact solutions have been presented in Figures 4.11 and 4.12. Variations of the velocities on either sides of the axes exhibit identical behaviour with equal peak values.

It is seen that our results are in quite good agreement with the exact solutions. The percentage error [78] of the maximum velocity (either u or v) has been used to test the accuracy of the schemes. For $Re = 20$ and $N = 1$ at time

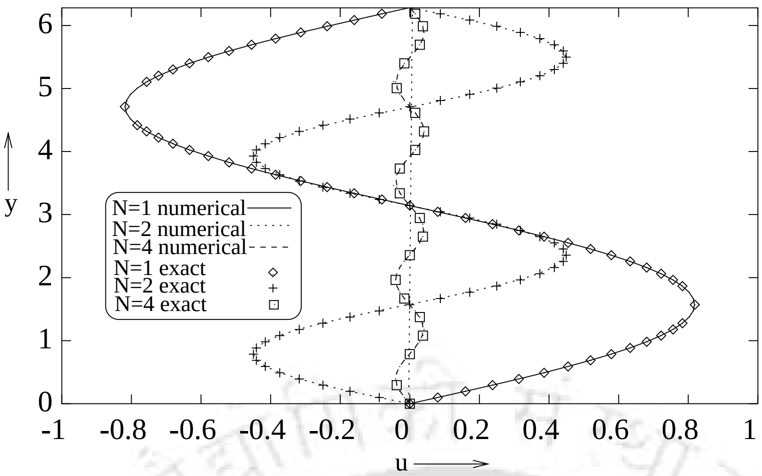

Figure 4.11: *Horizontal velocity along the vertical centreline for the Taylor's vortex problem at $t = 10$ for $N = 1, 2$ and 4, and $Re = 100$.*

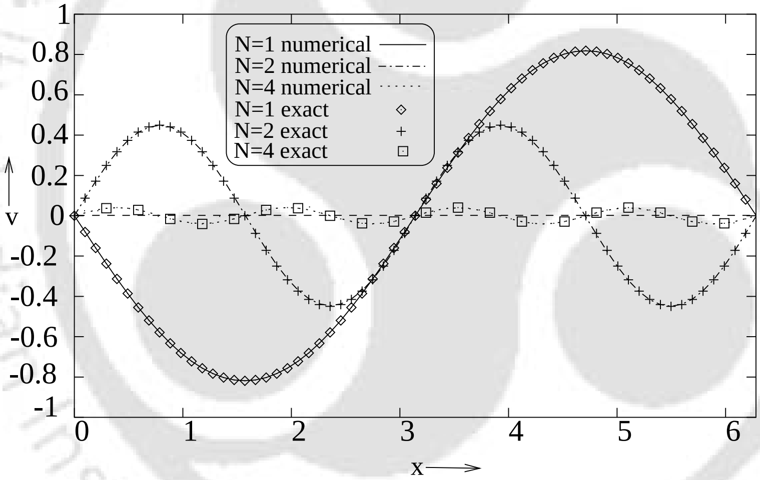

Figure 4.12: *Vertical velocity along the horizontal centreline for the Taylor's vortex problem at $t = 10$ for $N = 1, 2$ and 4, and $Re = 100$.*

$t = 10$ on a 65×65 grid, this error with the (9,9) scheme is found to be 0.0071%, which is much less than the minimum error 0.038% obtained in [13] with a grid size 129×129. For N =1, 2 and 4, the percentage errors of the scheme are 0.054, 0.170 and 0.802 respectively when $Re = 1000$.

4.4.4 Problem 4

The problem considered here is the 2D lid-driven cavity flow which is extensively used as a benchmark for code validation of the incompressible N-S equations. The cavity is defined by the square $0 \leq x, y \leq 1$. The governing equations are given by equations (4.18)-(4.20). The top wall of the cavity at $y = 1$ moving from left to right sets the fluid into motion. The velocities on that wall are $u = 1$ and $v = 0$, whereas on the other walls they are $u = v = 0$. The stream-function vorticity formulations have again been used here. A fourth order compact scheme for the Neumann boundary condition for vorticity has been adopted. For example, on the left wall, the approximation for the vorticity ω can be found from the relation $v = -\dfrac{\partial \psi}{\partial x}$, equations (4.24) and (4.25) as

$$\begin{aligned} & - \delta_x^+ \psi_{0j} - \left[\frac{h}{2} + \frac{h^2}{6}\delta_x^+ - \frac{h^3}{24}(Rev_{0j}\delta_y - \delta_y^2)\right]\omega_{0j} \\ & = v_{0j} - \frac{h^3}{24}(\delta_x^+\delta_y^2 v_{0j} - \delta_t^+ \omega_{0j}), \end{aligned} \tag{4.29}$$

where the suffixes 0 and j stand for the left wall and the vertical index respectively. This results in an explicit expression for ω on the left wall. Vorticities on the other walls can be found in a similar way and for the corners, a third order scheme [67] has been used.

Computations are carried out using uniform grids of sizes 41×41, 81×81 and 121×121 with a time step $\Delta t = 0.0125$ for $Re = 100$ and 1000. Steady-state results have been compared with those of Ghia *et al.* [24] and Spotz [64]. Table 4.7 depicts the steady-state values of ψ, ω and the location of the primary and the secondary bottom vortices along with their horizontal and vertical lengths $[(H_l)$ and $(V_l)]$ for $Re = 1000$. Comparisons with the results of Ghia *et al.* [24] and the best results of ref. [64] show very good agreement. Figures 4.13 and 4.14 show the steady-state contours of stream-function and vorticity respectively for $Re = 100$ and 1000. It is seen from the figures that though the centre of the primary vortex is offset towards the top right corner for $Re = 100$, with increasing Re, it moves towards the geometric

Table 4.7: *Steady-state vortex data for the lid-driven cavity problem for* $Re = 1000$ $(\Delta t = 0.0125)$.

Vortex	Method	ψ	ω	(x, y)	H_l	V_l
Primary	Present	-0.1188	-2.0618	(0.5333, 0.5750)	$---$	$---$
	Ghia	-0.1179	-2.0497	(0.5313, 0.5625)	$---$	$---$
	Spotz	-0.1172	-2.0533	(0.5250, 0.5750)	$---$	$---$
Bottom left	Present	0.00023	0.3328	(0.0833, 0.0750)	0.2156	0.1692
	Ghia	0.00023	0.3618	(0.0859, 0.0781)	0.2188	0.1680
	Spotz	0.00017	0.2392	(0.0750, 0.0750)	0.2189	0.1641
Bottom right	Present	0.00177	1.1162	(0.8667, 0.1167)	0.3023	0.3493
	Ghia	0.00175	1.1547	(0.8594, 0.1094)	0.3034	0.3536
	Spotz	0.00173	1.0441	(0.8750, 0.1250)	0.3067	0.3856

centre of the cavity (Figure 4.13). Also, as Re increases, several regions of high vorticity gradients, indicated by concentration of the vorticity contours, appear within the cavity (Figure 4.14). Figure 4.15 compares the horizontal velocity along the vertical centreline with the results of Ghia *et al.* [24]. A similar comparison for the vertical velocity along the horizontal centreline has been shown in Figure 4.16. Agreement in both the cases is excellent. The steady-state vorticity distribution on the moving wall obtained by Ghia *et al.* [24] and on all the four walls obtained by the present (9,9) scheme are shown for $Re = 100$ and 1000 in Figures 4.17 and 4.18. In case of the moving wall, there is some oscillation in the vorticity profile at the left end, as reported by Spotz and Carey [66, 67] for fourth order accurate boundary conditions. In general the solutions obtained through the present scheme, even on a coarser grid, are in excellent agreement with the well-established results.

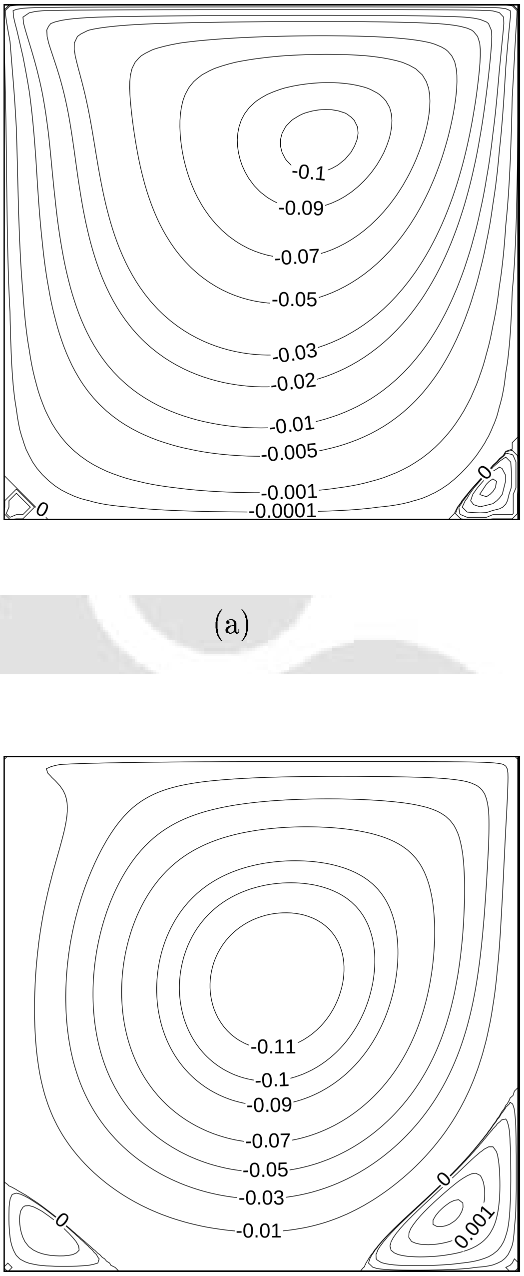

(a)

(b)

Figure 4.13: *Steady-state stream-function contours for the lid-driven cavity problem at (a)* $Re = 100$ *and (b)* $Re = 1000$.

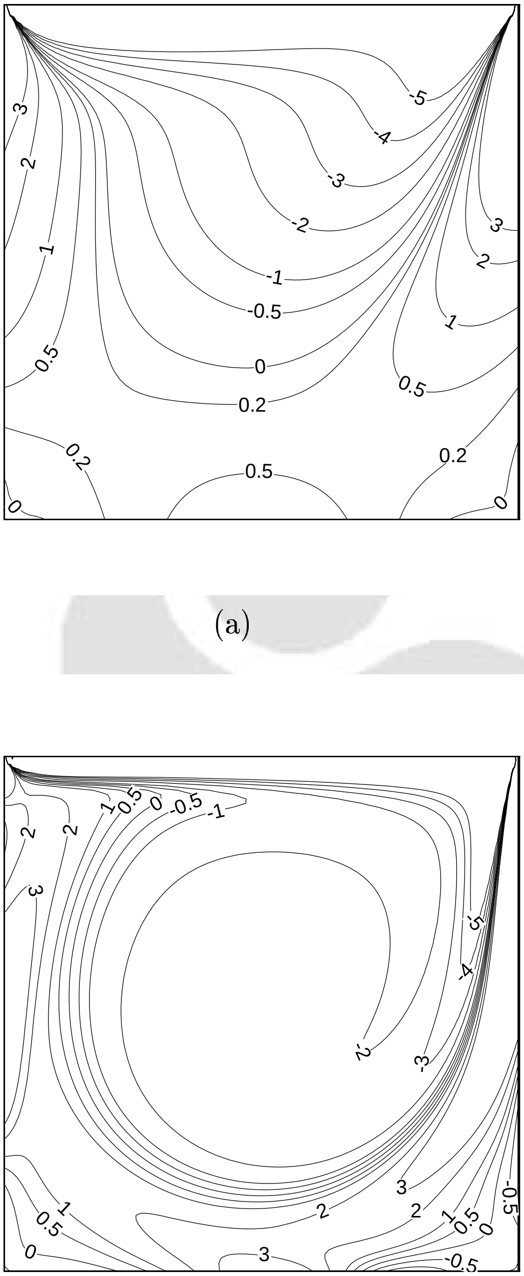

(a)

(b)

Figure 4.14: *Steady-state vorticity contours for the lid-driven cavity problem at (a)* $Re = 100$ *and (b)* $Re = 1000$.

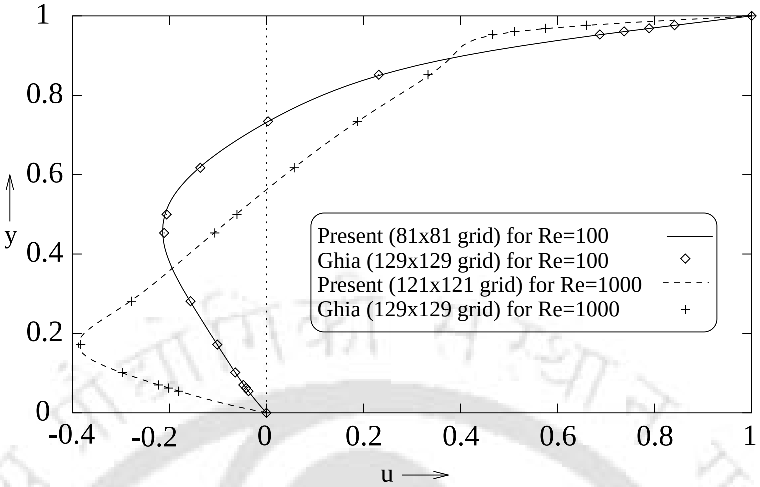

Figure 4.15: *Steady-state results of the lid-driven cavity problem: the horizontal velocity along the vertical centreline for* $Re = 100$ *and 1000.*

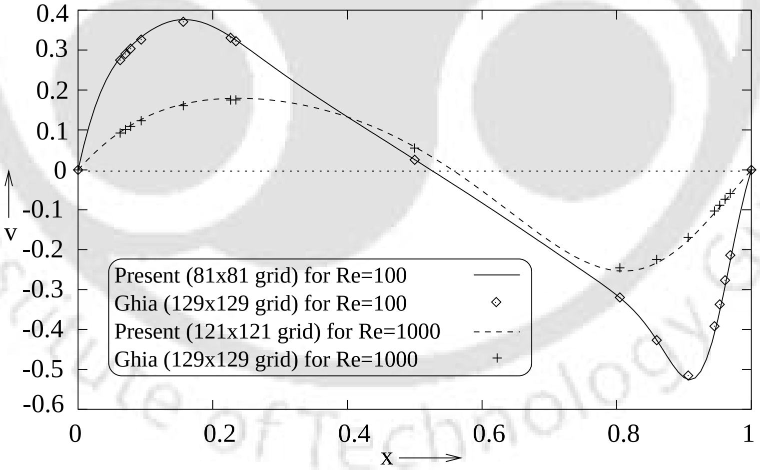

Figure 4.16: *Steady-state results of the lid-driven cavity problem : the vertical velocity along the horizontal centreline for* $Re = 100$ *and 1000.*

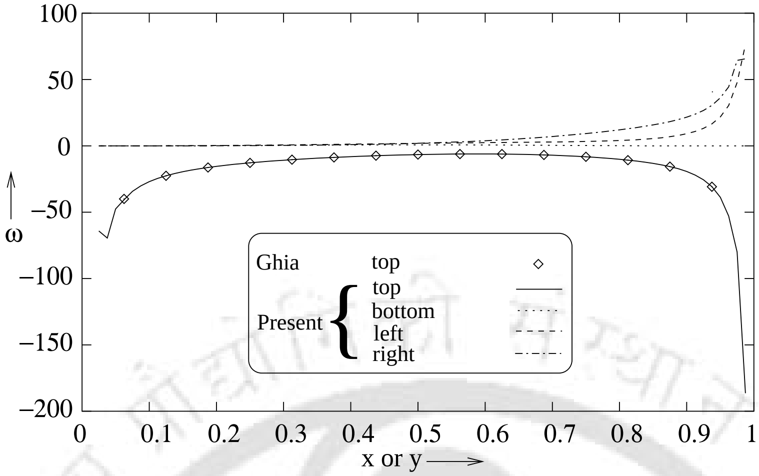

Figure 4.17: *Steady-state vorticity on the four boundaries of the cavity for* $Re = 100$.

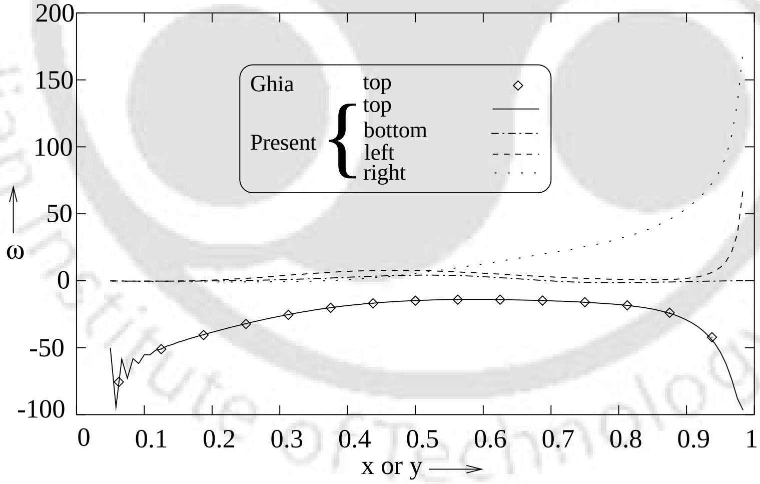

Figure 4.18: *Steady-state vorticity on the four boundaries of the cavity for* $Re = 1000$.

4.5 Conclusion

A class of implicit HOC finite difference schemes has been developed with weighted time discretization to solve the unsteady 2D variable coefficient convection-diffusion equation. Both Dirichlet and Neumann boundary conditions can easily be incorporated into the schemes. A linear stability analysis shows that the schemes are unconditionally stable for $0.5 \leq \mu \leq 1$. The schemes are second or first order accurate in time according as $\mu = 0.5$ or otherwise, and fourth order accurate in space. In a departure from the rigidity of usual HOC schemes, the present schemes have been developed for a grid aspect ratio which need not necessarily be unity. Three schemes viz. (9,5), (9,9) and (5,9) for $\mu = 0$, 0.5 and 1 respectively have been investigated. They are easy to implement and the use of conjugate gradient and a hybrid biconjugate gradient stabilized algorithms for solving the algebraic systems arising at every time level, makes the implicit procedure computationally efficient even in capturing transient solutions. To bring out different aspects of the schemes, they have been employed to compute the transient solutions of three 2D linear and nonlinear convection-diffusion problems and the time marching steady solution of the 2D lid-driven cavity flow problem. The robustness of the schemes is illustrated by their applicability to the wide range of problems of varying physical complexities represented, among others, by Reynolds numbers ranging from 50 to 10000. Computational efficiency of these schemes is reflected by the low demand on CPU time. This is substantiated by a comparison of the CPU time with an implicit scheme of identical temporal accuracy by Noye and Tan. The results obtained in all the four test cases with coarser grids are in excellent agreement with the analytical as well as established numerical results, underlining the high accuracy of the schemes. The implicit nature of the schemes is fully exploited in arriving at the steady-state results for the lid-driven cavity problem, where time-steps as high as 0.5 has been employed for some of the computations. Because of being HOC in space, second order accurate in time and implicit in nature, the $(9, 9)$ scheme in particular seems to have good potential for efficient application to many problems of incompressible viscous flows. This will be seen from the simulation of flows due to double-diffusive natural convection in a vertical annulus between two concentric cylinders in the next chapter.

Chapter 5

HOC SIMULATION OF DOUBLE-DIFFUSIVE NATURAL CONVECTION IN A VERTICAL POROUS ANNULUS

5.1 Introduction

The phenomenon of natural convection in fluid saturated porous medium due to the combined effects of temperature and concentration gradients can be found quite extensively, both in nature and technology. Technological applications include grain storage installations, migration of moistures through air contained in fibrous insulation, energy storage in solar ponds, contaminant transport in saturated soils and underground disposal of nuclear waste. Double-diffusive flows in porous media are also seen in geophysical systems, electrochemistry and metallurgy. All these factors have contributed to the recent growth of interest in the study of this phenomenon, either experimental or theoretical. Since analytical results could be found only for a very small range of the large numbers of parameters present in the governing equations, numerical simulation has been the most popular choice for this physical configuration. Moreover, recent advances in numerical techniques has made possible computations for those range of parameters, which have so far been beyond the reach of analytical or numerical studies.

Earlier, most of the theoretical, experimental or numerical studies in natural convection in porous media were confined mainly to double-diffusion in rectangular cavities. For example, Trevisan and Bejan [73, 74] investigated heat and mass transfer by natural convection in a rectangular cavity subjected to various boundary conditions. They developed an analytical Oseen-linearized solution for the boundary layer regime valid for Lewis number $Le = 1$, and a similarity solution for heat-transfer-driven flows for $Le > 1$. Apart from these, an extensive series of numerical experiments had also been carried out by them to validate the analytical results and provide heat and mass transfer data for the domain not covered by analysis. Recently, Alavyoon and his co-workers have re-investigated the case considered in ref. [74] for aiding ($N > 0$) [2] and opposing ($N < 0$) [3] heat and mass fluxes, N being the buoyancy ratio. Besides applying scale analysis to the two extreme cases of heat- and solute-driven natural convection, they also obtained analytical solutions, valid for stratified flow in slender cavities. More recently, Mamou *et al.* [43] have demonstrated the existence of multiple steady solutions for square cavities for opposing flows. They have further discussed the effect of the governing parameters on the domain of existence of these multiple solutions. Also, flow structure and convective heat transfer in a vertical porous annulus under the condition of constant heat flux or isothermal heating or cooling along the vertical side walls have been analyzed earlier both experimentally and numerically, but only for a single component (i.e., either temperature or concentration gradient). For example, theoretical and numerical studies of Havstad and Burns [27], the experimental studies of Reda [55] and the series of experimental [50,51] and numerical [48,49] studies by Prasad and co-workers were all confined to natural convection due to temperature gradients only.

Thus, it is seen that most of the earlier investigators mainly focussed their attention either on the study of double-diffusive natural convection in 2D rectangular cavities or of natural convection due to temperature gradient only in a vertical porous annulus. However, the rectangular models do not always adequately represent the more practical situations in which the cavity is a porous annulus bounded by two vertical concentric cylinders. Likewise, in fluid mixtures saturating the porous media, where the variation of fluid density is induced by both temperature and solute, the dynamics of heat and mass transfer can be very different from those driven by temperature distribution only. The present study investigates numerically the double-diffusive natural convection in a porous medium bounded by two vertical coaxial cylinders for a wide range of the parameters governing the flow. Special emphasis has been given to simulation of the flow in the annulus for an aspect ratio $A = 5$. It is seen that, in most of the numerical studies for this physical configuration [10, 44, 60, 61], spatially second-order accurate schemes, with some form of the pressure-correction algorithms by Patankar [47] have been used. The present study which uses the $(9, 9)$ transient higher-order compact (HOC) scheme [35] developed in Chapter 4 is perhaps the only attempt till date where an HOC algorithm has been applied to simulate flow involving both heat and mass transfer. The work has two main objectives: firstly, to test the efficiency of the present HOC scheme for the flow configuration under consideration and secondly to compute the flow features for certain domains of the flow parameters not explored earlier. It is found that the results obtained here on relatively coarser grids, as can be expected of an HOC scheme, compare very well with numerical results wherever available.

5.2 The Problem

The problem considered here is the flow in a rigid cylindrical annulus of height H, whose inner and outer radii are $r_i^{'}$ and $r_o^{'}$ respectively, as shown in Figure 5.1. The annulus is filled with a fluid saturated porous medium. All boundaries of the annular cavity are impermeable and the inner and outer walls are maintained at different uniform temperatures $T_h^{'}$ and $T_c^{'}$ $(T_h^{'} > T_c^{'})$, and con-

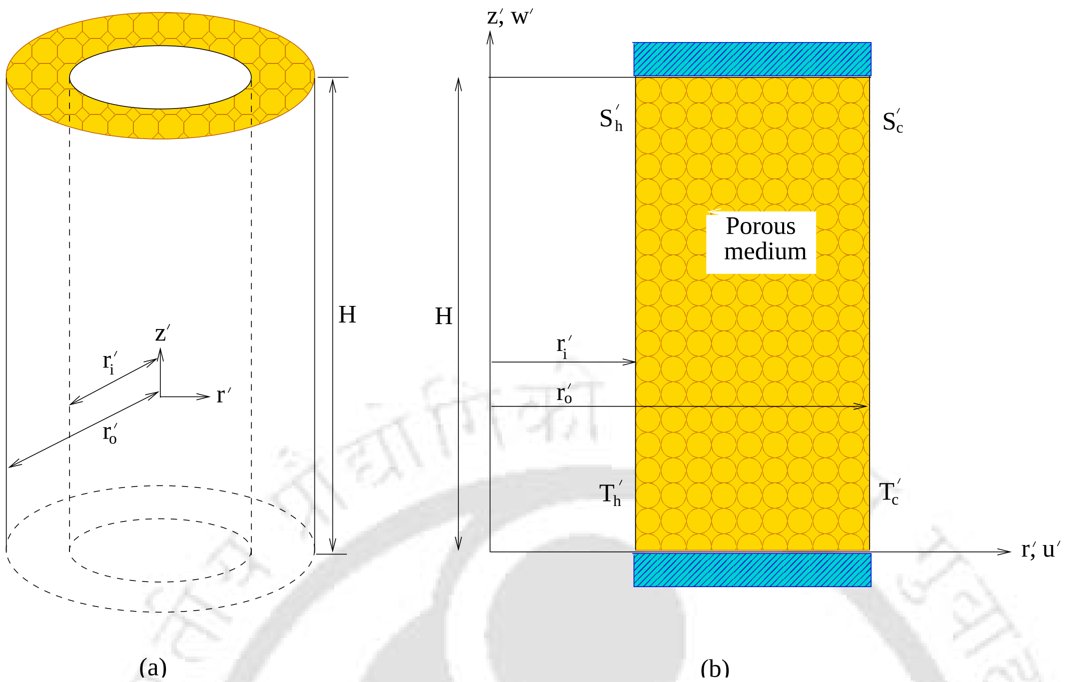

Figure 5.1: *Schematic view of the vertical porous annulus.*

centrations $S_h^{'}$ and $S_c^{'}$ ($S_h^{'} > S_c^{'}$) respectively. The top and bottom boundaries of the enclosure are insulated and in the porous medium, Darcy's law is assumed to hold. The classical hypotheses used in this study are: (i) the Dufour effect (heat flux produced by concentration gradient) is ignored, (ii) the Soret effect (mass flux produced by temperature gradient) is ignored and (iii) the fluid is assumed to be a Boussinesq fluid, i.e. both the porous matrix and the saturating fluid are incompressible, and all thermo-physical properties of the medium are constant, except density of the mixture which varies linearly with temperature and concentration as:

$$\rho(T^{'}, S^{'}) = \rho_r \left[1 - \beta_T \left(T^{'} - T_r^{'}\right) - \beta_S \left(S^{'} - S_r^{'}\right)\right] \tag{5.1}$$

where ρ_r is the density at $T^{'} = T_r^{'}$, $S^{'} = S_r^{'}$ and β_T, β_S are the thermal and solutal expansion coefficients respectively.

Under these assumptions, the equations governing the conservation of mass, momentum, heat and concentration in cylindrical polar co-ordinates $(r^{'}, z^{'})$

can be written as [10]

$$\frac{\partial}{\partial r'}\left(r'u'\right)+\frac{\partial}{\partial z'}\left(r'w'\right)=0, \tag{5.2}$$

$$u'=-\frac{K}{\mu}\frac{\partial p'}{\partial r'}, \tag{5.3}$$

$$w'=-\frac{K}{\mu}\left(\frac{\partial p'}{\partial z'}+\rho g\right), \tag{5.4}$$

$$\sigma\frac{\partial T'}{\partial t'}+u'\frac{\partial T'}{\partial r'}+w'\frac{\partial T'}{\partial z'}=\alpha\nabla'^2T', \tag{5.5}$$

$$\epsilon'\frac{\partial S'}{\partial t'}+u'\frac{\partial S'}{\partial r'}+w'\frac{\partial S'}{\partial z'}=D\nabla'^2S' \tag{5.6}$$

where

$$\nabla'^2=\frac{1}{r'}\frac{\partial}{\partial r'}\left(r'\frac{\partial}{\partial r'}\right)+\frac{\partial}{\partial z'^2}$$

and u', w', K, μ, p', ρ, g, T', S', α, D and ϵ' indicate r' and z' components of Darcy velocity, permeability of the porous medium, fluid viscosity, pressure, fluid density, gravitational acceleration, temperature, concentration, thermal diffusitivity, solutal diffusitivity and porosity of the porous medium. The heat capacity σ is defined as

$$\sigma=\frac{\epsilon'(\rho C)_f+\left(1-\epsilon'\right)(\rho C)_p}{(\rho C)_f}$$

where $(\rho C)_f$ and $(\rho C)_p$ are the heat capacity of the fluid and the saturated porous medium respectively.

The boundary conditions for the governing equations are

$$r'=r_i',\quad T'=T_h',\quad S'=S_h',\quad u'=0. \tag{5.7}$$

$$r^{'} = r_o^{'}, \quad T^{'} = T_c^{'}, \quad S^{'} = S_c^{'}, \quad u^{'} = 0. \tag{5.8}$$

$$z^{'} = 0,\ H; \quad \frac{\partial T^{'}}{\partial z^{'}} = \frac{\partial S^{'}}{\partial z^{'}} = 0, \quad w^{'} = 0. \tag{5.9}$$

Introducing the dimensionless variables,

$$\begin{gathered}
(r,\ z) = \frac{(r^{'},\ z^{'})}{H}, \\
(u,\ w) = \frac{(u^{'},\ w^{'})H}{\alpha}, \\
t = \frac{t^{'}\alpha}{H^2\sigma}, \\
p = \frac{p^{'}H^2}{\rho\alpha^2}, \\
T = \frac{T^{'} - T_r^{'}}{\Delta T^{'}}, \quad S = \frac{S^{'} - S_r^{'}}{\Delta S^{'}}, \\
T_r^{'} = \frac{T_h^{'} + T_c^{'}}{2}, \quad S_r^{'} = \frac{S_h^{'} + S_c^{'}}{2}, \\
\Delta T^{'} = T_h^{'} - T_c^{'} \quad \text{and} \quad \Delta S^{'} = S_h^{'} - S_c^{'},
\end{gathered}$$

the non-dimensional governing equations may be written as

$$\frac{\partial}{\partial r}(ru) + \frac{\partial}{\partial z}(rw) = 0, \tag{5.10}$$

$$u = -\frac{\partial p}{\partial r}, \quad w = -\frac{\partial p}{\partial z} + Ra\,(T + NS)\,, \tag{5.11}$$

$$\frac{\partial T}{\partial t} + u\frac{\partial T}{\partial r} + w\frac{\partial T}{\partial z} = \nabla_1^2 T, \tag{5.12}$$

$$\epsilon\frac{\partial S}{\partial t} + u\frac{\partial S}{\partial r} + w\frac{\partial S}{\partial z} = \frac{1}{Le}\nabla_1^2 S \tag{5.13}$$

with $\nabla_1^2 = \frac{1}{r}\frac{\partial}{\partial r}\left(r\frac{\partial}{\partial r}\right) + \frac{\partial}{\partial z^2}$. The dimensionless boundary conditions are

$$r = \frac{1}{A(\kappa - 1)}, \quad T = 0.5, \quad S = 0.5, \quad u = 0, \tag{5.14}$$

$$r = \frac{\kappa}{A(\kappa - 1)}, \quad T = -0.5, \quad S = -0.5, \quad u = 0, \tag{5.15}$$

$$z = 0, 1; \quad \frac{\partial T}{\partial z} = \frac{\partial S}{\partial z} = 0, \quad w = 0 \tag{5.16}$$

where $A = \frac{H}{r'_o - r'_i}$ is the aspect ratio defining the slenderness of the cavity, $\kappa = \frac{r'_o}{r'_i}$ is the radius ratio, $Ra = \frac{Kg\beta_T\Delta T' H}{\nu\alpha}$ (ν being the kinematic viscosity) is the thermal Rayleigh number, $N = \frac{\beta_S \Delta S'}{\beta_T \Delta T'}$ is the buoyancy ratio measuring the relative significance of species and thermal diffusion, $Le = \frac{\alpha}{D}$ is the Lewis number representing the ratio between the thermal and solutal diffusivities and lastly, $\epsilon = \frac{\epsilon'}{\sigma}$ is the normalized porosity of the porous medium. It may be mentioned that in the expressions for N, the thermal expansion coefficient β_T is positive for most of the fluids at ordinary temperature and pressure, whereas the solutal expansion coefficient β_S can also be negative which indicates opposing flow.

Now introducing dimensionless stream-function ψ defined by

$$u = -\frac{1}{r}\frac{\partial \psi}{\partial z}, \quad w = \frac{1}{r}\frac{\partial \psi}{\partial r}, \tag{5.17}$$

the equations (5.10) and (5.11) can be written as

$$\frac{\partial^2 \psi}{\partial r^2} - \frac{1}{r}\frac{\partial \psi}{\partial r} + \frac{\partial^2 \psi}{\partial z^2} = rRa\left(\frac{\partial T}{\partial r} + N\frac{\partial S}{\partial r}\right) \tag{5.18}$$

with $\psi = 0$ on the boundaries. Thus equations (5.12), (5.13), (5.17) and (5.18) together with the boundary conditions (5.14)-(5.16) completely define the problem in terms of the dimensionless parameters A, κ, Ra, Le, N and ϵ.

In most of the engineering applications, the overall heat and mass transfer characteristics are summarized by the Nusselt number Nu and the Sherwood number Sh respectively. The local Nu and Sh along the inner radial wall is defined by

$$Nu_i = \left.\frac{\partial T}{\partial r}\right|_{r=\frac{1}{A(\kappa-1)}} \tag{5.19}$$

and

$$Sh_i = \left.\frac{\partial S}{\partial r}\right|_{r=\frac{1}{A(\kappa-1)}} \tag{5.20}$$

Integrating these local Nu and Sh along the inner radial wall, the average Nusselt number $\overline{Nu}$ and the average Sherwood number $\overline{Sh}$ are obtained as

$$\overline{Nu_i} = \int_0^1 Nu_i dz \tag{5.21}$$

and

$$\overline{Sh_i} = \int_0^1 Sh_i dz \tag{5.22}$$

The corresponding values at the outer wall are given by

$$\overline{Nu_o} = \frac{\overline{Nu_i}}{\kappa} \tag{5.23}$$

and

$$\overline{Sh_o} = \frac{\overline{Sh_i}}{\kappa}. \tag{5.24}$$

5.3 Discretization of the Governing Equations

A slightly different approach is adopted to discretize the governing equations for the present case. As the governing equations are in cylindrical polar coordinates, they are restructured so as to fit into the unsteady HOC scheme. For example, the concentration equation (5.13) can be written as

$$\epsilon Le\frac{\partial S}{\partial t} + \left(Leu - \frac{1}{r}\right)\frac{\partial S}{\partial r} + Lew\frac{\partial S}{\partial z} - \nabla^2 S = 0 \tag{5.25}$$

where $\nabla^2 = \frac{\partial^2}{\partial r^2} + \frac{\partial^2}{\partial z^2}$. Similar expressions can be found for the other governing equations as well. Firstly equation (5.18) is solved; then the value of

ψ is used to calculate the values of u and w from (5.17) using a fourth order compact approximation [36]. The values of u and w found in this way are substituted in (5.12) and (5.13) to find T and S.

The boundary conditions for temperature and concentration in the present configuration are Dirichlet for the vertical walls and Neumann for the horizontal ones. Jensen's [56] 4th order accurate one sided formula is used for the Neumann boundary conditions as well as the derivatives appearing in the expressions for local Nu and Sh.

Flow simulations are carried out using grid sizes ranging from 21×21 to 65×641 depending upon the aspect ratio A. The time marching strategy is adopted till a steady-state is reached. As in the lid-driven cavity problem (Problem 4, Chapter 4), the governing equations being highly nonlinear, solution proceeds by iteration and BiCG algorithm [37, 62] have been used for all the equations. The convergence criterion for the inner iterations are set at $\max_{ij} |\phi^{\text{old}} - \phi^{\text{new}}| < 10^{-5}$ where ϕ is a variable for which solution is sought. The steady-state is assumed to reach when for the outer iterations, $\max_{ij} |\phi^{(n+1)} - \phi^{(n)}| < 10^{-7}$, n standing for the time level.

5.4 Results and Discussion

For the present physical configuration considered, six non-dimensional parameters, viz. aspect ratio A, radius ratio κ, Lewis number L, buoyancy ratio N, normalized porosity ϵ and thermal Rayleigh number Ra are important. In the actual calculations, ϵ is set to unity. Because of the presence of so many parameters, an extensive parametric investigation of the problem is beyond the scope of this study. As such, the large number of computations that has been reported in this chapter for all the parameters involved, represents only a sample of the full blown parametric investigation. It is found that, higher the absolute values of the parameters, greater the complexities associated with the flow, both in physics and numerics. This could be one of the reasons that the higher values of the parameters were not attempted in the earlier computations, most of which were carried out with lower-order accurate schemes. Contrary to this, the high accuracy of the present scheme coupled with the compactness of the difference stencils affords highly efficient and accurate simulation of the flow for a wide range of the parameters on relatively coarser grids. Computations carried out in this study are for $-50 \leq N \leq 50$, $1 \leq A \leq 10$, $1 \leq \kappa \leq 50$, $0 \leq Ra \leq 5000$ and $1 \leq L \leq 500$. Some of the ranges of the parameters have not been explored earlier probably because of computational difficulties. Systematic efforts have been made to illustrate the effects of different parameters on the steady-state solution.

5.4.1 Validation of Algorithm and Code

There are very few quantitative experimental or numerical data available for the parameters considered in the present study. Therefore, the validation of the present algorithm is first done through a comparison exercise for a range of parameters for which reliable qualitative and quantitative numerical results [10, 49] are available. The parameters chosen are $Ra = 500$, $N = 0$, $Le = 10$, $A = 1$, and $\kappa = 1$ and 5, which represents two cases for which the validation exercise is carried out. Grid-independent results of the present algorithm for the maximum stream-function value is compared with those of [10] in Table 5.1. The corresponding isotherms and, isoconcentration and stream-function

Table 5.1: *Grid independence study for* $A = 1$, $Le = 10$, $N = 0$ *and* $Ra = 500$.

κ	Grid	ψ_{max}
1	21×21	1381.63
	41×41	1364.39
	81×81	1363.24
	Beji *et al.* [10]	1359.00
5	21×21	7.9893
	41×41	7.8539
	81×81	7.8160
	Beji *et al.* [10]	7.6310

contours for the two cases are shown in figure 5.2 and they are very similar to those reported by, for example, Beji *et al.* [10] and Prasad and Kulacki [48]. The close comparison thus lends confidence in the present algorithm and code, which can be used now for the range of parameters not explored earlier. Also demonstrated in Table 5.1 is a notable merit of the present algorithm in that grid-independent results for the two cases are obtained on grids as coarse as 21×21. What follows in the next few sections, are the results of our systematic investigation for a wide range of parameters.

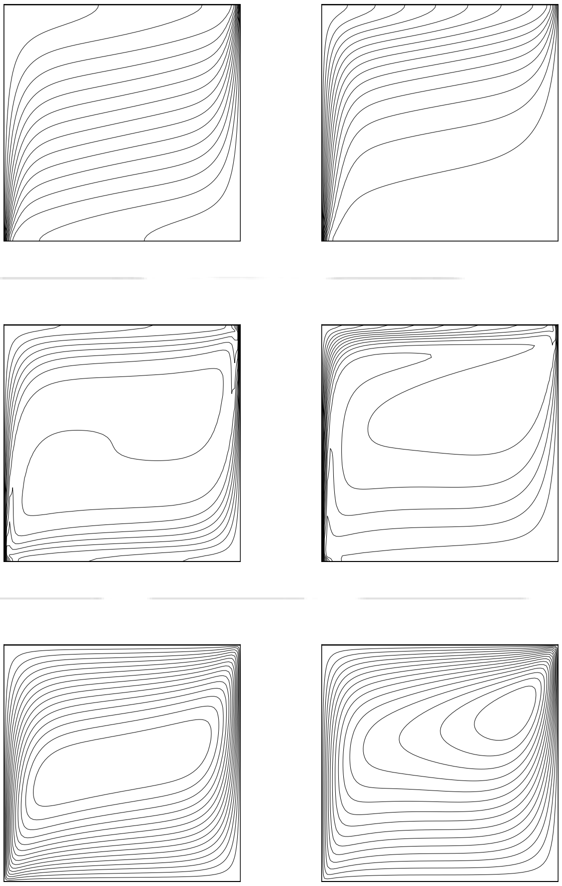

Figure 5.2: *Isotherms, isoconcentrates and the streamlines for* $N = 0$, $A = 1$, $Ra = 500$, $Le = 10$ *and* $\kappa = 1$ *(left) and* $\kappa = 5$ *(right).*

5.4.2 Influence of Aspect Ratio

The results for aspect ratios varying from 1 to 10 are presented in Figs 5.3 and 5.4 for $Ra = 500$, $\kappa = 2$, $Le = 10$ and $N = 5$. For $A > 5$, Ra and N considered in the present study are much higher than those of earlier studies [44, 48]. As the value of the buoyancy ratio N signifies, the flow is driven by moderately high solutal gradients. At $A = 1$ and 2, [Figs. 5.3 (a) and (b), centre] the concentration field is rather uniform at the central part of the cavity and gradients are sharper near the horizontal walls. Stratification of the flow is observed as A increases [Fig. 5.3 (centre)]. Fig. 5.4 (b) also confirms this fact where it can be seen that isoconcentrates spread further away from the vertical walls as A increases. It is seen that as radius increases, concentration sharpely drops near the inner wall and remain more or less same thereafter until it drops further in the vicinity of the outer wall. Obviously, the mass species boundary layers are thinner than the thermal boundary layers because of the lower diffusivity of mass species [Fig. 5.3 (top and centre)]. With the increase in A, the isotherms from a roughly diagonal shape, become more and more vertical [Fig. 5.3 (top)]. At high aspect ratio (particularly at $A = 8$ to 10), the temperature at the core of the cavity varies almost linearly in the horizontal direction [Fig. 5.4 (a)]. Here, the temperature profile nearly looks like that of pure conduction. Fig 5.4 (c) shows the variation of Nusselt and Sherwood numbers with aspect ratios. It is seen that the Sherwood number approaches a constant value asymptotically. With the increase in A, hydrodynamic boundary layers at the top and bottom walls become thicker and the vortex centre shifts slightly toward the upper region [figures 5.3 (a)-(f)]. Also the flow becomes weaker, which is indicated by the fall in the value of $|\psi_{max}|$. Hydrodynamic boundary layers grow at the vertical walls with the layer being more prominent at the cold wall.

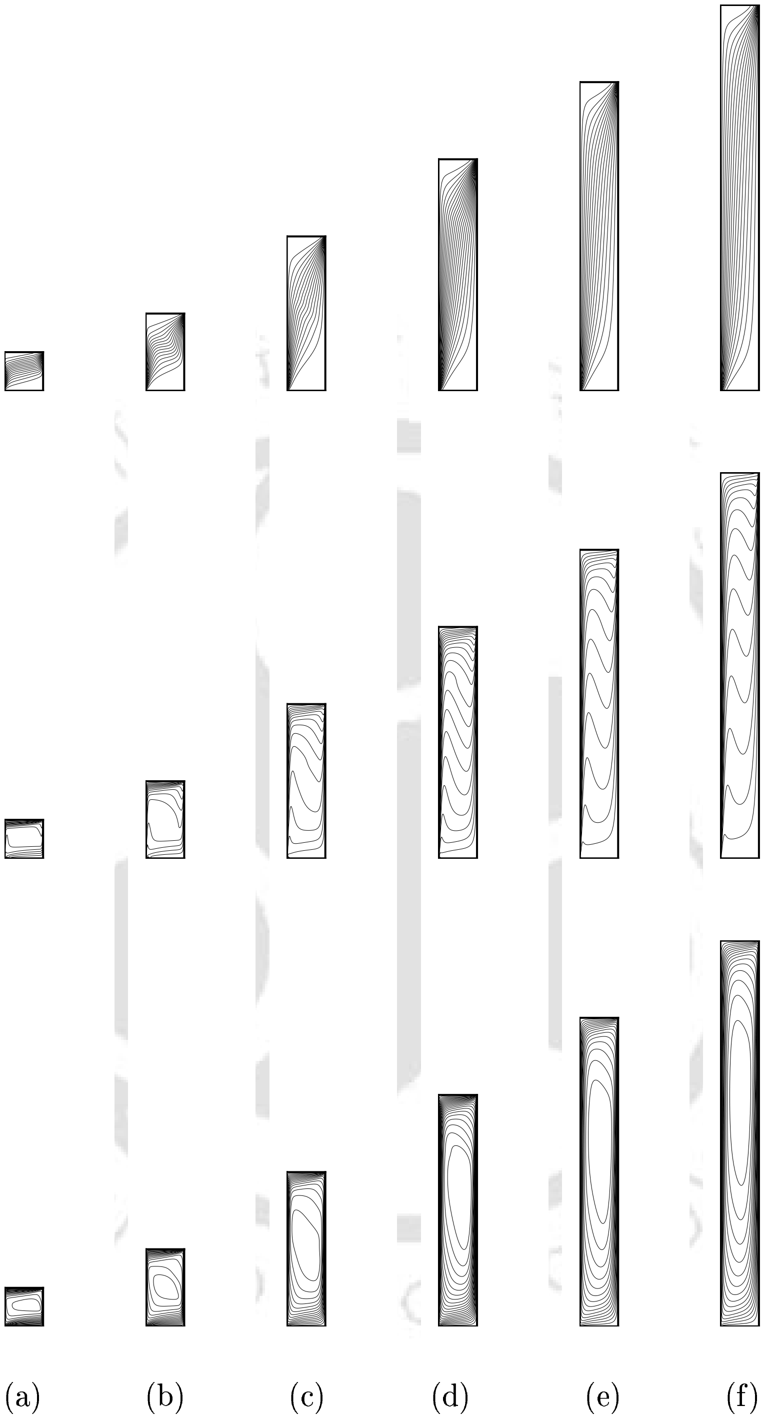
(a) (b) (c) (d) (e) (f)

Figure 5.3: *Temperature (top), concentration (centre) and stream-function (bottom) contours for* $\kappa = 2$, $Le = 10$, $Ra = 500$, $N = 5$ *and various values of* $A = 1$, *2, 4, 6, 8 and 10 (from left to right in that order).*

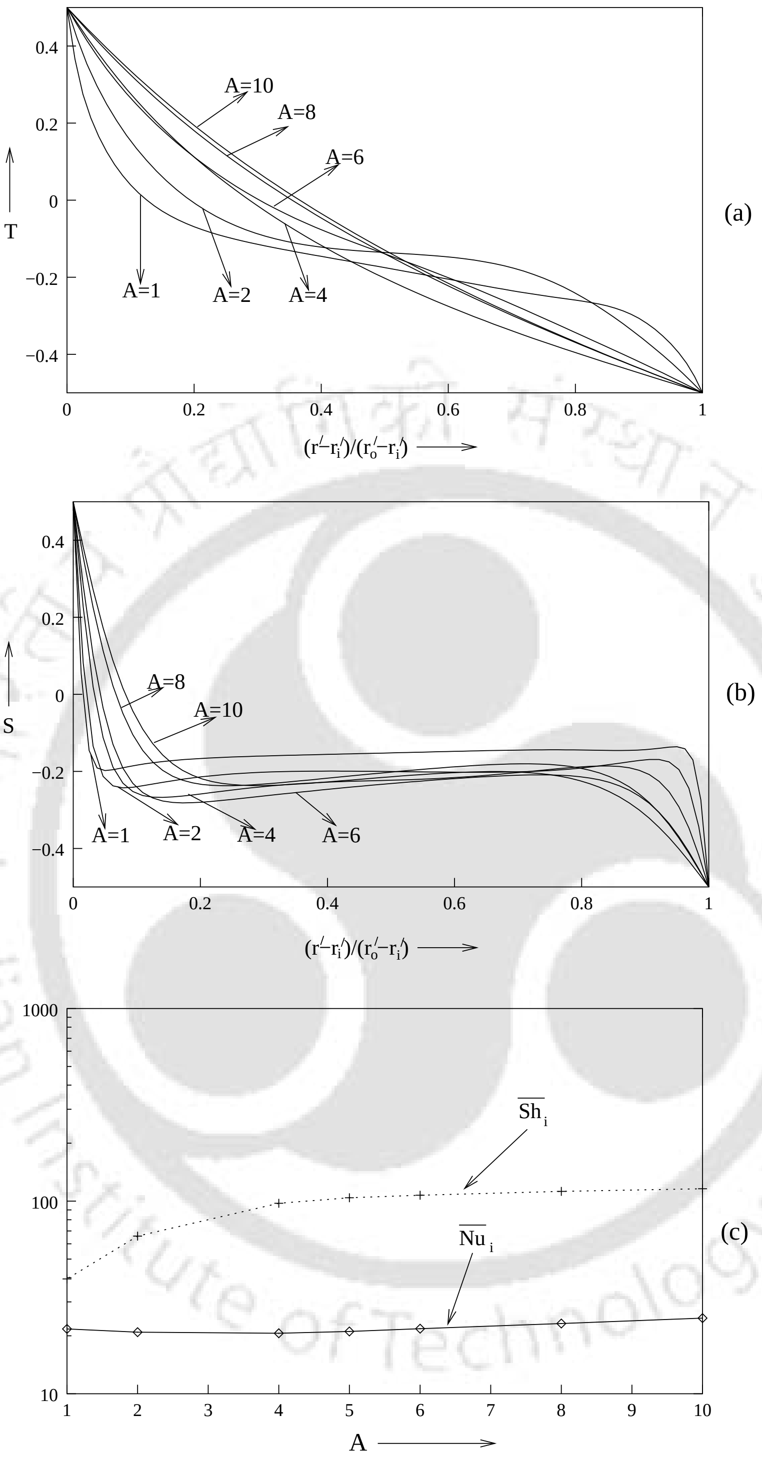

Figure 5.4: *Variations of (a) temperature and (b) concentration along the horizontal centreline and (c) average Nusselt and Sherwood numbers with respect to aspect ratio A for $\kappa = 2$, $Le = 10$, $Ra = 500$ and $N = 5$.*

5.4.3 Influence of Radius Ratio

Here, computations are carried out in the range $1 \leq \kappa \leq 50$ for $A = 5$, $Le = 10$, $Ra = 500$ and $N = 5$. The influence of increasing radius ratio is to impart asymmetry to the flow. As also can be seen from Fig. 5.2 (left) and Fig. 5.5 (a), for $\kappa = 1$, a centrosymmetry exists about the geometric centre of the cavity. With the increase in κ the centre of the primary vortex moves towards the top right of the cavity [Fig. 5.2 and Fig 5.5 (bottom)]. Also, the strength of the flow is reduced as seen from the value of $|\psi_{max}|$ shown in Table 5.2. The increasingly asymmetric behaviour of the temperature and concentration field shifts causes greater changes in the stream-line pattern in the upper part of the annulus. As can be seen from Fig. 5.5 (top), at $\kappa = 1$, the thermal boundary layers exist at the top right and bottom left regions of the annulus. With the increase in κ they become more prominent on the hot (inner) wall and less on the cold (outer) wall. Also from the isoconcentrates [Fig. 5.5 (centre)], it is seen that concentration gradients near the hot wall increase while the reverse happens at the cold wall. Temperature variation along the horizontal centreline is found to be almost linear at the core of the annulus for small κ and the curvature increases with κ [Fig. 5.6 (a)]. At the core, the concentration remains largely constant and decreases sharply to the value of -0.5, as κ increases. The high concentration gradients near the top and the hot walls [Fig. 5.5 (middle)] indicate high mass transfer, and high temperature gradients near the hot wall [Fig. 5.5 (top)] indicate high heat

Table 5.2: ψ_{max} *and its position for different radius ratios.*

κ	ψ_{max}	Primary vortex centre
1	301.482	$(0.5000, 0.5062)$
2	3.936	$(0.5315, 0.4844)$
5	1.509	(0.5515, 0.5875)
10	0.940	$(0.5440, 0.6594)$
20	0.6659	$(0.6110, 0.6719)$
50	0.4778	$(0.5940, 0.7250)$

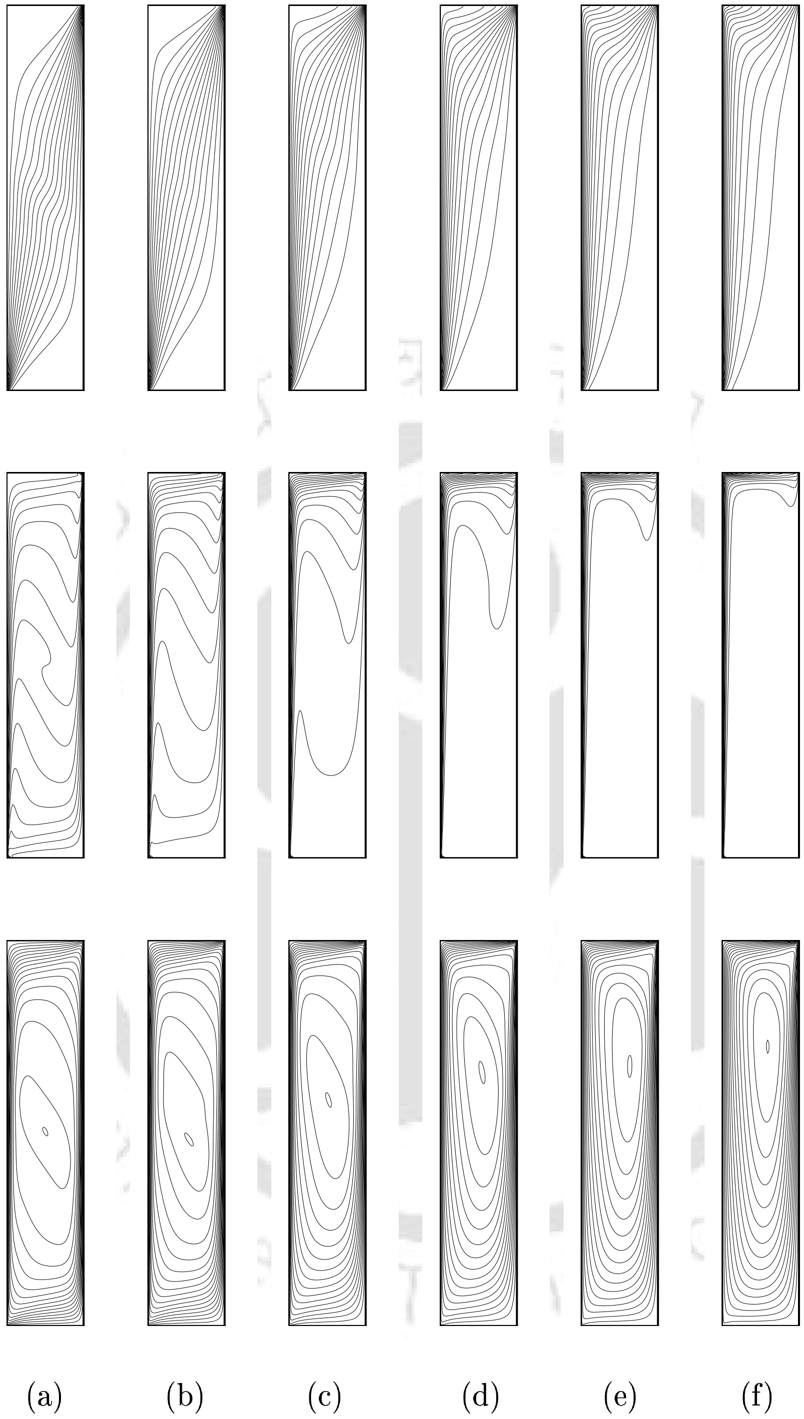

Figure 5.5: *Temperature (top), concentration (centre) and stream-function (bottom) contours for* $A = 5$, $Le = 10$, $Ra = 500$, $N = 5$ *and various values of* $\kappa = 1$, *2, 5, 10, 20 and 50 (from left to right in that order).*

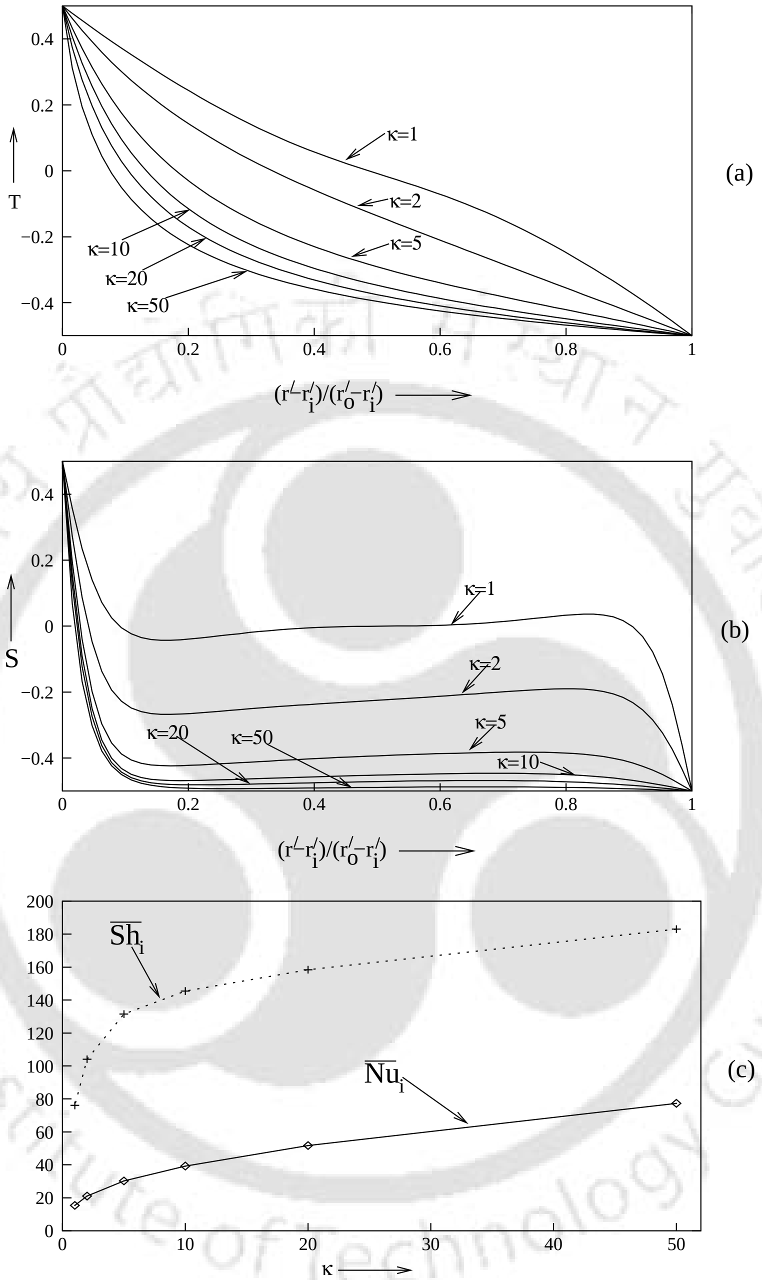

Figure 5.6: *Variations of (a) temperature and (b) concentration along the horizontal centreline and (c) average Nusselt and Sherwood numbers with respect to radius ratio* κ *for* $A = 5$, $Le = 10$, $Ra = 500$ *and* $N = 5$.

transfer in those regions and these effects increase with κ. This is confirmed by the increasing values of $\overline{Nu_i}$ and $\overline{Sh_i}$ [Fig. 5.6 (c)]. It may be mentioned that in the earlier studies, the simulations were confined only up to $\kappa = 10$ [10, 44].

5.4.4 Influence of Lewis Number

Here the parameters other than Le, viz., N, Ra, κ and A have been kept constant at 1, 500, 5 and 5 respectively. When $Le = 1$, the thermal diffusion equals the solutal diffusion and the isotherms and isoconcentrates are identical [Fig. 5.7 (a)]. With increase in Le, concentration boundary layers become sharper [Fig. 5.7 (centre)] whereas there is little change in the isotherm patterns [Fig. 5.7 (top)]. These facts are also evidenced by the centreline temperature and concentration distributions [Figs. 5.8 (a) and (b)] where for $Le \geq 5$, the temperature distribution is almost identical whereas the concentration boundary layers are seen thinning with increasing Le, particularly on the hot wall. At high Le's, as the mass diffusivity is much lower than the thermal diffusivity, the horizontal intrusion layers of concentration at the top and the bottom are considerably sharper than their thermal counterpart. As a result of this, the core of the concentration field at higher Le's is in a state of almost uniform concentration [Fig. 5.7 (b)-(f)]. Also, with increase in Le, there is a shift of the vortex centre toward the cold wall and hydrodynamic boundary layers thin down on the cold wall and thicken at the hot wall. The maximum Lewis number in the present study (viz., 500) is much greater than what was considered by the earlier investigations for this aspect ratio [2, 10, 44]. From Fig. 5.8 (c) it is seen that up to about $Le = 100$, $\overline{Sh_i}$ shows an increasing trend and a decreasing trend thereafter. Same figure shows that up to about $Le = 50$, $\overline{Nu_i}$ shows a decreasing trend and remains almost constant thereafter.

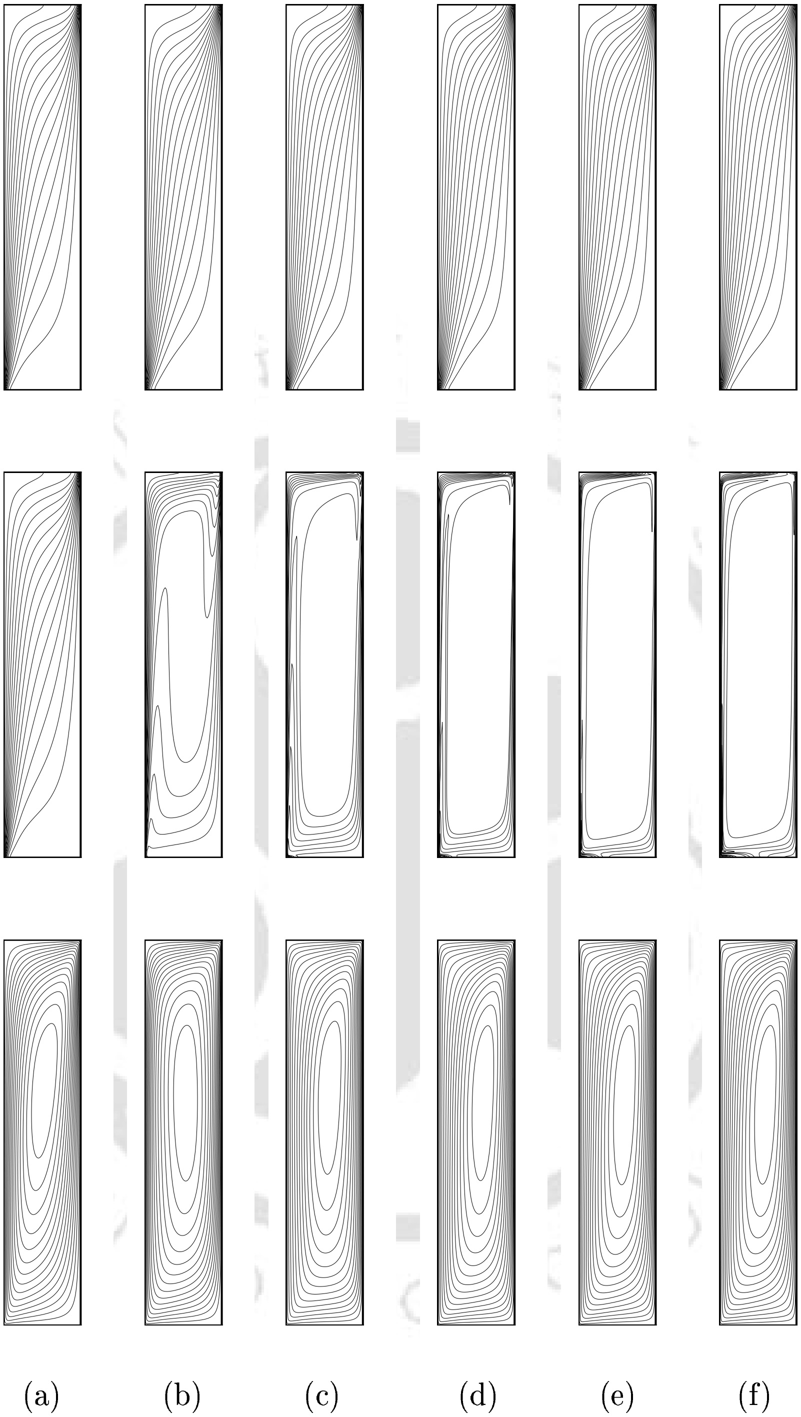

Figure 5.7: *Temperature (top), concentration (centre) and stream-function (bottom) contours for* $A = 5$, $\kappa = 2$, $Ra = 500$, $N = 1$ *and various values of* $Le = 1$, *10, 50, 100, 200 and 500 (from left to right in that order).*

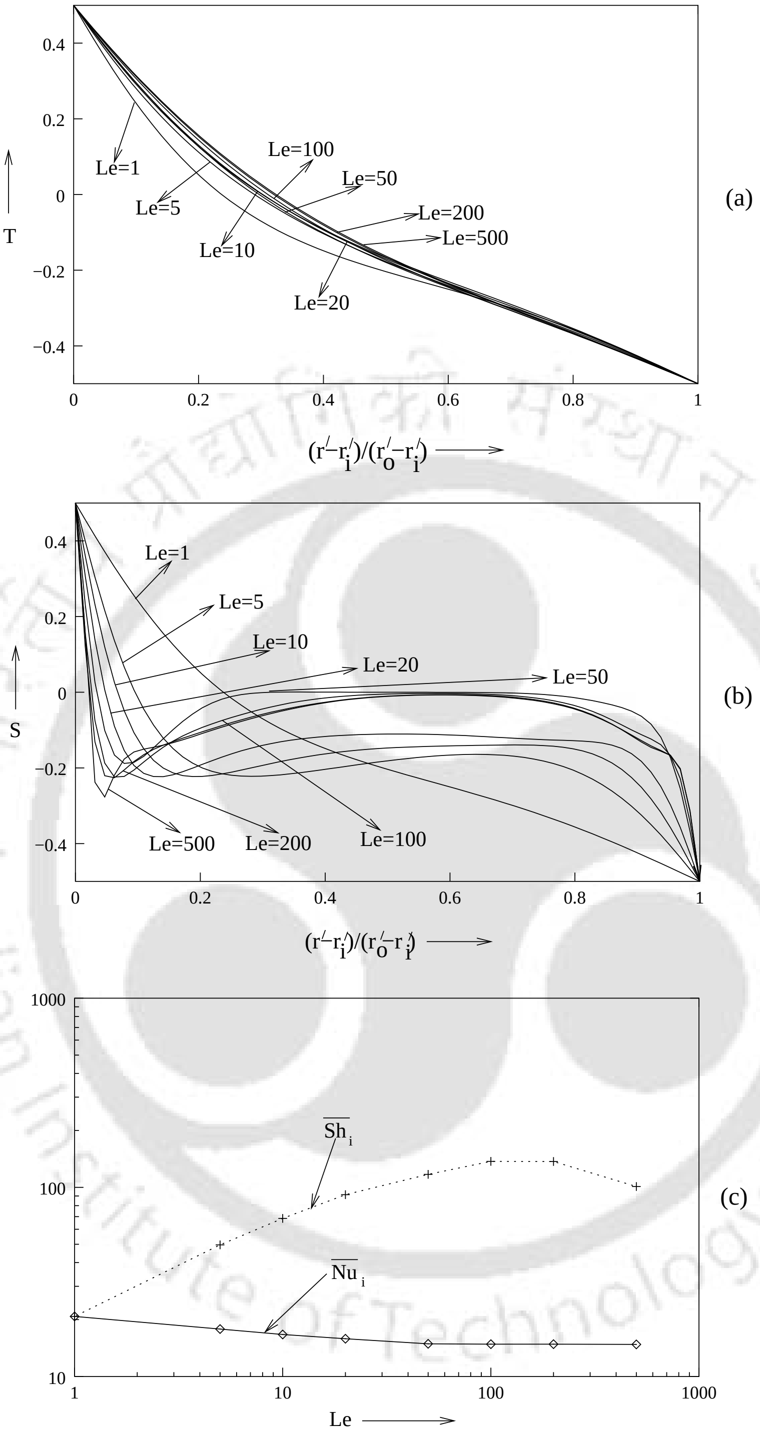

Figure 5.8: *Variations of (a) temperature and (b) concentration along the horizontal centreline and (c) average Nusselt and Sherwood numbers with respect to Lewis number Le for* $A = 5$, $\kappa = 2$, $Ra = 500$ *and* $N = 1$.

5.4.5 Influence of Buoyancy Ratio

Results are presented here for a wide range of Buoyancy ratios, viz., $-50 \leq N \leq 50$ with κ, Le, Ra and A fixed at 2, 10, 500 and 5 respectively. As a result of the thermal and solutal boundary conditions assumed here, the direction of the thermal flow is clockwise, whereas the direction of the solutal flow depends upon the sign of the concentration coefficient β_s, so that for $N > 0$ it is clockwise and for $N < 0$ it is anticlockwise. Though the range of buoyancy ratios explored here is also claimed to have been investigated in ref. [10], no qualitative or quantitative results are presented for $|N| = 50$ in that study. For $N \geq 0$, Figs. 5.9 (f)-(h) represent a selection of the simulated double-diffusive flows under the influence of mutually aiding effects of both the temperature and solute gradients. When $N << 1$, the buoyancy forces that drives the fluid motion are mainly due to the gradients in temperature; for $N = 0$, effects of concentration does not exist [Fig. 5.9 (e)] and the resulting flow pattern is that of pure heat transfer. That for $N > 0$, the mass species and thermal buoyancy forces augment each other, is also seen from Table 5.3 through the maximum and minimum values of ψ. Development of boundary layers is also seen with increase in N. For larger values of N, a large portion of the core of the annulus is seen to be stagnant [Fig. 5.9 (h)] because of the blocking effect of the combined effects of vertical concentration and temperature gradients.

The typical features of opposing double-diffusive flow can now be seen from Figs 5.9 (a)-(d). On lowering the buoyancy ratio to -2, one solute-driven rotating counterclockwise cell in the core region and two clockwise thermal-solute-driven cells develop on the top and bottom the annulus. When N is further decreased to -5, the lower clockwise cell is annihilated and with further decrease in N, only the counterclockwise cell remains with development of boundary layers which become prominent at $N = -50$. The effects of multiple cell formation at $N = -2$ are seen to modify the pattern of isotherm and isoconcentrates. With decreasing N, the isotherm pattern changes from vertical to diagonal. The vertical pattern at $N = -2$ indicates that the side-to-side heat transfer process is almost ruled by pure diffusion; at $N = -50$,

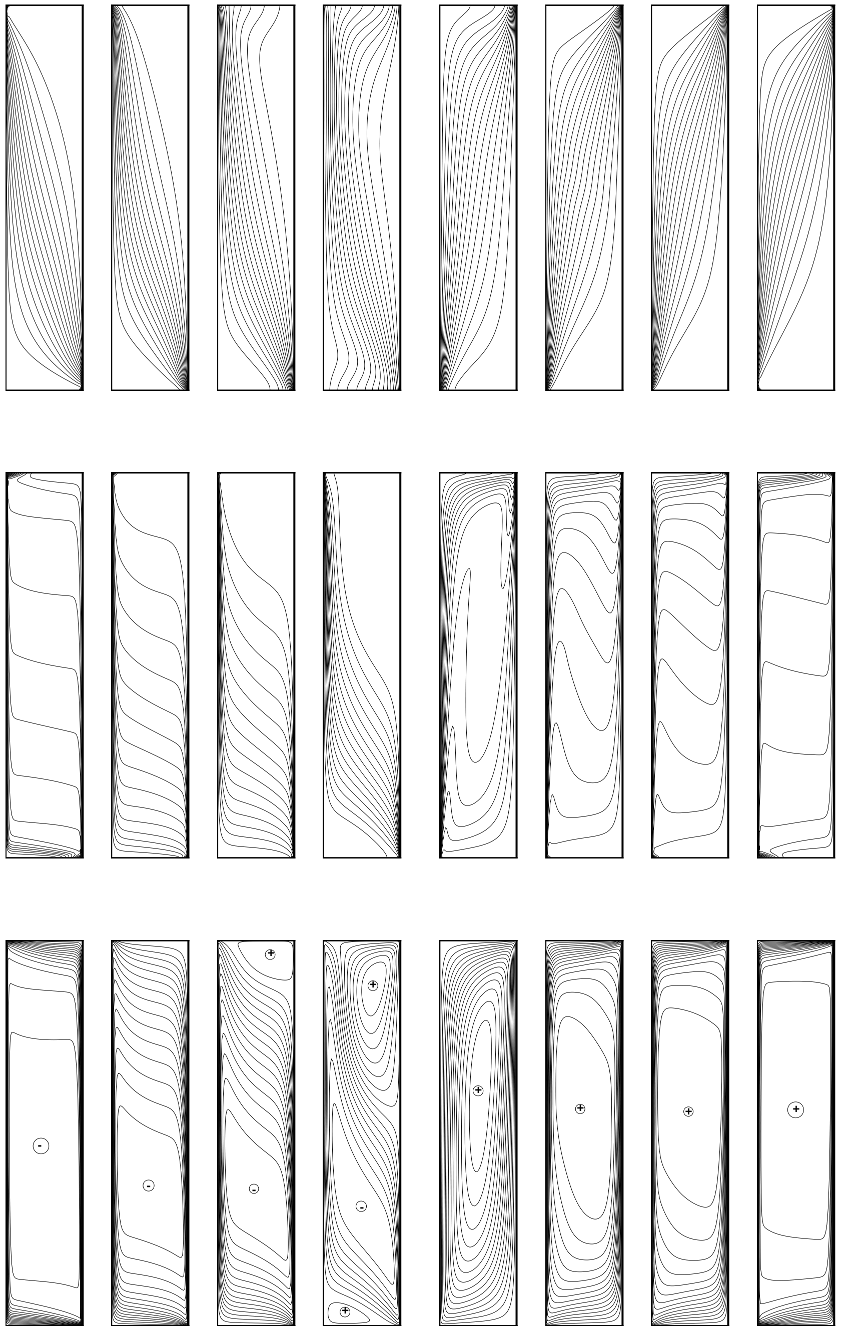

(a) (b) (c) (d) (e) (f) (g) (h)

Figure 5.9: *Temperature (top), concentration (centre) and stream-function (bottom) contours for $A = 5$, $Le = 10$, $Ra = 500$, $\kappa = 2$ and various values of N =-50, -10, -5, -2,, 0, 5, 10 and 50 (from left to right in that order).*

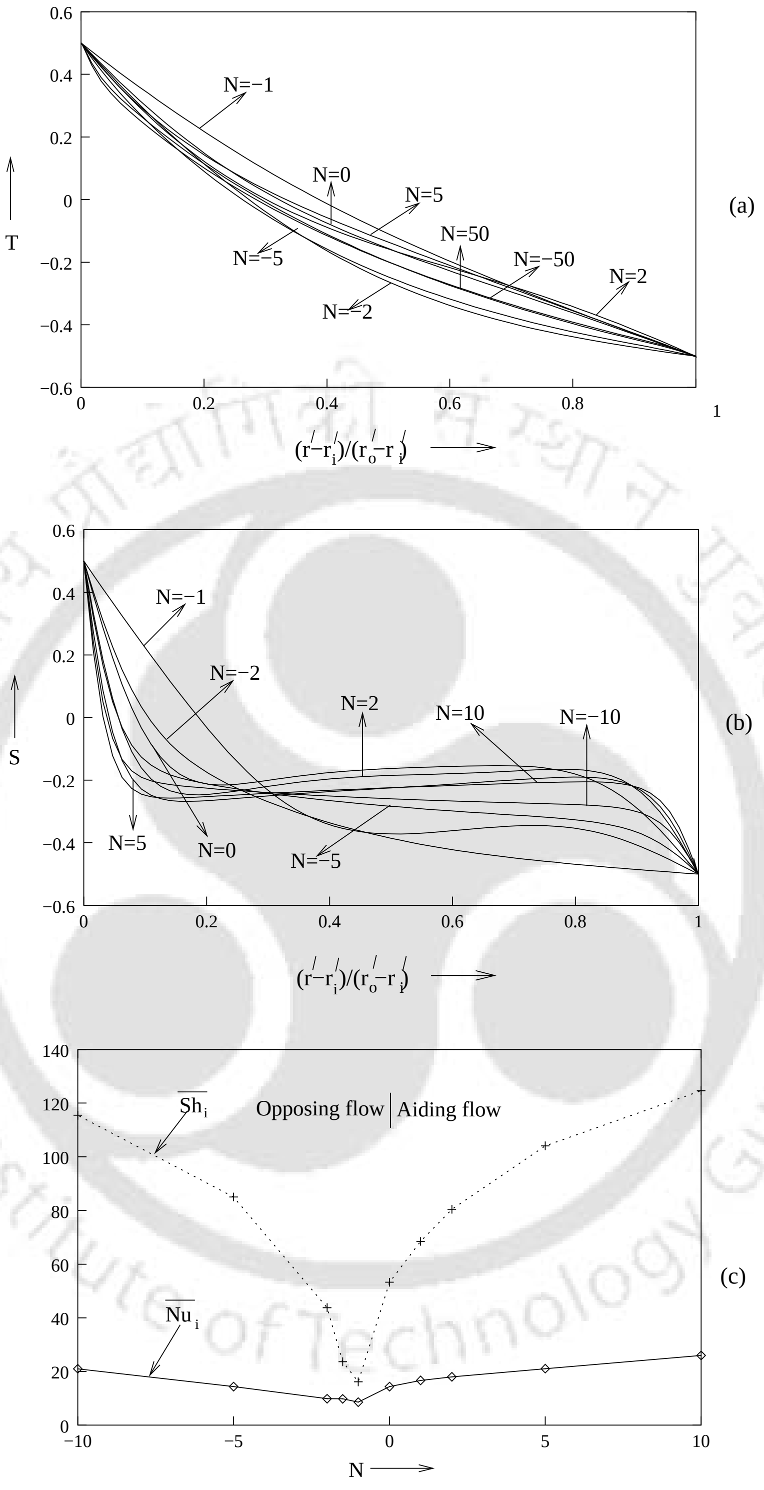

Figure 5.10: *Variations of (a) temperature and (b) concentration along the horizontal centreline and (c) average Nusselt and Sherwood numbers with respect to buoyancy ratio N for $A = 5$, $Le = 10$, $Ra = 500$ and $\kappa = 2$.*

Table 5.3: *Maximum and minimum values of ψ for different buoyancy ratios.*

N	ψ_{max}	ψ_{min}
-50	0	-13.5306
-10	0	-4.1492
-5	0.1948	-2.6408
-2	1.0462	-1.2397
-1.5	1.9720	-0.0412
-1	1.6016	-0.1661
-0.5	3.1688	0
0	3.1596	0
1	3.4990	0
2	3.6331	0
5	3.9362	0
10	5.0713	0
50	14.2914	0

the thermal field at the upper and lower parts of the annulus is now fairly homogeneous, whereas in the core, it is observed to be diagonal. The same can be said about the isoconcentration contours for $N = -2$. With further decrease in N, the flow becomes more stratified.

From the temperature distribution along the horizontal centreline [Fig. 5.10 (a)], it is seen that as $|N|$ increases the curves corresponding to the respective positive and negative values come increasingly close to each other and for $|N| = 50$, they almost merge into one. The temperature profile looks almost like that of a pure conduction regime. This is because of the relatively stagnant core for this kind of flow. For high $|N|$, the horizontal centreline concentration profile seems to remain constant within the core region [Fig. 5.10 (b)]. This is because of weaker mass species diffusivity ($Le = 10$), in which the mass species gradients can not penetrate the stagnant core as far as the thermal gradients.

The effect of buoyancy ratio on $\overline{Nu_i}$ and $\overline{Sh_i}$ can be observed from Fig 5.10 (c). They tend to remain minimum in the transitional range of N, where the flow reversal is about to take place. Expectedly, $\overline{Nu_i}$ for a certain $|N|$ is less when the flow is opposing ($N < 0$) than when it is aiding ($N > 0$). This is also true for $\overline{Sh_i}$; however, the relative difference for corresponding aiding and opposing buoyancy ratios is lower. This difference is attributed to the fact that the opposing flow has a lower flow rate adjacent to the enclosure walls than does the corresponding aiding flow.

Many of the trends observed for this configuration are keeping with the observation of earlier studies. For example, flow patterns in the sub-range $-5 \leq N \leq 5$ shown in Figs. 5.9 (c)-(f) are very close to those presented in ref. [10]. Again, the trends for $\overline{Nu_i}$ and $\overline{Sh_i}$ distribution shown in Fig. 5.10 (c) resembles the ones presented for rectangular annulus in [60].

5.4.6 Influence of Thermal Rayleigh Numbers

Computations are carried out for the range of Ra from 0 to 5000, keeping the other parameters A, κ, Le and N fixed at 5, 2, 10 and 5 respectively. The strength of the general convective movement increases with increasing Ra. This can be seen from the $\overline{Nu_i}$ and $\overline{Sh_i}$ distribution in Fig. 5.12 (c), indicating increased heat and solute transfer rates at the inner wall and also from the computed ψ_{max} values of Table 5.4, which indicates increased flow rate. With

Table 5.4: ψ_{max} *values for different* Ra.

Ra	ψ_{max}
0	0
10	0.3733
50	1.1771
100	1.7227
200	2.3909
500	3.9362
1000	6.1550
5000	20.5441

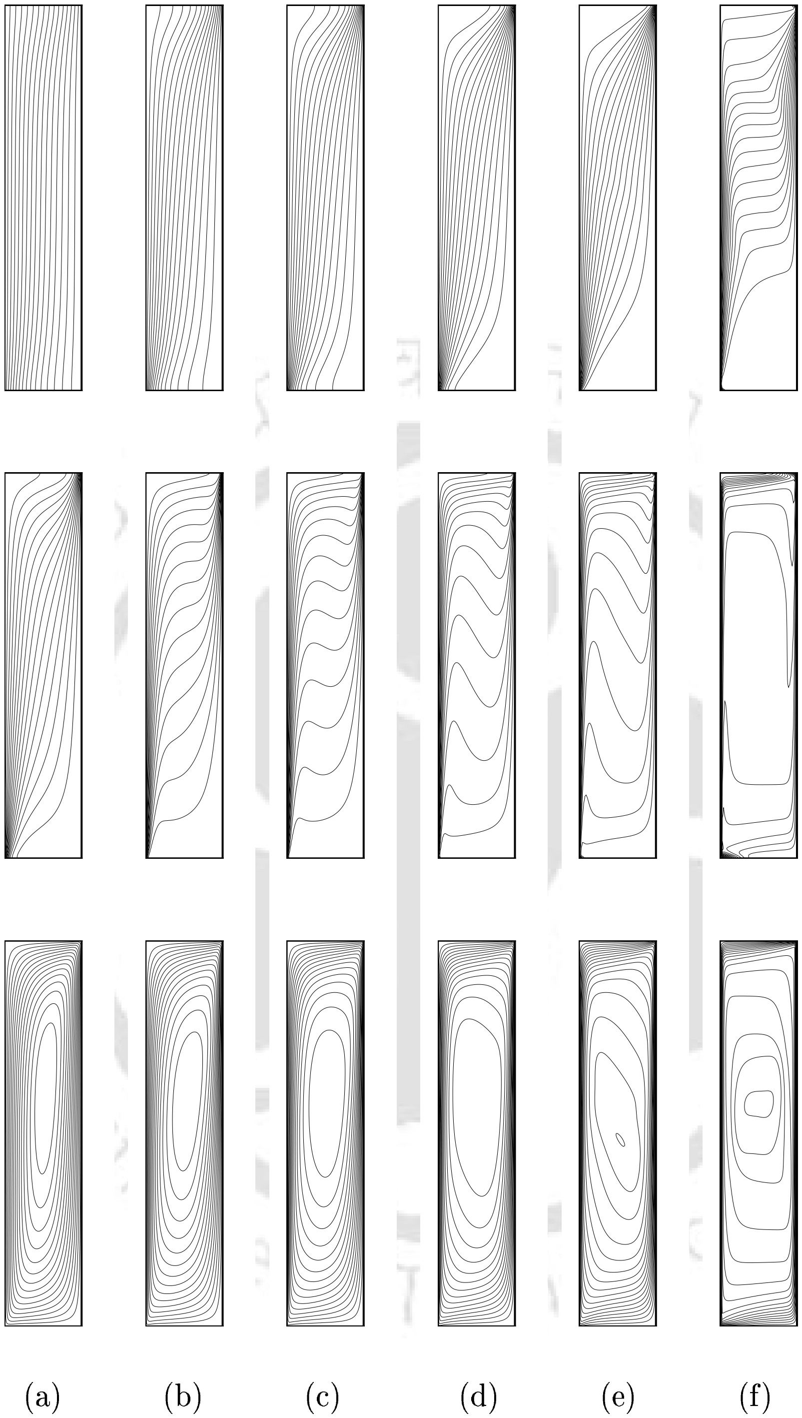

Figure 5.11: *Temperature (top), concentration (centre) and stream-function (bottom) contours for* $A = 5$, $Le = 10$, $\kappa = 2$, $N = 5$ *and different thermal Rayleigh numbers* $Ra = 10$, *50, 100, 200, 500 and 5000 (from left to right in that order).*

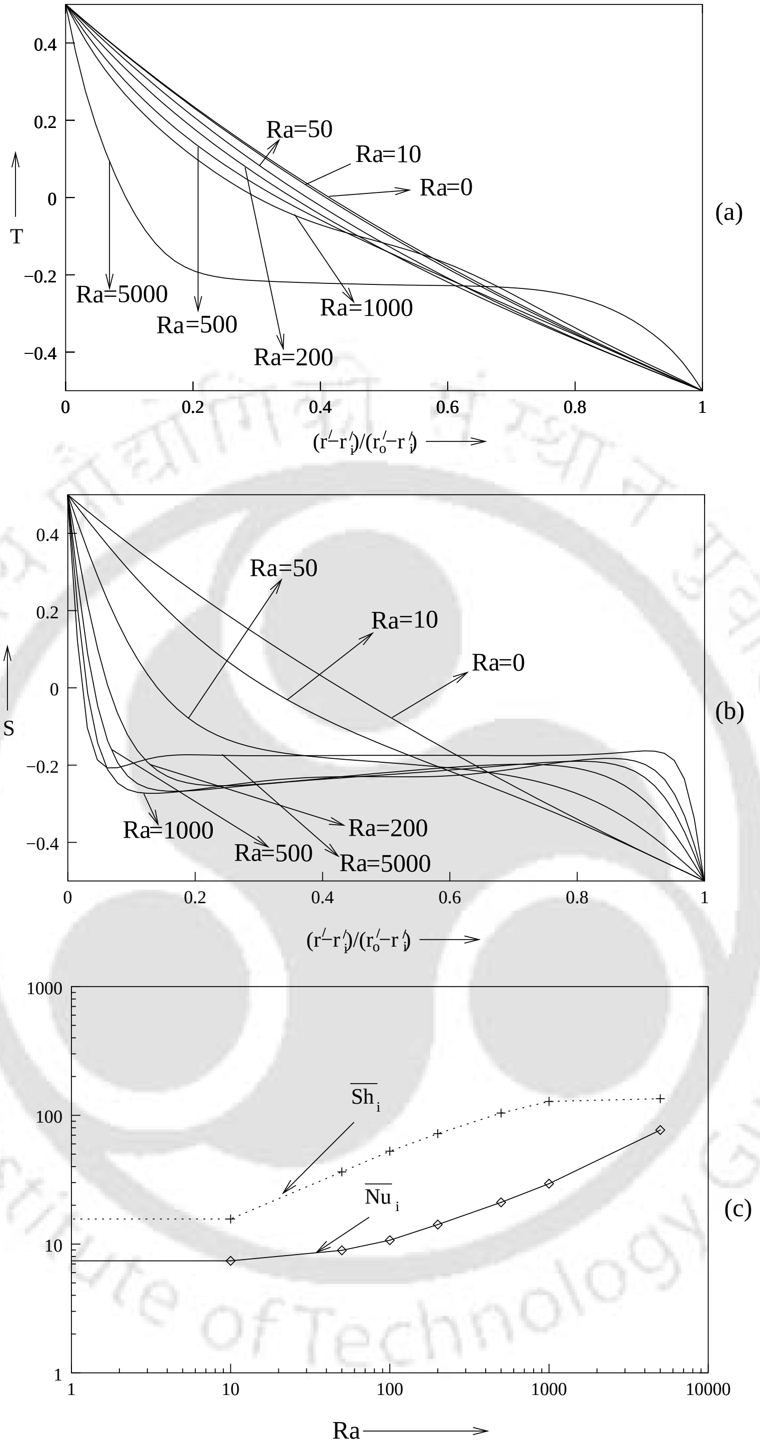

Figure 5.12: *Variations of (a) temperature and (b) concentration along the horizontal centreline and (c) average Nusselt and Sherwood numbers w. r. t. thermal Rayleigh number Ra for* $A = 5$, $\kappa = 2$, $Le = 10$ *and* $N = 5$.

increase in Ra, development of hydrodynamic boundary layers becomes increasingly obvious [Fig. 5.11 (bottom)]. The concentration boundary layers become much sharper in the inner wall compared to the outer [Figs. 5.11 (centre) and 5.12 (b)]. As Ra increses the isotherm pattern undergoes an interesting change [Fig. 5.11 (top)]. At low Ra's, the isotherms are almost vertical [Figs. 5.11 (a)-(c), top] indicating conduction dominated heat transfer. This fact is also observed from Fig. 5.12 (a). As Ra increses the isotherms become more and more diagonal [Figs. 5.11 (d) and (e), top] and at a high $Ra = 5000$, they become almost horizontal in the central portion of the annulus. As expected, with increase in Ra, $\overline{Nu}$ at the inner wall steadily increases, but $\overline{Sh}$ generally approach a constant value. It may be mentioned that at high Rayleigh numbers such as $Ra = 5000$, the computational complexities increase drastically and timestep used must necessarily be very small. This complexity could be one of the reasons why no results for such high Ra has been seen for this configuration so far.

5.5 Conclusion

A numerical investigation has been carried out on the phenomenon of thermosolutal convection in a concentric vertical annulus filled with a porous medium through the $(9, 9)$ transient HOC scheme proposed in Chapter 4. The higher-order accuracy of the scheme coupled with compactness of the computational stencils affords efficient computations for a wide range of the parameters governing the flow on relatively coarser grids. The influences of the aspect ratio A, the radius ratio κ, the buoyancy ratio N, the Lewis number Le and thermal Rayleigh number Ra on the flow have been investigated. As the number and range of parameters are quite large, exact comparisons with earlier work is not always possible. Wherever results of earlier investigations are available, comparisons are made and close resemblance is observed. For some difficult cases, for example, for large $|N|$ and Ra, computations for the configuration have been carried out probably for the first time, highlighting the efficiency and robustness of the present algorithm. As the algorithm and code has been carefully validated through a comparison excercise, and considering the high order of accuracy of the scheme, the new results produced for difficult cases are expected to be highly reliable. These results are quantified in several tables which may be used by later investigators to advantage. Based on the study, many observations can be made by varying one of the parameters κ, A, N, Ra or Le while keeping the others constant. They are summarized below:

As radius ratio κ increases $\overline{Nu}$ and $\overline{Sh}$ increse indicating increased heat and mass transfer. At $\kappa = 1$, there is a centrosymmetry of temperature, concentration and flow, which is lost as κ increases.

As aspect ratio increases from $A = 1$, mass transfer indicated by $\overline{Sh}$ at the inner wall increases gradually and at higher values like $A = 5$ and beyond, it remains almost constant. Heat transfer represented by $\overline{Nu}$ exhibits almost a similar behaviour.

Lewis number Le is mainly seen to have an influence on the concentration field. At lower values there is variation of concentration throughout the cavity; but as Le increases, the gradients almost completely vanish from the core of the annulus.

Effect of buoyancy ratio N on the behaviour of the solution has been studied in some details. The flow pattern undergoes some interesting change as the buoyancy ratio changes sign. When N is positive, thermal and solutal gradients tend to drive the flow in the same direction producing a clockwise flow pattern. At $N = 0$ the flow is still clockwise, but completely thermally driven. As N decreases below zero, solutal gradients start opposing thermally driven flow first giving rise to an interplay of counter rotating cells and finally at still lower values of N (or higher values of $|N|$) the clockwise rotating cells due to thermal gradients are completely annihilated and a single anticlockwise flow cell is obtained. Hot wall $\overline{Nu}$ and $\overline{Sh}$ also exhibit interesting behaviour with the values being minimum for N close to -1, indicating that opposing effects of thermal and solutal gradients, being comparable in magnitude, impedes heat and mass transfer greatly. Any increase of $|N|$ expectedly results in increased activity giving rise to gradual increase of $\overline{Nu}$ and $\overline{Sh}$.

Also studied are the effects of Ra for an aiding flow. Expectedly, increase in Ra aids heat transfer as seen from the steady rise of $\overline{Nu}$ with Ra at the inner wall. Mass transfer, however, appears to stagnate beyond a certain Ra as indicated by an almost constant value of $\overline{Sh}$.

Chapter 6

HOC SCHEME ON NONUNIFORM GRIDS WITHOUT TRANSFORMATION

6.1 Introduction

Finite difference method is frequently used in computational fluid dynamics. The method essentially consists in setting up a grid in the problem domain, discretizing the governing equations with respect to the grid and solving them numerically. The common practice is to use a uniform grid, though it may not be the most appropriate one for efficient computation. Accurate resolution of the solution requires that grid points are clustered in the regions of large gradients while economy demands that they are spread out in the regions of small gradients [5, 6, 30]. Hence a nonuniform grid is indicated for many flow configurations. The popular approach is to map the physical space with a nonuniform grid onto a computational space with uniform grid where a transformed set of equations is first solved before mapping this solution back onto the physical space. Disadvantages of such an approach are many. There is a substantial increase in the number of terms to be discretized in the transformed governing equation giving rise to added computation. Many a time the transformation of the equations results in the appearance of cross-derivative terms which increases the computational complexity in many solution algorithms [30]. Moreover if the transformation is not explicitly known, it may have to be generated by numerical solution of some differential equation and this results in additional error. Overall, the solution procedure becomes complicated, expensive and sometimes error-prone.

The HOC finite difference schemes for the computation of incompressible viscous flows [42, 46, 67, 71, 78] are gradually gaining popularity because of their high accuracy and advantages associated with compact difference stencils. However such computations have so far been carried out only on uniform grids. In a departure from this practice, Spotz and Carey [69] recently applied a fourth order accurate HOC scheme on a nonuniform grid to linear convection-diffusion equations without source term. They use the conventional transformation technique which inevitably brings in the complications of having to deal with some new cross-derivative terms in the transformed partial differential equations (PDE) in addition to the increase in terms of arithmetic operations. Also, the advantage of setting the diffusive coefficients appearing in the PDEs in the physical space to unity is lost because they no longer remain the same in the transformed space. An additional constraint is that the transformation has to be carried out in such a way as to keep the grid aspect ratio unity in the computational space. In the present work, we propose an HOC scheme on rectangular nonuniform grids for the steady 2D convection-diffusion equation with variable coefficients without any transformation [1]. It is based on the Taylor series expansion of a continuous function at a particular point for two different step lengths and approximation of the derivatives appearing in the 2D convection-diffusion equation on a nonuniform stencil. As before, the original PDE is then used again to replace the derivative terms appearing in the finite difference approximations, resulting in a higher order scheme on a compact stencil of nine points. We have seen that the grid aspect ratio in the earlier HOC schemes has to be necessarily unity. Even in the case

---

[1] Review of this work, after revision, is in progress in *J. Comp. Physics.*

where nonuniform grid has been used with transformation [69], this constraint remain in the computational space. The present scheme not only frees HOC schemes from such a constraint, but also makes it possible to use whatever nonuniform pattern of spacing one chooses in either direction. The order of accuracy of the scheme lies between three and four based on the pattern of grid spacing. Apart from avoiding the complexities associated with transformation techniques, this method affords a solution procedure that marries the virtues of a clustered grid to the efficiency of an HOC scheme. To validate the algorithm, the method has first been tested on two problems governed by linear PDEs for which analytical solutions exist. The power of the algorithm is better realized when applied to two fluid flow problems governed by the 2D incompressible N-S equations at high Re's in that it captures the physics of the flow accurately with relatively smaller number of grid points – a result of grid clustering – with complexities not higher than that associated with an HOC scheme on a uniform grid. The scheme handles both Dirichlet and Neumann boundary conditions with ease and has the potential for extension to transient flow problems and curvilinear co-ordinates as well.

6.2 Basic Formulations, Discretization and Numerical Procedure

Consider a rectangular domain $a_1 \le x \le a_2$, $b_1 \le y \le b_2$. We divide the interval $[a_1, a_2]$ into sub-intervals, not necessarily of equal length, by the points $a_1{=}x_0$, x_1, x_2, ..., x_{m-1}, $x_m{=}a_2$ and similarly $[b_1, b_2]$ by the points $b_1{=}y_0$, y_1, y_2, ..., y_{n-1}, $y_n{=}b_2$. In the x-direction, the forward and backward step lengths are given by $x_f = x_{i+1} - x_i$ and $x_b = x_i - x_{i-1}$ respectively, and similarly, in the y-direction, we have $y_f = y_{j+1} - y_j$ and $y_b = y_j - y_{j-1}$, $\quad 1 \le i \le m-1, \quad 1 \le j \le n-1$. For a function $\Phi(x, y)$ assumed smooth in the given domain, a Taylor series expansion at point $(i+1, j)$, (Figure 6.1) gives

$$\Phi_{i+1,j} = \Phi_{i,j} + x_f \frac{\partial \Phi}{\partial x} + \frac{x_f^2}{2!}\frac{\partial^2 \Phi}{\partial x^2}\bigg|_{ij} + \frac{x_f^3}{3!}\frac{\partial^3 \Phi}{\partial x^3}\bigg|_{ij} + \frac{x_f^4}{4!}\frac{\partial^4 \Phi}{\partial x^4}\bigg|_{ij} + O(x_f^5) \quad (6.1)$$

Similarly at $(i-1,j)$

$$\Phi_{i-1,j} = \Phi_{i,j} - x_b \frac{\partial \Phi}{\partial x} + \frac{x_b^2}{2!}\frac{\partial^2 \Phi}{\partial x^2}\bigg|_{ij} - \frac{x_b^3}{3!}\frac{\partial^3 \Phi}{\partial x^3}\bigg|_{ij} + \frac{x_b^4}{4!}\frac{\partial^4 \Phi}{\partial x^4}\bigg|_{ij} + O(x_b^5) \quad (6.2)$$

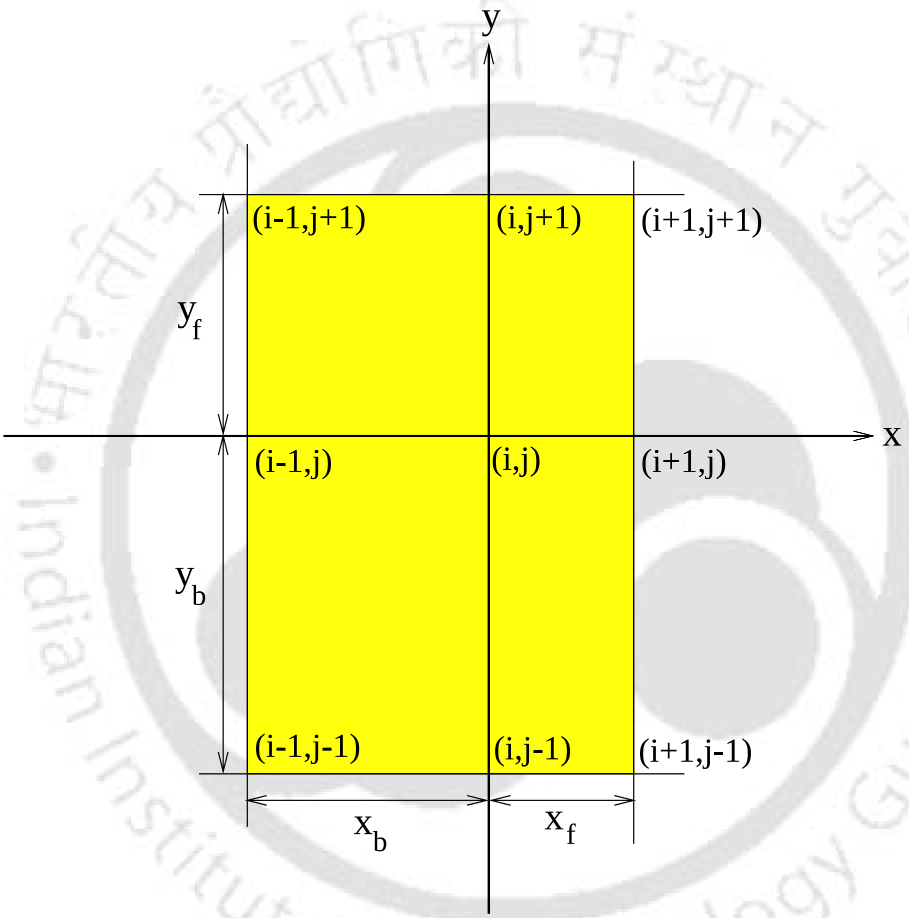

Figure 6.1: *Non uniform HOC stencil.*

From equations (6.1) and (6.2), we have

$$\begin{aligned}\frac{\partial \Phi}{\partial x}\bigg|_{ij} &= \frac{\Phi_{i+1,j} - \Phi_{i-1,j}}{x_f + x_b} - \frac{1}{2}(x_f - x_b)\,\frac{\partial^2 \Phi}{\partial x^2}\bigg|_{ij} - \frac{1}{6}(x_f^2 + x_b^2 - x_f x_b)\,\frac{\partial^3 \Phi}{\partial x^3}\bigg|_{ij} \\ &+ O\left((x_f - x_b)(x_f^2 + x_b^2)\right) \qquad (6.3)\end{aligned}$$

and

$$\begin{aligned}\left.\frac{\partial^2\Phi}{\partial x^2}\right|_{ij} &= \frac{2}{(x_f+x_b)}\left[\frac{\Phi_{i+1,j}}{x_f}+\frac{\Phi_{i-1,j}}{x_b}-\left(\frac{1}{x_f}+\frac{1}{x_b}\right)\Phi_{i,j}\right]-\frac{1}{3}(x_f-x_b)\left.\frac{\partial^3\Phi}{\partial x^3}\right|_{ij}\\ &- \frac{1}{12}(x_f^2+x_b^2-x_fx_b)\left.\frac{\partial^4\Phi}{\partial x^4}\right|_{ij}+O\left((x_f-x_b)(x_f^2+x_b^2)\right) \qquad (6.4)\end{aligned}$$

In the x-direction, the first and second order central difference (CD) operators are defined by,

$$\delta_x\Phi_{ij}=\frac{\Phi_{i+1,j}-\Phi_{i-1,j}}{x_f+x_b}$$

and

$$\delta_x^2\Phi_{ij}=\frac{2}{(x_f+x_b)}\left[\frac{\Phi_{i+1,j}}{x_f}+\frac{\Phi_{i-1,j}}{x_b}-\left(\frac{1}{x_f}+\frac{1}{x_b}\right)\Phi_{i,j}\right].$$

With these notations, (6.4) becomes

$$\begin{aligned}\left.\frac{\partial^2\Phi}{\partial x^2}\right|_{ij} &= \delta_x^2\Phi_{ij}-\frac{1}{3}(x_f-x_b)\left.\frac{\partial^3\Phi}{\partial x^3}\right|_{ij}\\ &- \frac{1}{12}(x_f^2+x_b^2-x_fx_b)\left.\frac{\partial^4\Phi}{\partial x^4}\right|_{ij}+O\left((x_f-x_b)(x_f^2+x_b^2)\right) \qquad (6.5)\end{aligned}$$

From equations (6.3) and (6.5), the first derivative may be approximated as

$$\begin{aligned}\left.\frac{\partial\Phi}{\partial x}\right|_{ij} &= \delta_x\Phi_{ij}-\frac{1}{2}(x_f-x_b)\delta_x^2\Phi_{ij}-\frac{x_fx_b}{6}\left.\frac{\partial^3\Phi}{\partial x^3}\right|_{ij}\\ &+ O\left((x_f-x_b)(x_f^2+x_b^2)\right) \qquad (6.6)\end{aligned}$$

Similar expressions can be derived for the y-derivatives.

Now, we proceed to derive the HOC scheme for the 2D convection-diffusion equation (2.3) on nonuniform grids. In view of equations (6.5) and (6.6), it may be approximated as

$$\left[-\delta_x^2-\delta_y^2+c\left\{\delta_x-0.5(x_f-x_b)\delta_x^2\right\}+d\left\{\delta_y-0.5(y_f-y_b)\delta_y^2\right\}\right]\phi_{ij}+\tau_{ij}=f_{ij} \qquad (6.7)$$

where τ_{ij} is the truncation error given by

$$\begin{aligned}\tau_{ij} &= H_1\frac{\partial^3\phi}{\partial x^3}+K_1\frac{\partial^3\phi}{\partial y^3}+H_2\frac{\partial^4\phi}{\partial x^4}+K_2\frac{\partial^4\phi}{\partial y^4}\\ &+ O\left((x_f-x_b)(x_f^2+x_b^2)+(y_f-y_b)(y_f^2+y_b^2)\right)\end{aligned} \tag{6.8}$$

with

$$H_1=\frac{1}{6}\left\{2(x_f-x_b)-cx_fx_b\right\},\quad H_2=\frac{1}{12}\left(x_f^2+x_b^2-x_fx_b\right)$$

and

$$K_1=\frac{1}{6}\left\{2(y_f-y_b)-dy_fy_b\right\},\quad K_2=\frac{1}{12}\left(y_f^2+y_b^2-y_fy_b\right)$$

6.2.1 Constant Convective Coefficients

If the convective coefficients c and d are constants, using the original equation (2.3) to substitute for the third and fourth order derivatives, (6.8) can be written as

$$\begin{aligned}\tau_{ij} &= (H_1+H_2c)\,c\frac{\partial^2\phi}{\partial x^2}+(K_1+K_2d)\,d\frac{\partial^2\phi}{\partial y^2}\\ &+ \left\{(H_1+H_2c)d+(K_1+K_2d)c\right\}\frac{\partial^2\phi}{\partial x\partial y}\\ &- (H_1+H_2c-K_2c)\,\frac{\partial^3\phi}{\partial x\partial y^2}-(K_1+K_2d-H_2d)\,\frac{\partial^3\phi}{\partial x^2\partial y}\\ &- (H_2+K_2)\,\frac{\partial^4\phi}{\partial x^2\partial y^2}\\ &- \left\{(H_1+H_2c)\frac{\partial}{\partial x}+(K_1+K_2d)\frac{\partial}{\partial y}+H_2\frac{\partial^2}{\partial x^2}+K_2\frac{\partial^2}{\partial y^2}\right\}f\\ &+ O\left((x_f-x_b)(x_f^2+x_b^2)+(y_f-y_b)(y_f^2+y_b^2)\right)\end{aligned} \tag{6.9}$$

From equations (6.7) and (6.9), the HOC scheme in nonuniform grids for the equation (2.3) with constant convective coefficients can be written as

$$\left[-A_{ij}\delta_x^2-B_{ij}\delta_y^2+c\delta_x+d\delta_y+G_{ij}\delta_x\delta_y-H_{ij}\delta_x\delta_y^2-K_{ij}\delta_x^2\delta_y-L_{ij}\delta_x^2\delta_y^2\right]\phi_{ij}=F_{ij}, \tag{6.10}$$

where the coefficients $A_{ij}, B_{ij}, G_{ij}, H_{ij}, K_{ij}$ and L_{ij} are as follows:

$$A_{ij} = 1 + 0.5(x_f - x_b)c - (H_1 + H_2c)c, \tag{6.11}$$

$$B_{ij} = 1 + 0.5(y_f - y_b)d - (K_1 + K_2d)d, \tag{6.12}$$

$$G_{ij} = (H_1 + H_2c)d + (K_1 + K_2d)c, \tag{6.13}$$

$$H_{ij} = H_1 + H_2c - K_2c, \tag{6.14}$$

$$K_{ij} = K_1 + K_2d - H_2d, \tag{6.15}$$

$$L_{ij} = H_2 + K_2 \tag{6.16}$$

and

$$\begin{aligned} F_{ij} &= \Big[1 + (H_1 + H_2c)\delta_x + (K_1 + K_2d)\delta_y + \{H_2 - 0.5(x_f - x_b)(H_1 + H_2c)\}\,\delta_x^2 \\ &+ \{K_2 - 0.5(y_f - y_b)(K_1 + K_2d)\}\,\delta_y^2\Big]\, f_{ij} \end{aligned} \tag{6.17}$$

6.2.2 Variable Convective Coefficients

For variable convective coefficients the formulations are more complicated with the derivatives of c and d also coming into the picture. Using (2.3), as before, to substitute for the derivatives, (6.8) can be written as:

$$\begin{aligned} \tau_{ij} &= \left(H_1c + H_2c^2 + 2H_2\frac{\partial c}{\partial x}\right)\frac{\partial^2\phi}{\partial x^2} + \left(K_1d + K_2d^2 + 2K_2\frac{\partial d}{\partial y}\right)\frac{\partial^2\phi}{\partial y^2} \\ &+ \left\{(H_1 + H_2c)\frac{\partial c}{\partial x} + (K_1 + K_2d)\frac{\partial c}{\partial y} + H_2\frac{\partial^2 c}{\partial x^2} + K_2\frac{\partial^2 c}{\partial y^2}\right\}\frac{\partial\phi}{\partial x} \\ &+ \left\{(H_1 + H_2c)\frac{\partial d}{\partial x} + (K_1 + K_2d)\frac{\partial d}{\partial y} + H_2\frac{\partial^2 d}{\partial x^2} + K_2\frac{\partial^2 d}{\partial y^2}\right\}\frac{\partial\phi}{\partial y} \\ &+ \left\{(H_1 + H_2c)d + (K_1 + K_2d)c + 2H_2\frac{\partial d}{\partial x} + 2K_2\frac{\partial c}{\partial y}\right\}\frac{\partial^2\phi}{\partial x\partial y} \\ &- \{H_1 + H_2c - K_2c\}\,\frac{\partial^3\phi}{\partial x\partial y^2} - \{K_1 + K_2d - H_2d\}\,\frac{\partial^3\phi}{\partial x^2\partial y} \end{aligned}$$

$$
\begin{aligned}
&- \quad (H_2+K_2)\frac{\partial^4\phi}{\partial x^2\partial y^2}\\
&- \quad \left\{(H_1+H_2c)\frac{\partial}{\partial x}+(K_1+K_2d)\frac{\partial}{\partial y}+H_2\frac{\partial^2}{\partial x^2}+K_2\frac{\partial^2}{\partial y^2}\right\}f\\
&+ \quad O\left((x_f-x_b)(x_f^2+x_b^2)+(y_f-y_b)(y_f^2+y_b^2)\right) \qquad (6.18)
\end{aligned}
$$

From equations (6.7) and (6.18), we have the following HOC scheme on nonuniform grids for equation (2.3) with variable convective coefficients:

$$
\begin{aligned}
[\quad &- \quad A_{ij}\delta_x^2 - B_{ij}\delta_y^2 + C_{ij}\delta_x + D_{ij}\delta_y\\
&+ \quad G_{ij}\delta_x\delta_y - H_{ij}\delta_x\delta_y^2 - K_{ij}\delta_x^2\delta_y - L_{ij}\delta_x^2\delta_y^2]\,\phi_{ij} = F_{ij}, \qquad (6.19)
\end{aligned}
$$

where the coefficients $C_{ij}, D_{ij}, A_{ij}, B_{ij}$ and G_{ij} are given by

$$
\begin{aligned}
C_{ij} \quad &= \quad \left[1+(H_1+H_2c)\delta_x+(K_1+K_2d)\delta_y+\{H_2-0.5(x_f-x_b)(H_1+H_2c)\}\,\delta_x^2\right.\\
&+ \quad \left.\{K_2-0.5(y_f-y_b)(K_1+K_2d)\}\,\delta_y^2\right]c, \qquad (6.20)
\end{aligned}
$$

$$
\begin{aligned}
D_{ij} \quad &= \quad \left[1+(H_1+H_2c)\delta_x+(K_1+K_2d)\delta_y+\{H_2-0.5(x_f-x_b)(H_1+H_2c)\}\,\delta_x^2\right.\\
&+ \quad \left.\{K_2-0.5(y_f-y_b)(K_1+K_2d)\}\,\delta_y^2\right]d, \qquad (6.21)
\end{aligned}
$$

$$
A_{ij} = 1-\left[(H_1+H_2c)+2H_2\left\{\delta_x c-0.5(x_f-x_b)\delta_x^2 c\right\}\right]+0.5(x_f-x_b)C_{ij}, \qquad (6.22)
$$

$$
B_{ij} = 1-\left[(K_1+K_2d)+2K_2\left\{\delta_y d-0.5(y_f-y_b)\delta_y^2 d\right\}\right]+0.5(y_f-y_b)D_{ij}, \qquad (6.23)
$$

and

$$
\begin{aligned}
G_{ij} \quad &= \quad (H_1+H_2c)d+(K_1+K_2d)c+2H_2\delta_x d+2K_2\delta_y c\\
&- \quad \left\{H_2(x_f-x_b)\delta_x^2 d+K_2(y_f-y_b)\delta_y^2 c\right\} \qquad (6.24)
\end{aligned}
$$

The details of the FD operators appearing in equations (6.10) and (6.19) are given in the Appendix B. The discretized form of equations (6.10) and (6.19) can now be put in the form

$$
\sum_{k_1=-1}^{1}\sum_{k_2=-1}^{1}\eta_{i+k_1,j+k_2}\;\phi_{i+k_1,j+k_2} = \sum_{k_1=-1}^{1}\sum_{k_2=-1}^{1}\xi_{i+k_1,j+k_2}\;f_{i+k_1,j+k_2}, \qquad (6.25)
$$

where η, ξ's are functions of the convection coefficients c and d, their derivatives and the step lengths x_f, x_b, y_f and y_b. In matrix form, the system of algebraic equations given by (6.25) can now be written as

$$\mathrm{A}\mathbf{\Phi} = \mathbf{f} \tag{6.26}$$

where the coefficient matrix A is an asymmetric sparse matrix with each row containing at most nine non-zero entries. For a grid of size $m \times n$, A is of size $mn \times mn$, and $\mathbf{\Phi}$ and $\mathbf{f}$ are mn-component vectors. Partitioning A, $\mathbf{\Phi}$ and $\mathbf{f}$ into sub-matrices corresponding to the interior and the boundaries, equation (6.26) can be written as

$$\begin{pmatrix} \mathrm{A_L} & \mathbf{0} & \mathbf{0} & \mathbf{0} & \mathbf{0} \\ \mathbf{0} & \mathrm{A_B} & \mathbf{0} & \mathbf{0} & \mathbf{0} \\ \mathbf{0} & \mathbf{0} & \mathrm{A_D} & \mathbf{0} & \mathbf{0} \\ \mathbf{0} & \mathbf{0} & \mathbf{0} & \mathrm{A_T} & \mathbf{0} \\ \mathbf{0} & \mathbf{0} & \mathbf{0} & \mathbf{0} & \mathrm{A_R} \end{pmatrix} \begin{pmatrix} \mathbf{\Phi_L} \\ \mathbf{\Phi_B} \\ \mathbf{\Phi_D} \\ \mathbf{\Phi_T} \\ \mathbf{\Phi_R} \end{pmatrix} = \begin{pmatrix} \mathbf{f_L} \\ \mathbf{f_B} \\ \mathbf{f_D} \\ \mathbf{f_T} \\ \mathbf{f_R} \end{pmatrix},$$

where suffixes L, R, B and T stand respectively for the left, right, bottom and top boundaries of the domain and D represents the interior. The structures of the partitioned matrices appearing in the left hand side of the expression following equation (6.26) are similar to those following equation (4.12) in Chapter 4. Likewise, the vectors $[f_L]_{(n-2)\times 1}$, $[f_R]_{(n-2)\times 1}$, $[f_B]_{m\times 1}$ and $[f_T]_{m\times 1}$ correspond respectively to the left, right, bottom and top boundary conditions, and the entries of $[f_D]_{(m-2)(n-2)\times 1}$ are given by the right hand side of equation (6.26).

The next step is to solve equation (6.26) with iterative methods. On uniform grids, some of the associated matrices are symmetric and positive definite, which allows algorithms like conjugate gradient (CG) [37] to be used. As nonuniform grid invariably leads to unsymmetric matrices, in order to solve these systems, the hybrid biconjugate gradient stabilized method (BiCGStab(2)) [37,62] is used without preconditioning. For a problem having Dirichlet boundary conditions, A will have at most $2[m+n-2]+9\times(m-2)(n-2)$ non-zero entries. Therefore, for such iterative methods, the computation of the matrix-vector product $A\Phi$ involves $2[m+n-2]+81\times(m-2)(n-2)$ arithmetic operations only.

It may be noted that for the coupled nonlinear PDEs (such as the ψ-ω form of the N-S equations), an iterative solution procedure must be adopted. These iterations may be termed as outer iterations. We use a decoupled algorithm where vorticity and stream-functions are solved iteratively and sequentially through hybrid BiCGStab(2) and lagging the appropriate terms. The latter iterations may be termed inner iterations which must be carried out at every outer iteration with updated data.

6.3 Numerical Test Cases

The proposed scheme has been applied to two linear and two nonlinear test cases. The nonlinear cases deal with the fluid flows governed by the 2D steady-state incompressible N-S equations. Care has been taken to choose such problems as will permit the use of nonuniform grids at certain portions of the solution domain for better scale resolution with grid economy. Both Dirichlet and Neumann boundary conditions have been used wherever necessary.

6.3.1 Problem 1.

We take the problem proposed by Gartland [22], where in equation (2.3),

$$c = Re, \quad d = 0, \quad f = 0 \quad \forall \quad 0 \le x, y \le 1,$$

with boundary conditions

$$\phi(x,0) = \phi(x,1) = 0 \qquad 0 \le y \le 1$$

$$\phi(0,y) = \phi(1,y) = \sin \pi y \qquad 0 \le x \le 1$$

The exact solution is given by

$$\phi(x,y) = e^{\frac{Rex}{2}} \sin \pi y \frac{2e^{-\frac{Re}{2}} \sinh \sigma x + \sinh \sigma (1-x)}{\sinh \sigma}, \quad \sigma^2 = \pi^2 + \frac{Re^2}{4}. \quad (6.27)$$

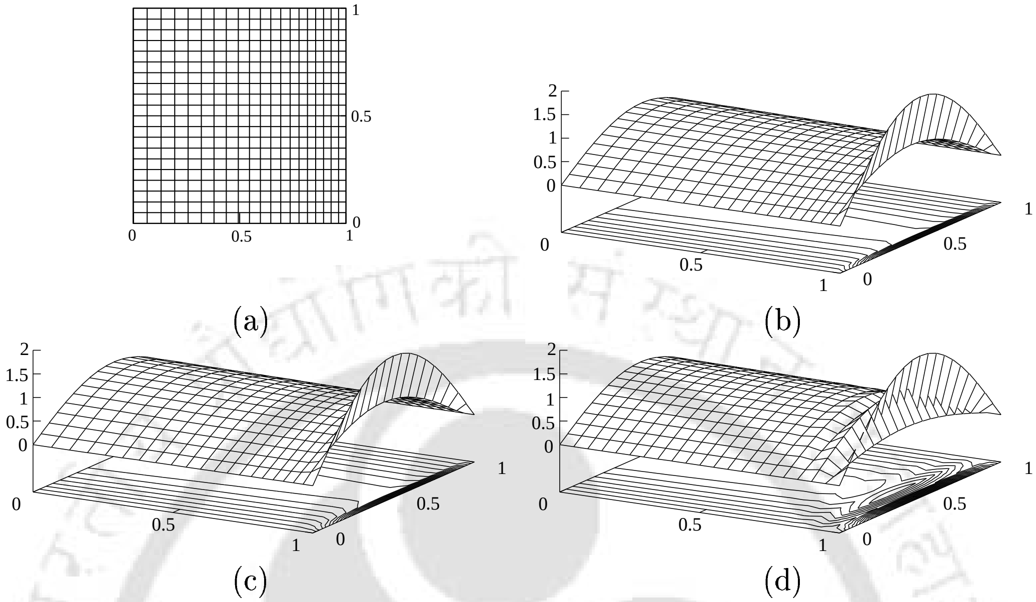

(a) (b) (c) (d)

Figure 6.2: *For problem 1, at* $Re = 100$*: (a) The grid used* (21×21) *and the surface and contour plots of (b) the analytical solution, (c) the present scheme* ($\lambda = 0.5$) *and (d) the CD scheme.*

The solution has a boundary layer attached to the line $x = 1$ and therefore, a uniform grid along the y-direction, and a nonuniform grid along the x-direction with clustering near $x = 1$ has been used with the following stretching function [69]

$$x_i = \frac{i}{i_{max}} + \frac{\lambda}{\pi} \sin\left(\frac{\pi i}{i_{max}}\right),$$

where λ is a stretching parameter controlling the density of grid points in the x-direction. It may be noted that higher the value of λ, greater the clustering near the boundary. The grid is shown in Figure 6.2 (a). Figures 6.2 (b), (c) and (d) respectively show the surface and contour plots of the exact, the numerical solution with the present scheme ($\lambda = 0.5$) and the numerical solution with the central difference (CD) scheme on a 21×21 grid for $Re = 100$. While the numerical solution with the present scheme shows no discernible differences with the exact solution, the CD solution shows a clear oscillation in the region of the boundary layer. This is attributed to the violation of the so-called cell-Péclect condition

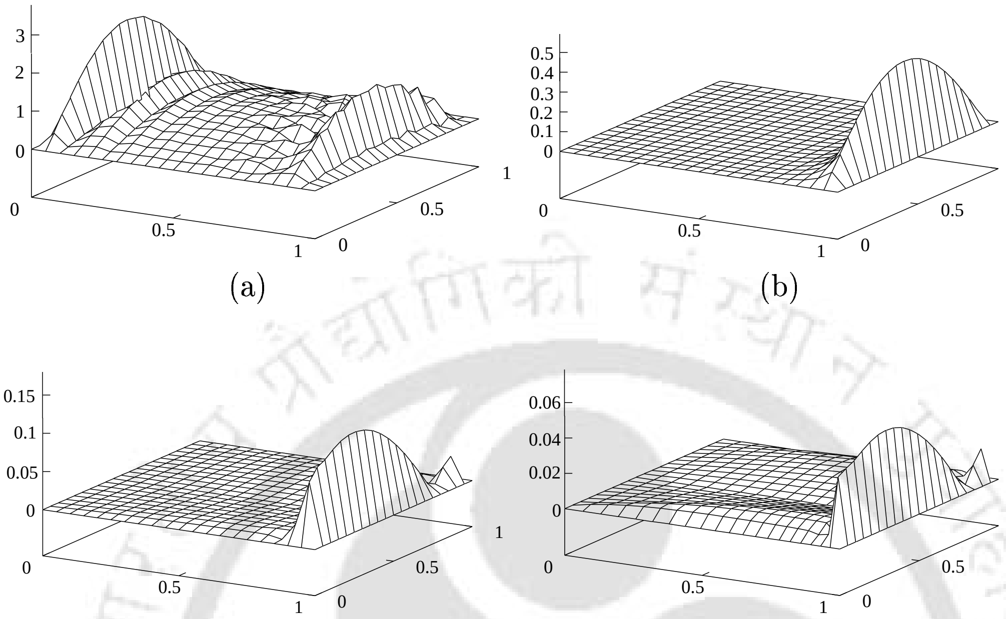

(a) (b)

(c) (d)

Figure 6.3: *Surface plots of the absolute errors for problem 1 (Re=100, 21×21 grid), (a) Upwind, (b) Central difference, (c) Uniform HOC and (d) Present scheme ($\lambda = 0.5$).*

$$Re_{\Delta x} = Re\Delta x < 2 \quad \text{or} \quad \Delta x < \frac{2}{Re}.$$

On the other hand the maximum and the minimum values of Δx with our scheme are 0.064 and 0.045, which being greater than the limit 0.02, clearly violates the above condition. Inspite of this violation, no oscillation is seen in our results which indicates that our scheme has the oscillation suppressing property. Also the surface plots of the absolute errors (Fig. 6.3) for the upwind, CD, HOC uniform and the present scheme for the same problem confirms that, the present scheme yields the best result. Table 6.1 compares the maximum error (max(er)) and the root mean square error (rms(er)) of the HOC scheme on a uniform grid with those of the present scheme for different λ's and grid sizes. Max(er) of the present scheme for all λ's is lower than that of the uniform grid whereas rms(er) for higher clustering on finer grids may be higher.

Table 6.1: *Comparison of the errors on the uniform and nonuniform grids for Problem 1.*

Grid	Uniform	
	rm(er)	max(er)
26×26	1.09×10^{-2}	8.12×10^{-2}
51×51	1.41×10^{-3}	1.27×10^{-2}
101×101	2.45×10^{-4}	2.37×10^{-3}
Grid	Non uniform ($\lambda = 0.5$)	
	rm(er)	max(er)
26×26	5.21×10^{-3}	2.86×10^{-2}
51×51	9.50×10^{-4}	4.76×10^{-3}
101×101	2.23×10^{-4}	9.21×10^{-4}
Grid	Non uniform ($\lambda = 0.6$)	
	rm(er)	max(er)
26×26	4.69×10^{-3}	2.18×10^{-2}
51×51	9.63×10^{-4}	3.75×10^{-3}
101×101	2.34×10^{-4}	7.20×10^{-4}
Grid	Non uniform ($\lambda = 0.7$)	
	rm(er)	max(er)
26×26	4.42×10^{-3}	1.60×10^{-2}
51×51	1.00×10^{-3}	2.88×10^{-3}
101×101	2.49×10^{-4}	5.75×10^{-4}
Grid	Non uniform ($\lambda = 0.8$)	
	rm(er)	max(er)
26×26	4.36×10^{-3}	1.11×10^{-2}
51×51	1.06×10^{-3}	2.12×10^{-3}
101×101	2.67×10^{-4}	4.73×10^{-4}

6.3.2 Problem 2.

The domain of this problem is the same as that of problem 1 and in equation (2.3), $c = Re\cos\theta$, $d = Re\sin\theta$ and $f = 0$ with boundary conditions

$$\phi(x,0) = \phi(x,1) = 0 \qquad 0 \le x \le 1,$$

$$\phi(0,y) = 4y(1-y) \qquad \phi(1,y) = 0, \quad 0 \le y \le 1.$$

This problem has the exact solution

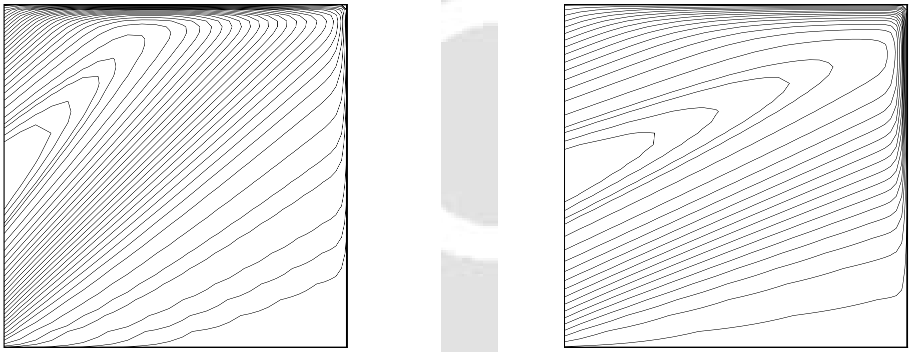

(a) (b)

Figure 6.4: *The contour plots of the Problem 2 for* $Re = 80$: *(a)* $\theta = \frac{\pi}{4}$, *(b)* $\theta = \frac{\pi}{8}$.

$$\phi(x,y) = exp\left(-\frac{Re}{2}(x\cos\theta + y\sin\theta)\right)\sum_{n=1}^{\infty}\{B_n\sinh[\sigma_n(1-x)]\sin(n\pi y)\} \tag{6.28}$$

where

$$\sigma_n^2 = n^2\pi^2 + \frac{\alpha^2}{4}$$

and

$$B_n = \frac{8}{\sinh\sigma_n}\int_0^1 y(1-y)exp\left(\frac{-\alpha y}{2}\sin\theta\right)\sin(n\pi y)dy$$

The problem deals with the convection of ϕ (temperature or concentration) in a fluid moving with a uniform velocity at an angle θ to the x-axis. It has earlier been solved numerically by Gupta *et al.* [26] and Mackinnon and Johnson [42]. The present computation uses the stretching function of Problem 1 to generate clustered grids with refinement near x=1 and y=1. The method captures the boundary layers developed on $x = 1$ and $y = 1$ very well as can be seen from from Figure 6.4 where the computed contours of ϕ has been plotted for two convection angles $\frac{\pi}{4}$ and $\frac{\pi}{8}$. Table 6.2 compares of the max(er) for $Re = 40$ for three convection angles, viz., $\frac{\pi}{4}$, $\frac{\pi}{8}$ and 0 with those obtained from the Upwind Difference Scheme (UDS), the Central Difference Scheme (CDS), and the higher order schemes of Gupta *et al.* [26] and Spotz and Carey [66] for different grid sizes. When judged against the orders of accuracy of the other schemes, the errors of the present computations are within the expected limits.

Table 6.2: *Comparison of the maximum errors on the uniform and nonuniform grids for different schemes in Problem 2 with stretching factor* $\lambda = 0.8$.

θ	Grids	UDS $O(h)$	CDS $O(h^2)$	Gupta $O(h^4)$	Spotz $O(h^4)$	Present $O(h^3)$ to $O(h^4)$
0	16×16	0.1604	0.1532	0.01323	0.04050	0.01403
	32×32	0.1256	0.0445	0.00112	0.00856	0.00306
$\frac{\pi}{8}$	16×16	0.2268	0.1286	0.01019	0.01769	0.02992
	32×32	0.1394	0.0348	0.00081	0.00492	0.00759
$\frac{\pi}{4}$	16×16	0.2035	0.0803	0.00598	0.00598	0.00496
	32×32	0.1218	0.0195	0.00041	0.00041	0.00046

6.3.3 Problem 3: Lid-driven Cavity Flow

The solution procedure is now extended to the 2D laminar lid-driven square cavity problem which has been used extensively to study the strength and accuracy of numerical methods for incompressible flow problems. This flow is governed by the 2D incompressible N-S equations. The stream-function-

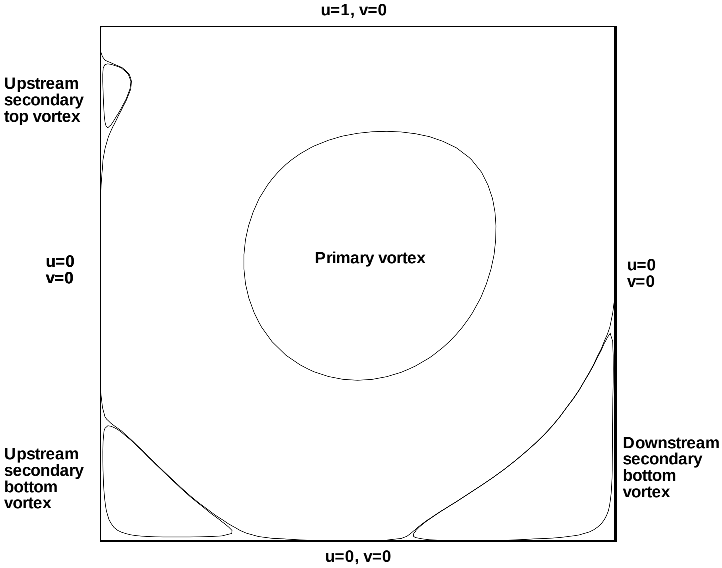

Figure 6.5: *The lid-driven cavity flow configuration with boundary conditions.*

vorticity (ψ-ω) form of these equations has been used in the present computations. The geometry and the boundary conditions have been shown in Fig. 6.5 where the top wall is moving from left to right and the remaining three walls are stationary. The flow is driven by the moving wall and the resultant flow patterns depend on Re. Because of the presence of large gradients near the walls, grid has been clustered there using the stretching function

$$x_i = \frac{i}{i_{max}} - \frac{\lambda}{2\pi} \sin\left(\frac{2\pi i}{i_{max}}\right), \quad 0 < \lambda \leq 1$$

which we obtain by combining the functions used by Spotz and Carey [69] and Janssen and Henkes [32]. Here, the parameter λ determines the degree of clustering near the boundaries with centrosymmetric stretching. The effect of λ on grids can be seen from Figs. 6.6 (a) and (b) where a uniform and a clustered 81×81 grid have been shown. Numerical results are presented for Re's ranging from 0 to 7500 with grid sizes varying from 11×11 to 121×121. As the boundary layer thickness is of the order of $Re^{-0.5}$, grid size and λ have been chosen in such a way that there are several points within the boundary

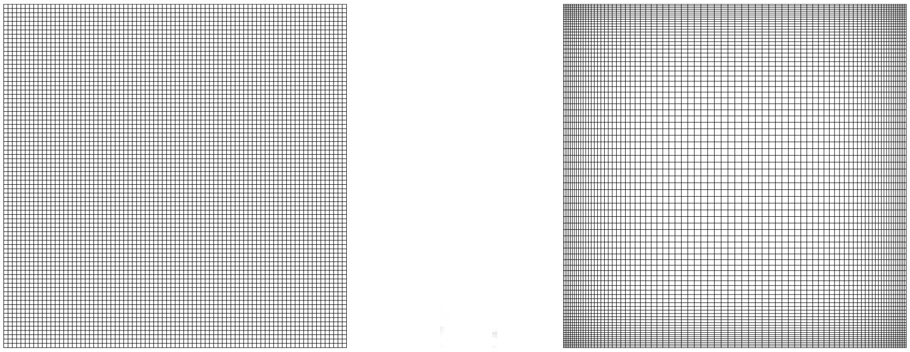
(a) (b)

Figure 6.6: 81×81 *grids for square cavity: (a) uniform and (b) clustered with* $\lambda = 0.6$.

layer. For example, the minimum internodal distance near the wall is 0.0345 for $Re = 100$ (11×11, $\lambda = 0.7$) and 1.37×10^{-4} for $Re = 3200$ (81×81, $\lambda = 0.99$). The Neumann boundary conditions for vorticity are obtained through a third order compact formula [67] as a fourth order compact boundary scheme is

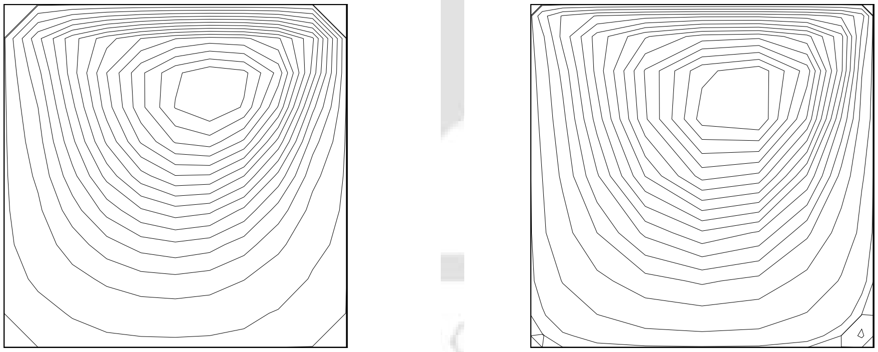
(a) (b)

Figure 6.7: *Streamlines for the lid-driven cavity flow on* 11×11 *grid for* $Re = 100$*: (a) uniform HOC and (b) present scheme* ($\lambda = 0.7$).

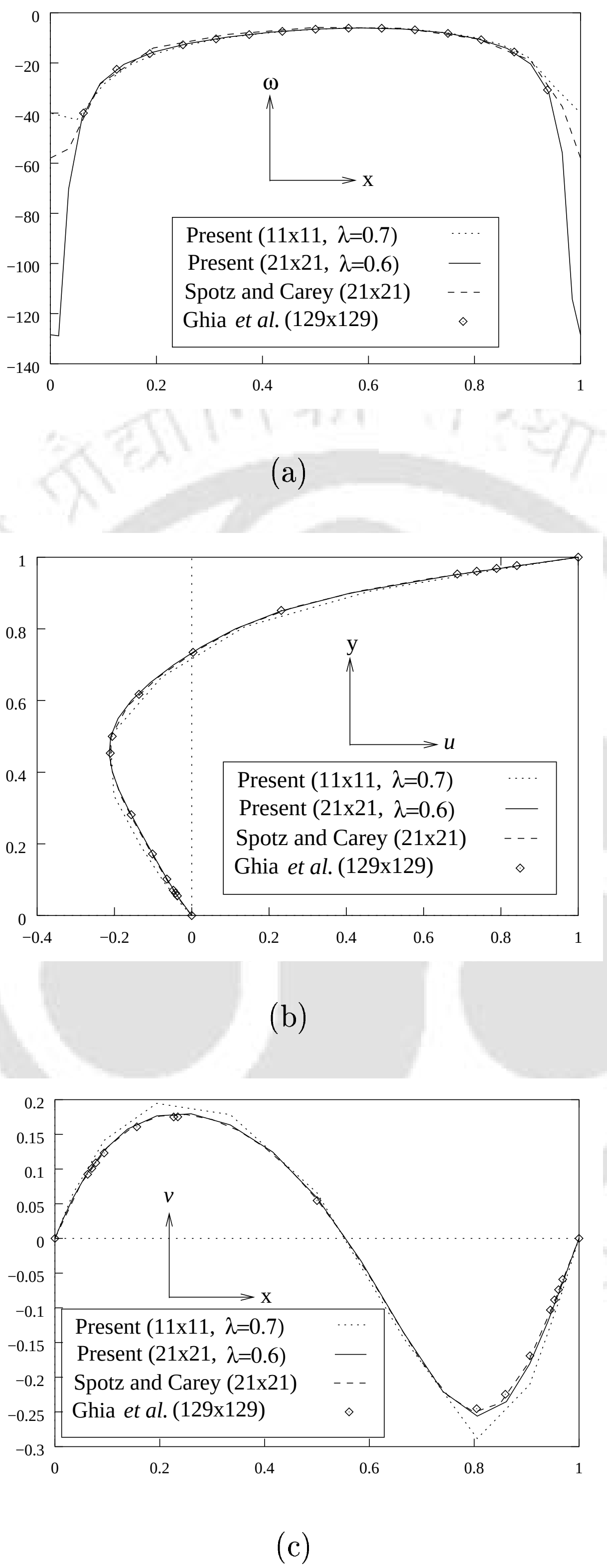

Figure 6.8: *Comparisons of (a) vorticity along the moving wall, (b) horizontal velocity along the vertical centreline and (c) vertical velocity along the horizontal centreline for Re=100 in the lid-driven cavity flow.*

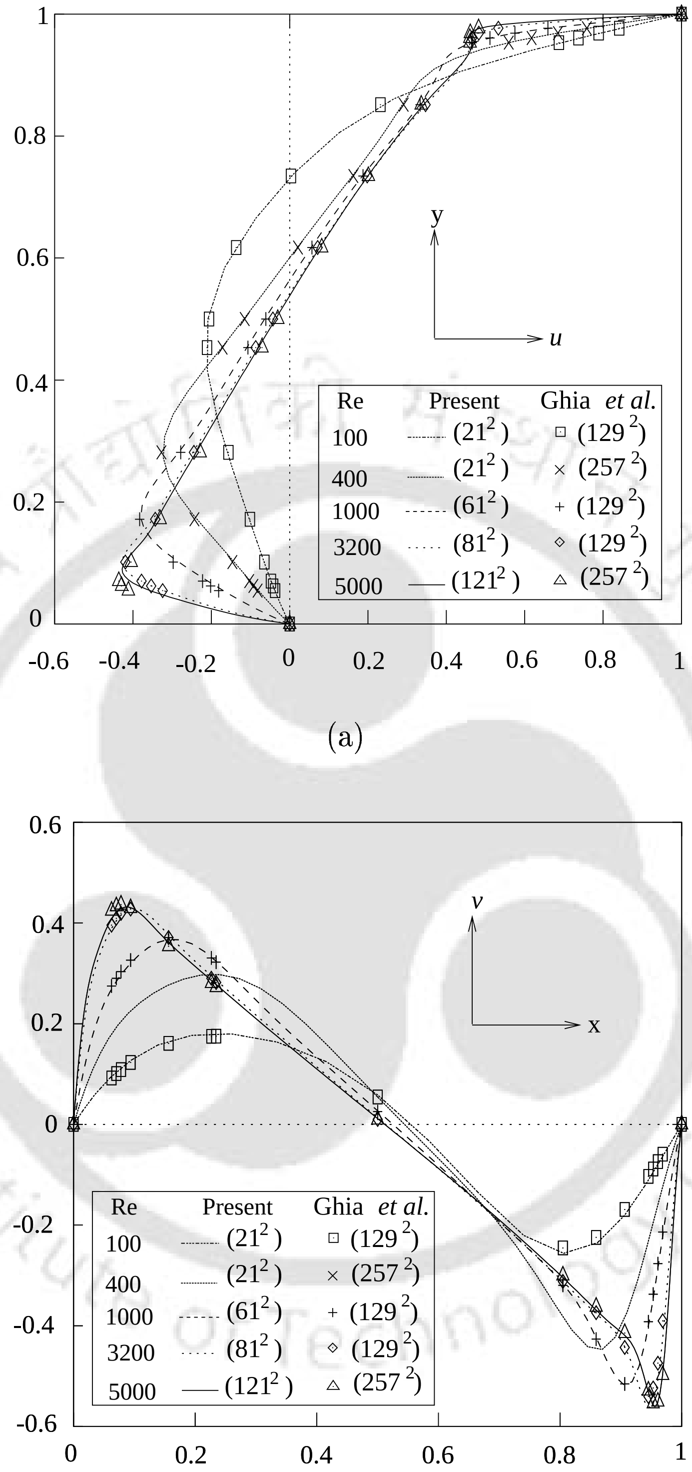

(a)

(b)

Figure 6.9: *Comparisons of (a) horizontal velocity along the vertical centreline and (b) vertical velocity along the horizontal centreline for different Re's in the lid-driven cavity flow ($\lambda = 0.6$).*

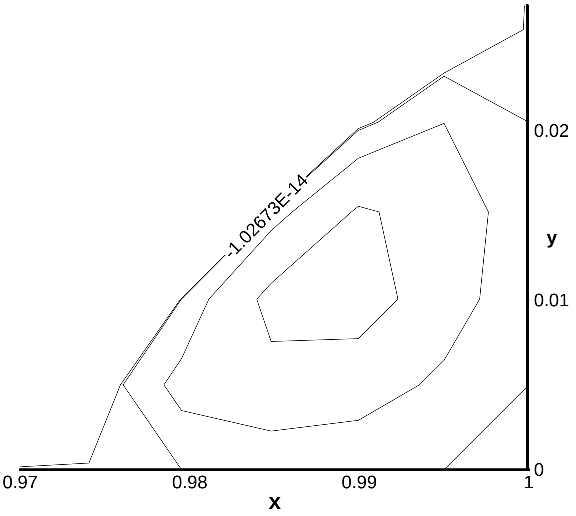

(a)

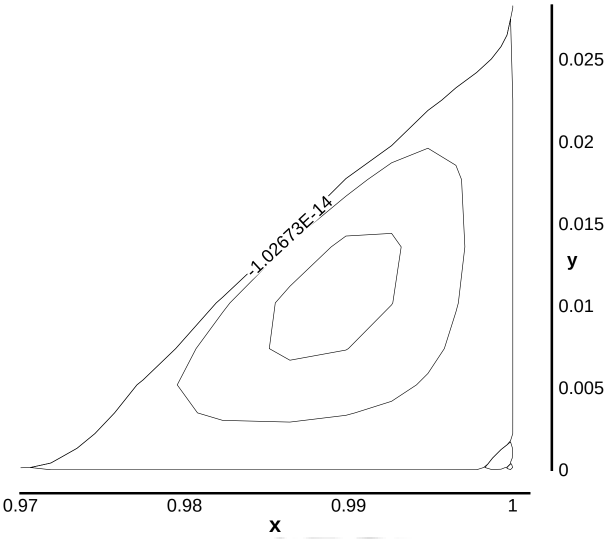

(b)

Figure 6.10: *The bottom right vortices for the lid-driven cavity flow at Re =* 3200 *on* 81 × 81 *grid: (a) tertiary (*$\lambda = 0.6$*) and (b) tertiary, quaternary and post-quaternary (*$\lambda = 0.99$*).*

found to be oscillatory at the moving wall. For $Re = 100$ the streamline contours obtained by HOC schemes on 11×11 uniform and nonuniform grids are shown in Figs. 6.7 (a) and (b). It is clear from the figures that the fourth order accurate scheme on uniform grids captures none of the corner vortices whereas the present scheme with accuracy lower than fourth does. Interestingly the present scheme with a grid as coarse as 21×21 ($\lambda = 0.6$) captures the flow details quite accurately as can be seen from the comparison with the results of Ghia *et al.* [24] produced with a 129×129 grid (Fig. 6.8). The centreline velocity profiles obtained through the present scheme with those of Ghia *et al.* [24] are presented side by side in Fig. 6.9 for different Re's. Again it is seen that the present scheme computes the flow with a much coarser grid. The significance of grid clustering at high Re's involving multiple scales can be seen

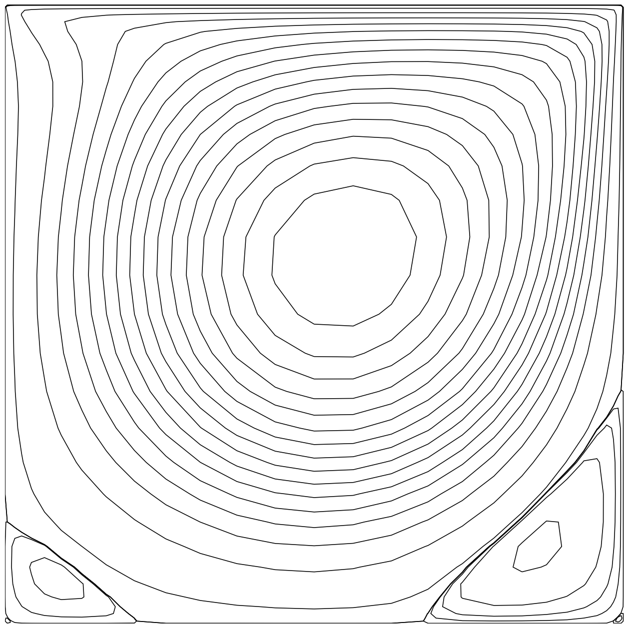

Figure 6.11: *Streamline patterns for the lid-driven cavity flow for* $Re = 1000$ *(*31×31, $\lambda = 0.9$*).*

from Fig. 6.10 where for $Re = 3200$, the corner vortex features on 81×81 grids are shown for $\lambda = 0.6$ and 0.99. With $\lambda = 0.6$ [Fig. 6.10 (a)], corner vortices only up to the tertiary level have been resolved whereas with $\lambda = 0.99$ two hitherto unreported vortices - the quaternary and post-quaternary - have been captured [Fig. 6.10 (b) - walls removed for clarity]. Fig. 6.11 (walls removed for clarity) shows the streamline contours for $Re = 1000$. It is seen that for $Re = 1000$, the present scheme on a 31×31 grid captures even the tertiary vortices whereas on uniform grid of the same size, iteration stagnates [67]. The following observations (as also can be seen from Figs. 6.12, 6.13, 6.14 and 6.15), which are in agreement with the earlier investigations [12,24,38,58], can be made with increase in Re: (i) for $Re = 0$, flow is symmetric about the vertical centreline and from $Re = 100$ onwards, the primary vortex center shifts from the top right corner towards the geometric centre of the cavity which virtually becomes invariant for $Re \geq 5000$ (Figs. 6.12 and 6.13). (ii) there is an expansion of the recirculation zone for the secondary vortices with a tendency of their centers to shift towards the geometric center (Figs. 6.12 and 6.13). The appearance of the top-left secondary vortex can be seen for $Re = 2000$ and more. (iii) several regions of high vorticity gradients indicated by the concentration of the vorticity contours, appears within the cavity (Figs. 6.14 and 6.15). As against the stream-function, they are not aligned with the geometric boundaries of the cavity. In Table 6.3, the stream-function and the vorticity values at the primary vortex centers of the present study have been compared with the calculations of Kim and Moin [38], Ghia *et al.* [24] and Bruneau and Jouron [12] and, agreement has been very close. Shown in Fig. 6.16 is the convergence history based on the root mean square error [rms(er)] of ω at $Re = 1000$ for the present scheme for two different grid sizes. This error has been defined as

$$\text{rms(er)} = \left[\frac{1}{i_{max} \times j_{max}} \sum \left(\omega^{(k+1)} - \omega^{(k)} \right)^2 \right]^{\frac{1}{2}}$$

where k and $k+1$ denote two consecutive iteration levels. The CPU times on a Sun enterprise 250 workstation for the two grids are 10.94 and 173.33 seconds respectively when the exit criteria for the fall of residuals of the inner iterations for both ψ and ω are set at 10^{-3}.

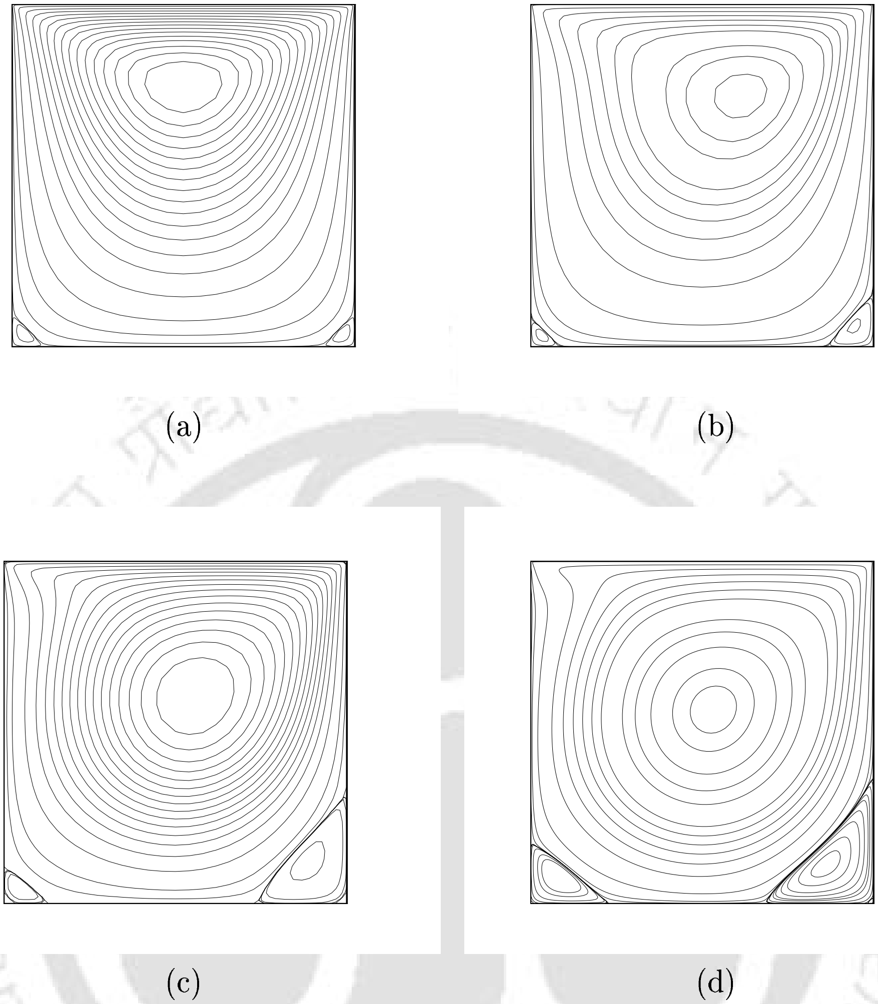
(a) (b) (c) (d)

Figure 6.12: *Stream function contours for the lid-driven cavity flow for (a) $Re = 0$, (b) $Re = 100$, (c) $Re = 400$ and (d) $Re = 1000$.*

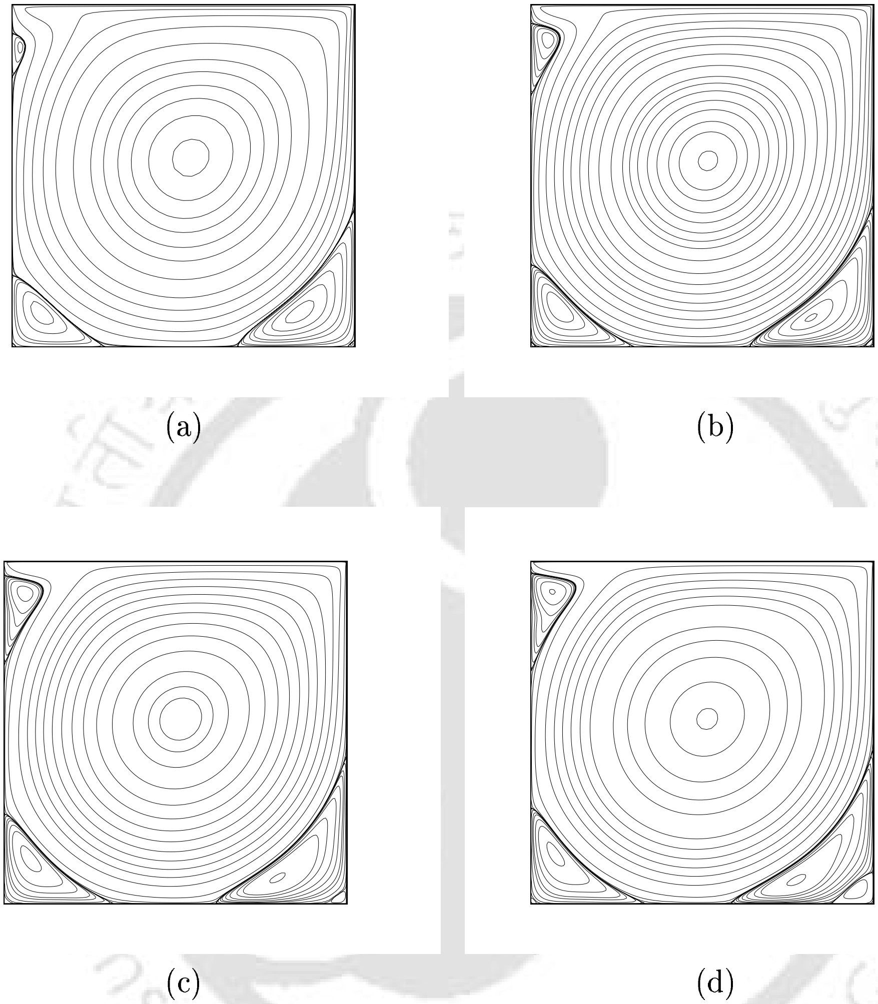

(a) (b) (c) (d)

Figure 6.13: *Stream function contours for the lid-driven cavity flow for (a)* $Re = 2000$*, (b)* $Re = 3200$*, (c)* $Re = 5000$ *and (d)* $Re = 7500$*.*

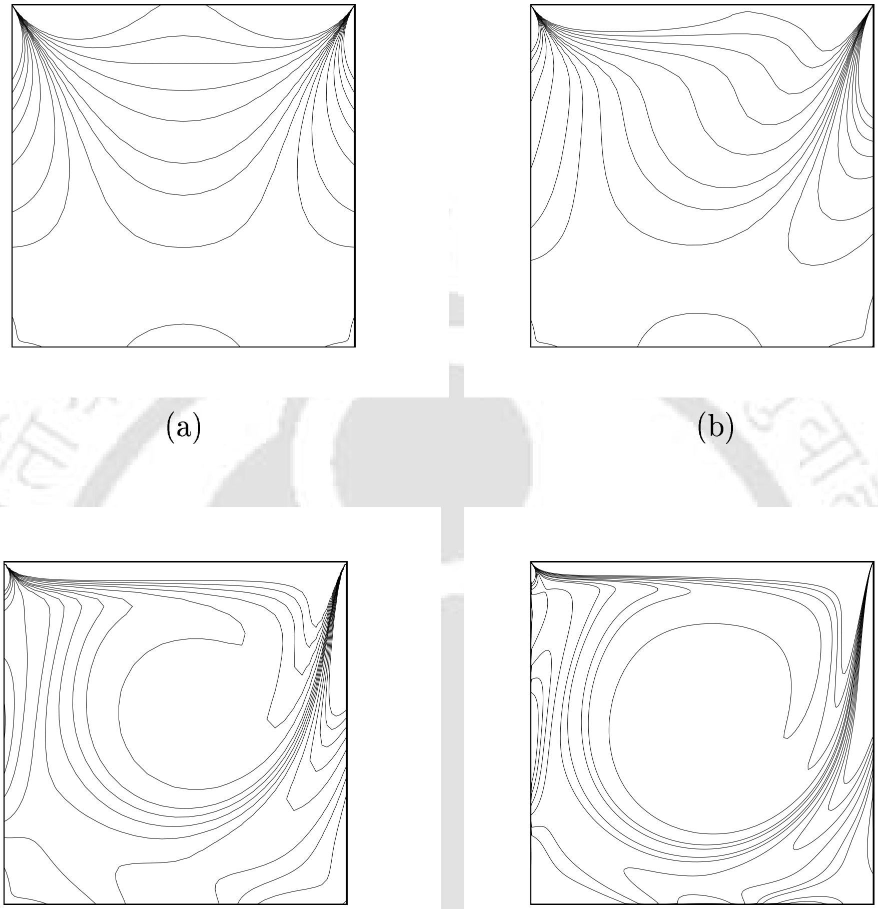

(a) (b)

(c) (d)

Figure 6.14: *Vorticity contours for the lid-driven cavity flow for (a)* $Re = 0$*, (b)* $Re = 100$*, (c)* $Re = 400$ *and (d)* $Re = 1000$*.*

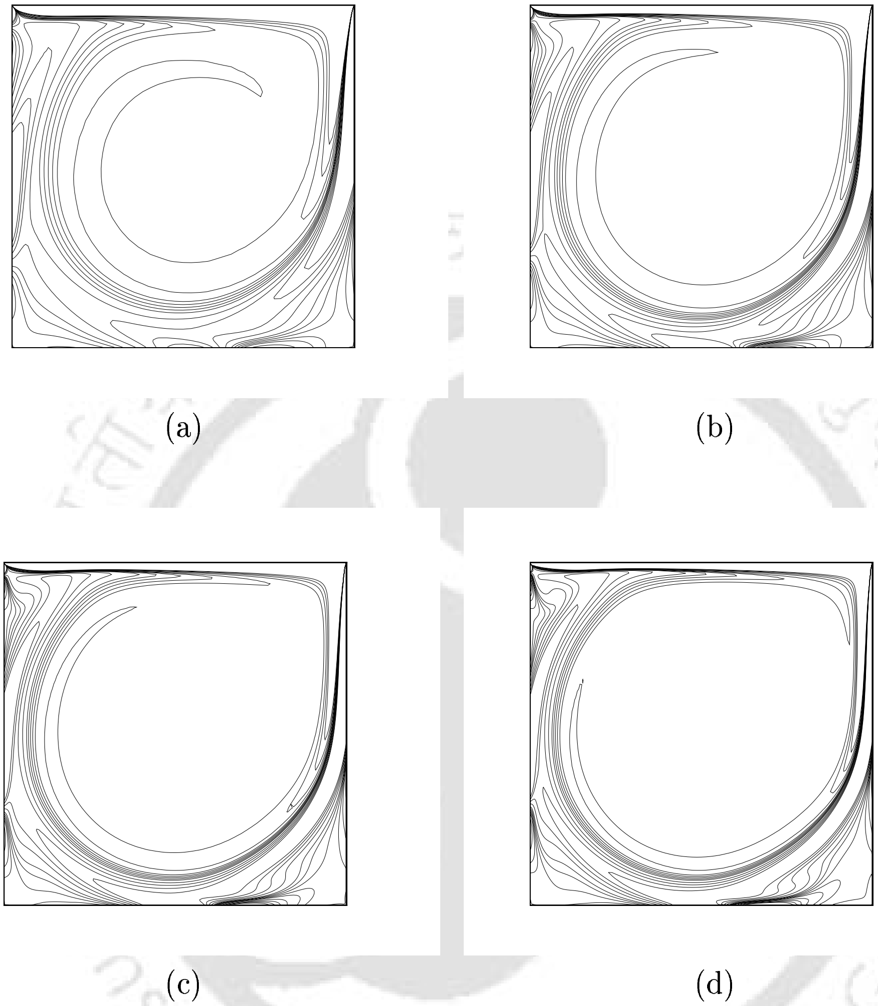

(a)

(b)

(c)

(d)

Figure 6.15: *Vorticity contours for the lid-driven cavity flow for (a)* $Re = 2000$, *(b)* $Re = 3200$, *(c)* $Re = 5000$ *and (d)* $Re = 7500$.

Table 6.3: *Stream function and vorticity at primary vortex center for Different Reynolds numbers.*

Re	Kim and Moin	Ghia *et al.*	Bruneau	Present ($\lambda = 0.6$)
100	$-0.103(-3.177)$ 65×65	$-0.103(-3.166)$ 129×129	$-0.103(--)$ 128×128	$-0.103(-3.152)$ 41×41
400	$-0.112(-2.260)$ 65×65	$-0.114(-2.295)$ 257×257	$--$ $--$	$-0.113(-2.260)$ 41×41
1000	$-0.116(-2.026)$ 97×97	$-0.118(-2.050)$ 129×129	$-0.116(--)$ 256×256	$-0.117(-2.057)$ 61×61
3200	$-0.115(-1.901)$ 97×97	$-0.120(-1.989)$ 129×129	$--$ $--$	$-0.120(-1.962)$ 81×81
5000	$-0.112(-1.812)$ 97×97	$-0.119(-1.860)$ 257×257	$-0.114(--)$ 512×512	$-0.119(-1.926)$ 81×81
7500	$--$ $--$	$-0.120(-1.880)$ 257×257	$-0.111(--)$ 512×512	$-0.115(-1.874)$ 121×121

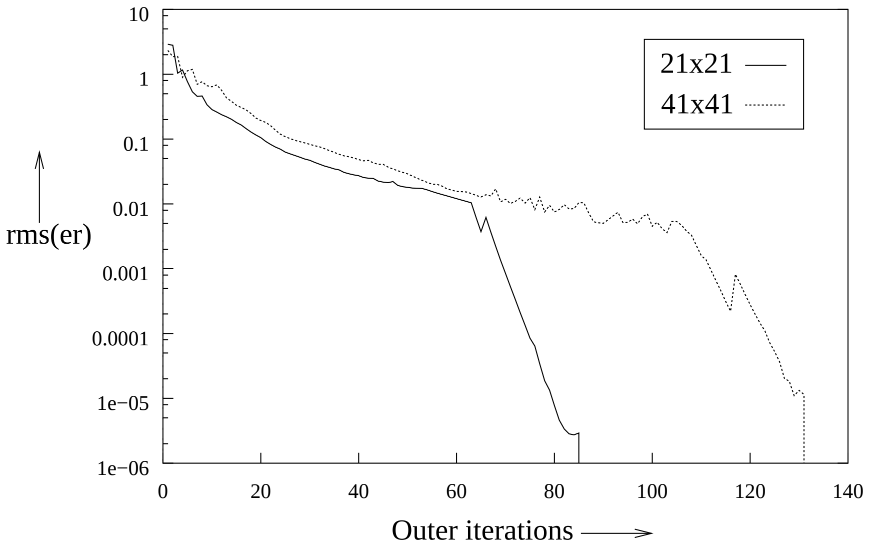

Figure 6.16: *Convergence history based on the root mean square error of* ω *for Re=1000* ($\lambda = 0.8$) *in the lid-driven cavity flow.*

6.3.4 Problem 4: The Backward-facing Step Flow

Next we consider the flow over the backward-facing step in a channel which provides an excellent test case for the accuracy of numerical methods because of the reattachment length being a function of the Reynolds number. The governing equations are the incompressible 2D N-S equations and the ψ-ω formulation has been used here as well. The problem configuration is shown in Figure 6.17. At the inlet, a parabolic velocity profile is usually prescribed [7,23,33,38] and the one used here is given by Gartling [23] as $u = 24y(0.5-y)$, $v = 0$. The downstream boundary conditions are prescribed at a distance of 30 step heights, where the fully developed velocity profile can be determined by equating the flow rates at the inlet and the outlet. Thus the outlet velocity becomes $u = 0.75(1-4y^2)$, $v = 0$. The corresponding ψ and ω at these boundaries can easily be found from the velocity profiles. At the stationary walls, as in problem 3, a Neumann vorticity BC is prescribed using a third order compact formula [66]. Numerical simulations are carried out for the range of Reynolds numbers (Re) from 100 to 800. It is defined as $Re = \dfrac{u_{av}L}{\nu}$ [23] where u_{av} is the average inlet velocity, L is the channel height and ν is the kinematic viscosity of the fluid. In all the computations, a 81×21 grid was

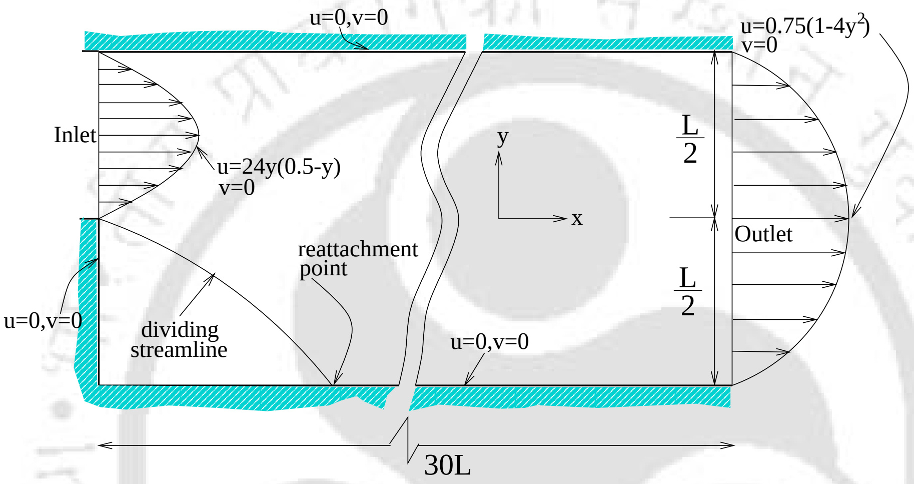

Figure 6.17: *Backward-facing step geometry with boundary conditions and channel dimensions.*

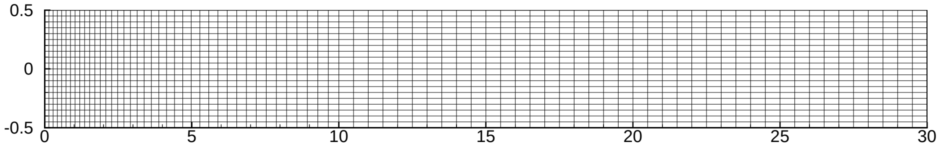

Figure 6.18: *Grid spacing for the backward facing step flow.*

enough to capture the flow (Figure 6.18). In the streamwise direction x, as a finer grid is necessary to capture the recirculation zone, a stretching grid is used in the zone $0 \leq x \leq 10$ and uniformity is maintained thereafter. Although boundary layers exist near both the top and bottom walls and as such a grid refinement indicated, we use a uniform grid as the number of grid points necessary to resolve the normal gradients is moderate for the flow considered [70]. Figures 6.19 and 6.20 show the streamline and vorticity patterns for Re=200, 400, 600 and 800. For the same Re's, the velocity vector (relative and uniform) plots are shown in Figures 6.21 and 6.22. The spacing in the y-direction has been magnified twice for a better resolution. The formation of a secondary vortex at the upper wall can be seen with increasing Re's. In our simulations, this vortex is visible for Re=500 (figure not shown) and above. This is also reported by John [33] who used the FIDAP code. The velocity vector plots give a clear picture of the recirculation zones and the velocity profiles at different streamwise locations, indicating the development of a parabolic profile towards the exit. In Figure 6.23, the re-attachment length as a function of Reynolds number is shown against the experimental and computational results of Armaly *et al.* [7] and the numerical results of Kim and Moin [38]. As they give no tabular results, the graphical results were optically scanned to produce the cited quantities. Our results are in excellent agreement with the experimental results of Armaly *et al.* [7] for the whole range of Re from 0 to 800, whereas those of the previous numerical experiments [7, 23, 38] failed to tally with the same experimental results for $Re > 600$. The reason was thought to be because of the three-dimensionality

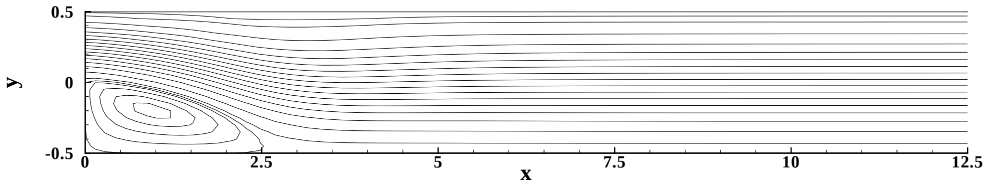

(a) Re=200

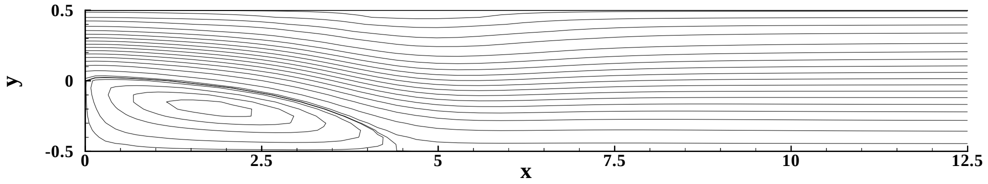

(b) Re=400

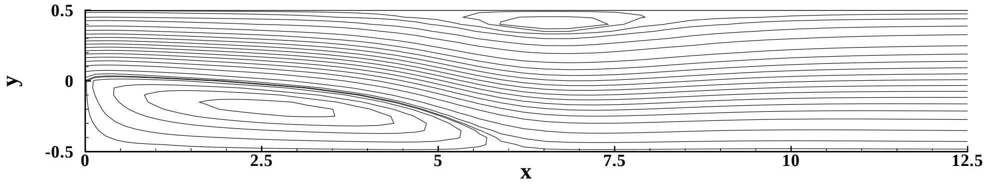

(c) Re=600

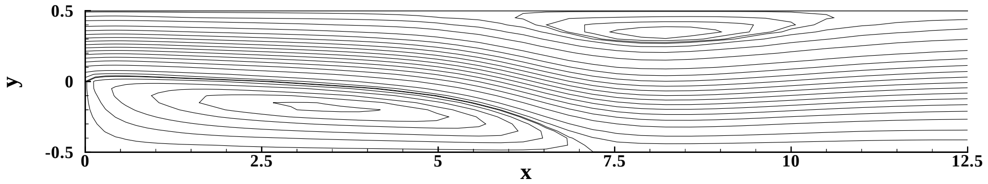

(d) Re=800

Figure 6.19: *Streamlines for the backward facing step flow.*

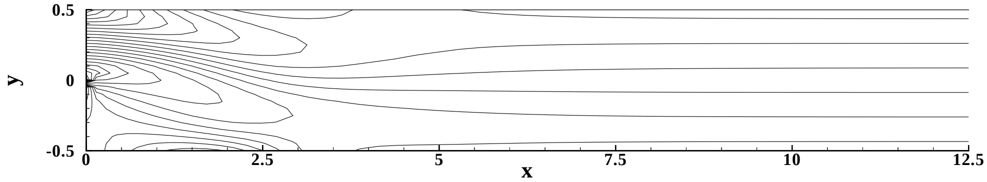

(a) Re=200

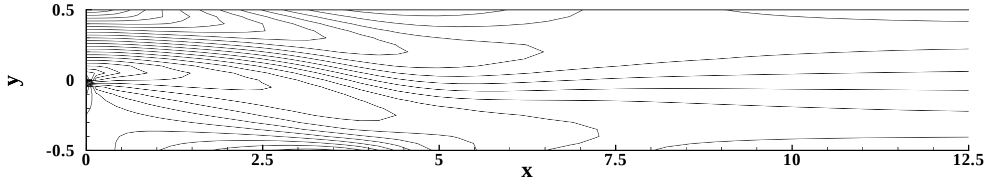

(b) Re=400

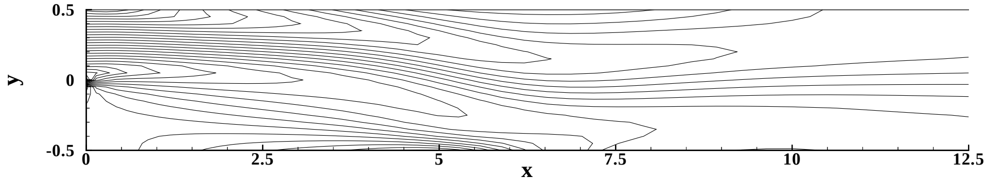

(c) Re=600

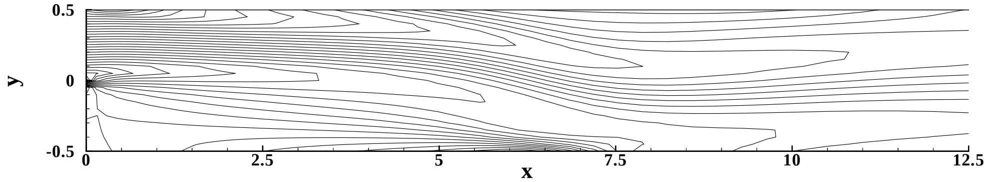

(d) Re=800

Figure 6.20: *Vorticity contours for the backward facing step flow.*

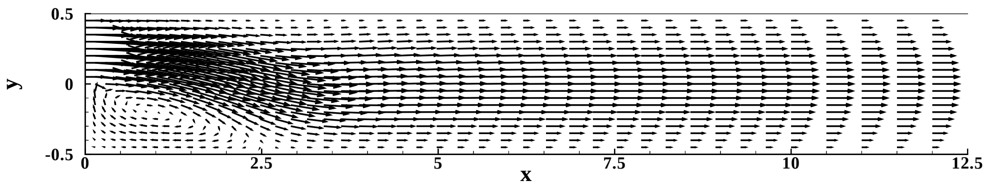

(a) Re=200

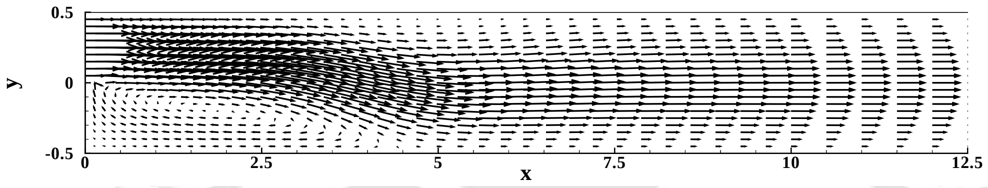

(b) Re=400

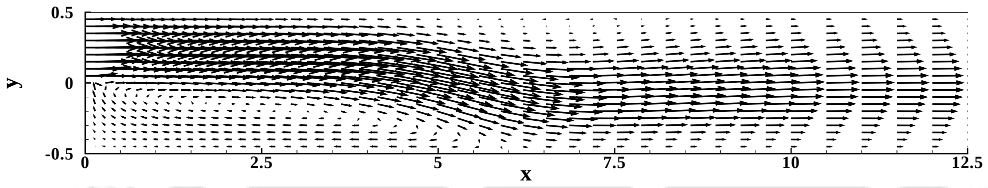

(c) Re=600

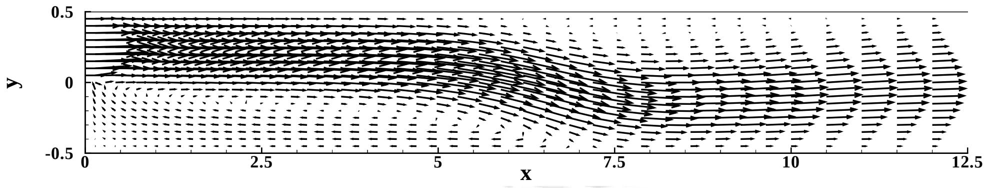

(d) Re=800

Figure 6.21: *Velocity vectors (in magnitude) for the backward facing step flow.*

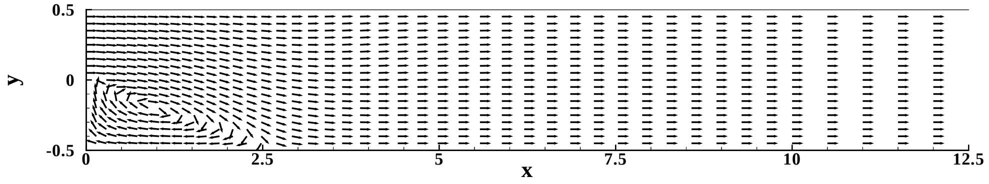

(a) Re=200

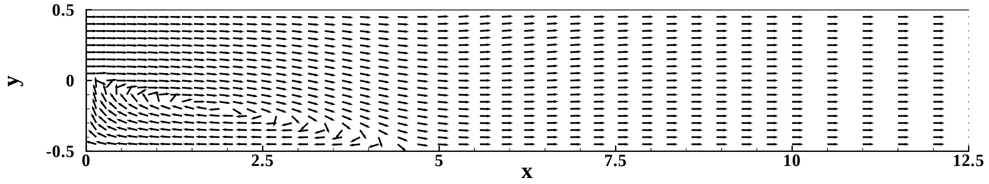

(b) Re=400

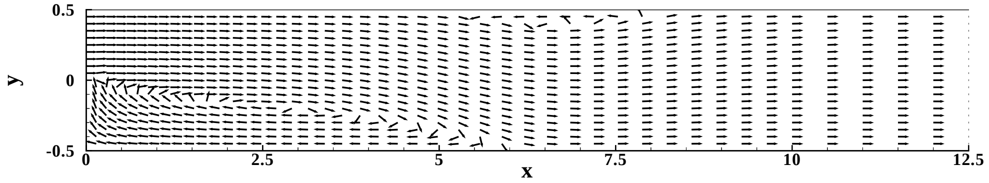

(c) Re=600

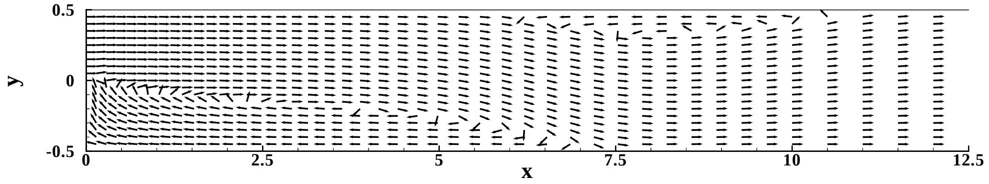

(d) Re=800

Figure 6.22: *Uniform velocity vectors for the backward facing step flow.*

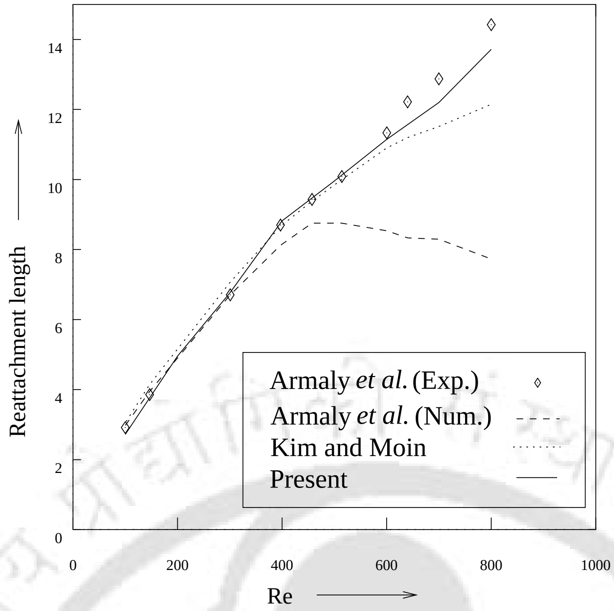

Figure 6.23: *Re-attachment length as a function of Reynolds number.*

of this flow at $Re \geq 400$. Streamwise velocity profiles along vertical lines through the centers of the upper and lower eddy for Re=800 in Figure 6.24 gives a clear picture of the recirculation and the associated flow reversals.

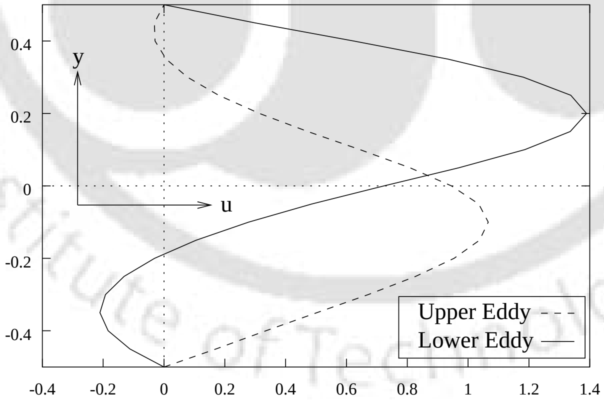

Figure 6.24: *The streamwise velocity profile along the vertical lines through the centers of the upper and lower eddy for Re=800 in the backward-facing step flow.*

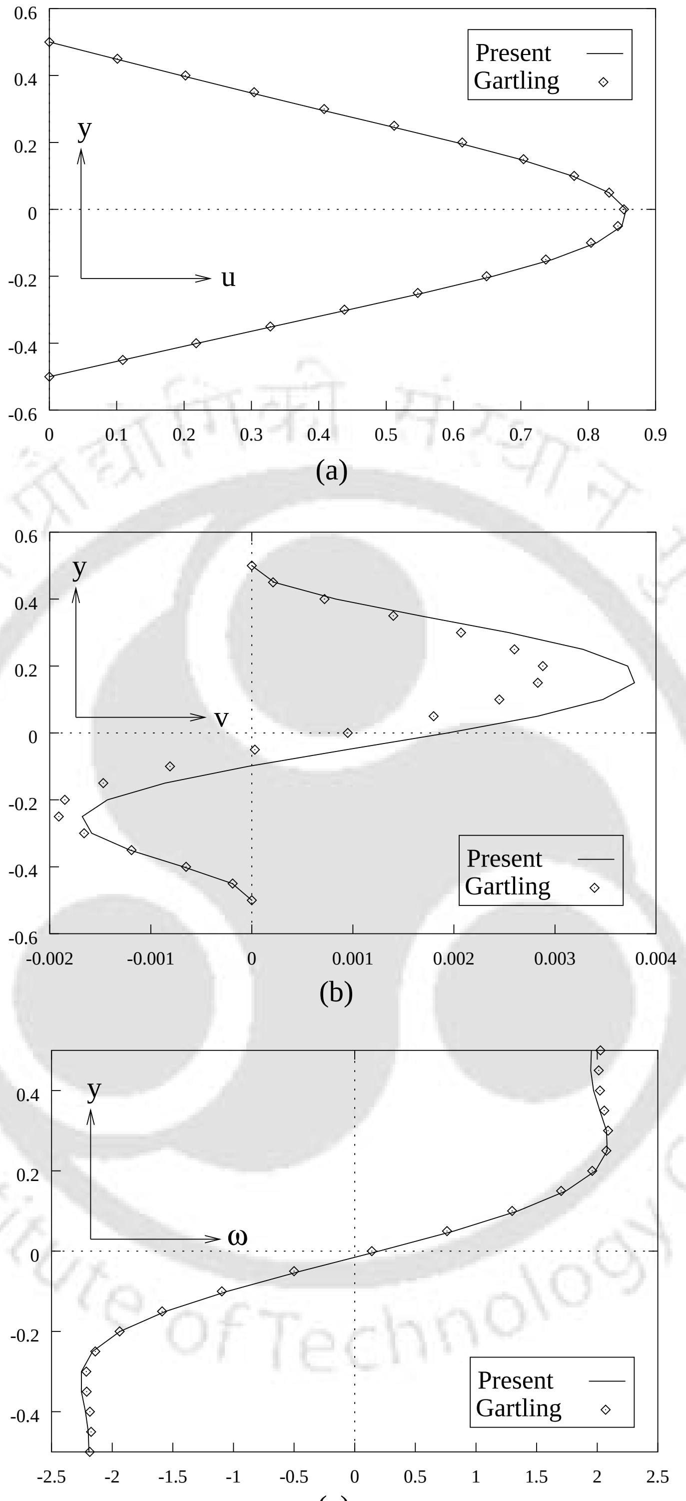

(a)

(b)

(c)

Figure 6.25: *Comparison with Gartling for (a) Horizontal velocity profile, (b) Vertical velocity profile and (c) the vorticity at* $x = 15$ *for* $Re = 800$.

Figure 6.25 presents, at station x=15, the distributions of u, v and ω along with those of Gartling [23] and agreement in u and ω is observed to be close. However, the distribution of v does not agree as closely which fact has also been observed by Srinivasan and Rubin [70]. Again, the upper wall separation length l_u=4.31 found by this study is much closer to the experimental value $l_u \approx 4.1$ of Armaly *et al.* [7] against the predicted values of $l_u \approx 4.7$, 5.63 and 5.75 of John [23, 33]Gartling and Kim and Moin [38] respectively.

6.4 Conclusion

The HOC scheme on nonuniform grids for convection-diffusion has so far been tested only for linear problems with grid transformation. The present work affords an HOC method on nonuniform grids which avoids the complexities associated with transformation. Dispensing with transformation also reduces computational effort as the method now deals with smaller number of terms at each grid point. Because of clustering the method is seen to produce accurate solution of complex flows with significantly smaller number of grid points with resultant economy. For instance, a 31 × 31 grid is found to be good enough to capture the flow details including the tertiary vortices for the lid-driven cavity problem up to Re=1000. The method may therefore, in many respects, be considered superior to similar ones on either uniform grids or nonuniform grids with transformation. Nonuniformity in grid, however, renders the algebraic system for the Poisson equations (for example, those associated with ψ) nonsymmetric, necessitating the use of hybrid BiCGStab algorithm instead of CG. We believe that the solution procedure does not lose much competitive edge because of this, as it uses smaller number of grid points which again may become significant at times in terms of saving memory. Since it is possible for the present method to place comparatively larger number of grid points in the boundary layer regions, it brings out some unreported features, for example, two new vortices in the much examined lid-driven cavity flow at Re=3200. The solution procedure is very robust and to our knowledge this is the first instance of extension of an HOC algorithm on nonuniform grid to the N-S equations, with or without grid-transformation. Also we believe that the present work, for the first time, effectively extends an HOC algorithm to Re's much beyond 1000 in the lid-driven cavity problem and beyond 200 in the backward-facing step problem. For the cavity, the method captures very accurate solutions including new flow features and for the step, our results at higher Re (600 to 800) are much closer to the experimental results compared with earlier investigations. Overall we consider the present method an important addition to the existing solution procedures for incompressible viscous flows.

Chapter 7

CONCLUSION

7.1 Observations and Remarks

This dissertation is concerned with HOC schemes for convection-diffusion equations in general and incompressible viscous flows in particular. New HOC finite difference algorithms are developed and some already existing ones modified for the 2D linear and nonlinear convection-diffusion equations. The new schemes are first tested on linear convection-diffusion problems to have an understanding of their mode of working, merits and demerits. All the schemes are then employed to different complex physical flow situations with or without heat and mass transfer to examine their accuracy, efficiency and robustness. Extensive validation exercise is carried out by comparing the results obtained from the schemes with existing analytical, numerical and experimental results. In what follows, first the work carried out in the thesis is described briefly so that insightful comments can be made on it later.

Scheme 1: An HOC scheme for the ψ-ω formulation of the N-S equations is combined with some new developments to solve the thermally driven cavity flow. These developments are in the shape of a compact $O(h^4)$ approximation for the first order derivative source term and a zero-gradient Neumann boundary condition of identical accuracy for temperature. The resultant method is termed *fully* HOC as the scheme, the boundary conditions and the source term treatment are all compact and fourth order accurate.

Scheme 2: A parametrized class of implicit HOC schemes are next developed for the 2D unsteady convection-diffusion equations with variable convection coefficients. The schemes are spatially fourth order accurate. They are temporally second or first order accurate and unconditionally stable depending on the choice of a weighted average parameter. The schemes are studied in great details bringing out interesting features like numerical diffusion and anti-diffusion exhibited by them. They are employed to a large number of problems of varying complexities with great success. Especially the $O[(\Delta t)^2]$ $(9,9)$ scheme is seen to compute transient solution of coupled nonlinear PDEs represented by the 2D N-S equations very effectively. The same scheme computes the steady solution (in a time-marching fashion) of two problems involving complex flows, namely, the lid-driven cavity flow and the double-diffusive flow in a vertical porous annulus. A large number of results are presented for a wide range of flow parameters and they compare very well with existing results.

Scheme 3: Also in a significant development, a transformation-free HOC finite difference scheme on nonuniform Cartesian grids is introduced. Conventional finite difference algorithms on nonuniform grids generally involve to-and-fro transformations between the physical and the computational spaces, bringing in a lot of additional complexities into the solution procedure especially in the context of HOC schemes. Against this, the present scheme uses a nonuniform grid, but no transformation! Its distinguishing feature is the simplicity of the underlying idea and high effectiveness in the computation of wall-bounded incompressible viscous flows, exemplified by the highly accurate and efficient coarse grid computation of flow in the lid-driven cavity and the backward-facing step problem at high Re's.

The work therefore, achieves with great success three major objectives set at the beginning, namely, development of some new HOC algorithms for computation of steady and unsteady viscous flows, modification of some existing ones to enhance their strength, and broadening the scope of applicability of

HOC schemes. In what follows the major achievements of the thesis will be highlighted in the form of observations and comments, further substantiating the claim of objectives having been achieved.

(i) The HOC treatment of the first order derivative source term by Scheme 1 can be easily extended to higher order derivatives making it possible to handle the pressure-Poisson equation in the primitive variable formulation of the N-S equations. The temperature boundary conditions developed for the adiabatic walls can be extended to any variable with zero normal gradient satisfying Laplace equation. These developments broaden the scope of applicability of HOC schemes.

(ii) Time accurate implicit schemes is an interesting area of research to which much research effort is currently being directed. However, HOC schemes for transient problems are seen only for linear convection-diffusion and there is a distinct void in this area. Scheme 2 developed here applies to general 2D convection-diffusion and can be considered a notable step in filling this void. Significantly, the scheme is also seen to have better time-wise efficiency compared to similar schemes and is therefore an important development.

(iii) The earlier HOC schemes all suffered from the debilitating constraint of having to use a grid aspect ratio of unity. Scheme 2 removes this constraint for the first time; Scheme 3 goes much beyond that by making it possible to use whatever nonuniform pattern of spacing one chooses in either direction –an important achievement indeed!

(iv) The only earlier HOC computation on a nonuniform grid is for a simple linear convection-diffusion problem through a transformation technique. In contrast, Scheme 3 produces remarkably accurate results on nonuniform grids for complex wall-bounded flows at high Re's. Multiplicity of scales at high Re's is known to pose a challenge to all computational methods. This is because, for near-wall small scales to be captured through an uniform grid, the number of points has to be so large as to go beyond the range of most of the ordinary computers. The scheme removes this hurdle to a great extent as it makes a much lower demand on memory. The solution procedure is so effective and accurate that for the much investigated lid-driven cavity, it captures some hitherto unreported flow features and for the backward-facing step flow problem, it produces results which are much closer to experimental compared with other numerical results. Elimination of transformation also results in marked simplicity. Clearly the method is a very important addition to the existing methods for computing incompressible viscous flows. Attempts have been initiated (see Appendix C) to extend the method to orthogonal curvilinear co-ordinates to enhance its power.

(vi) The robustness and versatility of the schemes can be realized from the accurate computation of viscous flows under complex situations represented, for instance, by high Rayleigh number, high Reynolds number, and buoyant flow driven by thermal and solutal gradients acting in opposition.

(v) For many of the difficult range of flow parameters, no earlier HOC result exist. For instance, for the lid-driven cavity flow, no earlier result beyond $Re = 10^3$ is seen whereas results included here are up to $Re = 7500$. For the thermally driven cavity flow again, no HOC result beyond $Ra = 10^5$ is seen whereas results for $Ra = 10^6$ and 10^7 are included in this thesis. For the double-diffusive flow in a porous annulus, some of the computations performed here for difficult range of flow parameters were not attempted earlier by any other method. It is thus seen that schemes developed in this work are put to severe tests not known to earlier HOC methods. The HOC computation of the double-diffusive flow in the porous annulus through Scheme 2 is perhaps the first instance of an HOC method being applied to a problem of both heat and mass transfer. This work thus broadens the range and scope of applicability of HOC schemes to a great extent.

(vii) Another point worth mentioning is that throughout the present work, advanced iterative solvers like CG, BiCG, BiCGStab and hybrid BICGStab are extensively used to solve the discrete algebraic systems. This appears to have added strength to the methods as computation in some complex flow situations are accomplished without much difficulty.

7.2 Scope for Future Work

The work also opens up a host of interesting research possibilities, the major ones of which are listed below.

1. As mentioned earlier, this work makes it possible to handle the pressure-Poisson equation arising in the primitive variable form of N-S equations. This opens up the possibility of efficient solution of 3D incompressible N-S equations through HOC schemes.

2. All the HOC schemes in this work have been applied only to incompressible viscous flow problems. It will be worthwhile to examine to what extent the strategy of using the original PDE to construct HOC schemes can be used in relation with compressible flows.

3. The transient $(9, 9)$ scheme is spatially fourth and temporally second order accurate. Whether the scheme in some modified form can be extended to direct numerical simulation (DNS) of turbulent flows seems to be an interesting and important area of research.

4. Preliminary work of extension of Scheme 3 to orthogonal curvilinear system of co-ordinates has already been included in Appendix C. The idea appears to have good potential for efficient computation of physically meaningful flows like incompressible viscous flow past a cylinder. Future work in this direction seems to be fraught with interesting possibilities.

5. Because of the presence of the four corner points in the 9-point stencil for the transient scheme (Scheme 2), it was found difficult to adopt an alternate direction implicit (ADI) strategy. Whether this hurdle can be removed and an efficient HOC scheme can be constructed is another idea worth pursuing.

Appendix A

Stability analysis of the transient HOC scheme

As described in section 4.3 in Chapter 4, the amplification factor ξ can be found by substituting the expression for ϕ_{ij}^{n} and ϕ_{ij}^{n+1} in equation (4.11) whereby

$$\xi = \frac{(a_1 + Ib_1) + (a_2 + Ib_2)}{(a_1 + Ib_1)} \qquad (I = \sqrt{-1}) \tag{A.1}$$

with

$$\begin{aligned} a_1 &= \mu \left[-\frac{\Lambda_1 + \Lambda_2}{2} \left(\frac{2}{3} \cos\theta_x \cos\theta_y + \frac{\gamma h k}{c} \sin\theta_x \sin\theta_y \right) \right. \\ &+ 2 \left(\frac{\Lambda_1 + \Lambda_2}{6} - \Lambda_1 \alpha \right) \cos\theta_x + 2 \left(\frac{\Lambda_1 + \Lambda_2}{6} - \Lambda_2 \beta \right) \cos\theta_y \\ &+ \left. \left(2\Lambda_1 \alpha + 2\Lambda_2 \beta - \frac{\Lambda_1 + \Lambda_2}{3} \right) \right] + b \left(\frac{\cos\theta_x + \cos\theta_y}{6} + \frac{2}{3} \right) \end{aligned} \tag{A.2}$$

$$\begin{aligned} a_2 &= \frac{\Lambda_1 + \Lambda_2}{2} \left(\frac{2}{3} \cos\theta_x \cos\theta_y + \frac{\gamma h k}{c} \sin\theta_x \sin\theta_y \right) \\ &- 2 \left(\frac{\Lambda_1 + \Lambda_2}{6} - \Lambda_1 \alpha \right) \cos\theta_x - 2 \left(\frac{\Lambda_1 + \Lambda_2}{6} - \Lambda_2 \beta \right) \cos\theta_y, \\ &+ \left(2\Lambda_1 \alpha + 2\Lambda_2 \beta - \frac{\Lambda_1 + \Lambda_2}{3} \right) \end{aligned} \tag{A.3}$$

$$\begin{aligned} b_1 &= \mu\left[\frac{\Lambda_1+\Lambda_2}{6}\left(hc\sin\theta_x\cos\theta_y+kd\cos\theta_x\sin\theta_y\right)+\Lambda_1 h\left(C-\frac{c}{3}\right)\sin\theta_x\right.\\ &+ \left.\Lambda_2 k\left(D-\frac{d}{3}\right)\sin\theta_y\right]-\frac{b}{12}\left(hc\sin\theta_x+kd\sin\theta_y\right) \end{aligned} \tag{A.4}$$

$$\begin{aligned} b_2 &= -\frac{\Lambda_1+\Lambda_2}{6}\left(hc\sin\theta_x\cos\theta_y+kd\cos\theta_x\sin\theta_y\right)-\Lambda_1 h\left(C-\frac{c}{3}\right)\sin\theta_x\\ &- \Lambda_2 k\left(D-\frac{d}{3}\right)\sin\theta_y \end{aligned} \tag{A.5}$$

so that

$$a_1=-\mu a_2+b\left(\frac{\cos\theta_x+\cos\theta_y}{6}+\frac{2}{3}\right), \tag{A.6}$$

and

$$b_1=-\mu b_2-\frac{b}{12}\left(hc\sin\theta_x+kd\sin\theta_y\right) \tag{A.7}$$

Therefore using equation (A.1) and the stability criterion $|\xi^2|-1\leq 1$, we get

$$\left(1+\frac{a_1a_2-b_1b_2}{a_1^2+b_1^2}\right)^2+\left(\frac{a_1b_2+a_2b_1}{a_1^2+b_1^2}\right)^2-1\leq 1,$$

ie.,

$$a_2^2+b_2^2+2\left(a_1a_2-b_1b_2\right)\leq 0$$

or

$$(1-2\mu)\left(a_2^2-b_2^2\right)+2\left[a_2\left(\frac{\cos\theta_x+\cos\theta_y}{6}+\frac{2}{3}\right)+\frac{bb_2}{12}\left(hc\sin\theta_x+kd\sin\theta_y\right)\right]\leq 0 \tag{A.8}$$

Now, ξ has its strictest stability restriction when $\cos\theta_x=\cos\theta_y=-1$. Also $C=c$, $D=d$, $\alpha=1+\dfrac{h^2c^2}{12}$ and $\beta=1+\dfrac{k^2d^2}{12}$ when c and d are constants. Using these facts in the expressions for a_2 and b_2, equation (A.8) after some simplifications yield the relation (4.13) given by

$$(1-2\mu)\leq\frac{2b}{\Lambda_1(8+h^2c^2)+\Lambda_2(8+k^2d^2)}.$$

Appendix B

Details of finite difference operators

The expressions for the finite difference operators appearing in the equations (6.10), (6.17) and (6.19)-(6.24) in Chapter 6 are as follows

$$\delta_x \phi_{ij} = \frac{\phi_{i+1,j} - \phi_{i-1,j}}{2h} \tag{B.1}$$

$$\delta_y \phi_{ij} = \frac{\phi_{i,j+1} - \phi_{i,j-1}}{2k} \tag{B.2}$$

$$\delta_x^2 \phi_{ij} = \frac{1}{h} \left\{ \frac{\phi_{i+1,j}}{x_f} - \left(\frac{1}{x_f} + \frac{1}{x_b} \right) \phi_{ij} + \frac{\phi_{i-1,j}}{x_b} \right\} \tag{B.3}$$

$$\delta_y^2 \phi_{ij} = \frac{1}{k} \left\{ \frac{\phi_{i,j+1}}{y_f} - \left(\frac{1}{y_f} + \frac{1}{y_b} \right) \phi_{ij} + \frac{\phi_{i,j-1}}{y_b} \right\} \tag{B.4}$$

$$\delta_x \delta_y \phi_{ij} = \frac{1}{4hk} \left(\phi_{i+1,j+1} - \phi_{i+1,j-1} - \phi_{i-1,j+1} + \phi_{i-1,j-1} \right) \tag{B.5}$$

$$\begin{aligned} \delta_x \delta_y^2 &= \frac{1}{2hk} \left\{ \frac{1}{y_f} \left(\phi_{i+1,j+1} - \phi_{i-1,j+1} \right) - \left(\frac{1}{y_f} + \frac{1}{y_b} \right) \left(\phi_{i+1,j} - \phi_{i-1,j} \right) \right. \\ &+ \left. \frac{1}{y_b} \left(\phi_{i+1,j-1} - \phi_{i-1,j-1} \right) \right\} \end{aligned} \tag{B.6}$$

$$\begin{aligned} \delta_x^2 \delta_y &= \frac{1}{2hk} \left\{ \frac{1}{x_f} \left(\phi_{i+1,j+1} - \phi_{i+1,j-1} \right) - \left(\frac{1}{x_f} + \frac{1}{x_b} \right) \left(\phi_{i,j+1} - \phi_{i,j-1} \right) \right. \\ &+ \left. \frac{1}{x_b} \left(\phi_{i-1,j+1} - \phi_{i-1,j-1} \right) \right\} \end{aligned} \tag{B.7}$$

$$\begin{aligned}
\delta_x^2\delta_y^2\phi_{ij} &= \frac{1}{hk}\left\{\frac{\phi_{i+1,j+1}}{x_f y_f} + \frac{\phi_{i-1,j+1}}{x_b y_f} - \left(\frac{1}{x_f y_f} + \frac{1}{x_b y_f}\right)\phi_{i,j+1}\right. \\
&- \left(\frac{1}{x_f y_f} + \frac{1}{x_f y_b}\right)\phi_{i+1,j} + \left(\frac{1}{x_f y_f} + \frac{1}{x_f y_b} + \frac{1}{x_b y_f} + \frac{1}{x_b y_b}\right)\phi_{ij} \\
&- \left.\left(\frac{1}{x_f y_b} + \frac{1}{x_b y_b}\right)\phi_{i,j-1} - \left(\frac{1}{x_b y_f} + \frac{1}{x_b y_b}\right)\phi_{i-1,j} + \frac{\phi_{i+1,j-1}}{x_f y_b} + \frac{\phi_{i-1,j-1}}{x_b y_b}\right\}
\end{aligned} \tag{B.8}$$

where x_f, x_b, y_f and y_b are as defined in section 6.2 of Chapter 6 and $h = \dfrac{x_f + x_b}{2}$ and $k = \dfrac{y_f + y_b}{2}$.

When $x_f = x_b = h$ and $y_f = y_b = k$, these become the operators appearing in equations (4.3)-(4.10) of Chapter 4 and on setting $x_f = x_b = y_f = y_b = h$, they reduce to the operators appearing in equations (2.4) and (2.12)-(2.18) of Chapter 2.

Appendix C

Extension of nonuniform HOC methodology to Curvilinear Co-ordinates

So far, the present dissertation has dealt only with rectangular Cartesian co-ordinates; however, it is possible to extend the HOC methodology on nonuniform grids developed in Chapter 6 to orthogonal curvilinear co-ordinates as well. An HOC formulation is developed here on a curvilinear co-ordinate system without transformation. The procedure is briefly described below:

The convection-diffusion equation for a transport variable ϕ in 2D general orthogonal curvilinear co-ordinates (s, n) may be written as

$$-a(s,n)\frac{\partial^2 \phi}{\partial s^2} - b(s,n)\frac{\partial^2 \phi}{\partial n^2} + c(s,n)\frac{\partial \phi}{\partial s} + d(s,n)\frac{\partial \phi}{\partial n} = f(s,n) \qquad \text{(C.1)}$$

It is worth mentioning that unlike the earlier HOC formulation for 2D convection-diffusion, the diffusion coefficients a and b in the present case are variables as in most of the curvilinear cases (e.g. the polar co-ordinates) one is likely to come across at least one variable diffusion coefficient. The HOC formulation for this on nonuniform grids with forward and backward steplengths Δs_f, Δs_b in s- and Δn_f, Δn_b in n-directions may be written as

$$\begin{aligned}&\Big[-A_{ij}\delta_s^2 - B_{ij}\delta_n^2 + C_{ij}\delta_s + D_{ij}\delta_n \\ +\ & G_{ij}\delta_s\delta_n - H_{ij}\delta_s\delta_n^2 - K_{ij}\delta_s^2\delta_n - L_{ij}\delta_s^2\delta_n^2\Big]\,\phi_{ij} = F_{ij},\end{aligned} \tag{C.2}$$

where the coefficients C_{ij}, D_{ij}, A_{ij}, B_{ij}, G_{ij}, H_{ij}, K_{ij} and L_{ij} are given by

$$\begin{aligned}C_{ij} &= \Big[1 + \frac{1}{a}(H_1 - \alpha H_2)\delta_s + \frac{1}{b}(K_1 - \beta K_2)\delta_n \\ &+ \frac{1}{a}\left\{H_2 - 0.5(s_f - s_b)(H_1 - \alpha H_2)\right\}\delta_s^2 \\ &+ \frac{1}{b}\left\{K_2 - 0.5(n_f - n_b)(K_1 - \beta K_2)\right\}\delta_n^2\Big]\,c,\end{aligned} \tag{C.3}$$

$$\begin{aligned}D_{ij} &= \Big[1 + \frac{1}{a}(H_1 - \alpha H_2)\delta_s + \frac{1}{b}(K_1 - \beta K_2)\delta_n \\ &+ \frac{1}{a}\left\{H_2 - 0.5(s_f - s_b)(H_1 - \alpha H_2)\right\}\delta_s^2 \\ &+ \frac{1}{b}\left\{K_2 - 0.5(n_f - n_b)(K_1 - \beta K_2)\right\}\delta_n^2\Big]\,d,\end{aligned} \tag{C.4}$$

$$\begin{aligned}A_{ij} = a &+ \Big[\frac{1}{a}(H_1 - \alpha H_2)\left\{\delta_s a - 0.5(s_f - s_b)\delta_s^2 a - c\right\} \\ &+ \frac{1}{b}(K_1 - \beta K_2)\left\{\delta_n a - 0.5(n_f - n_b)\delta_n^2 a\right\} + \left(\frac{H_2}{a}\delta_s^2 a + \frac{K_2}{b}\delta_n^2 a\right) \\ &- 2\frac{H_2}{a}\left\{\delta_s c - 0.5(s_f - s_b)\delta_s^2 c\right\}\Big] + 0.5(s_f - s_b)C_{ij},\end{aligned} \tag{C.5}$$

$$\begin{aligned}B_{ij} = b &+ \Big[\frac{1}{a}(H_1 - \alpha H_2)\left\{\delta_s b - 0.5(s_f - s_b)\delta_s^2 b\right\} \\ &+ \frac{1}{b}(K_1 - \beta K_2)\left\{\delta_n b - 0.5(n_f - n_b)\delta_n^2 b - d\right\} + \left(\frac{H_2}{a}\delta_s^2 b + \frac{K_2}{b}\delta_n^2 b\right) \\ &- 2\frac{K_2}{b}\left\{\delta_n d - 0.5(n_f - n_b)\delta_n^2 d\right\}\Big] + 0.5(n_f - n_b)D_{ij},\end{aligned} \tag{C.6}$$

$$\begin{aligned}G_{ij} &= \frac{1}{a}(H_1 - \alpha H_2)d + \frac{1}{b}(K_1 - \beta K_2)c + 2\frac{H_2}{a}\left\{\delta_s d - 0.5(s_f - s_b)\delta_s^2 d\right\} \\ &+ 2\frac{K_2}{b}\left\{\delta_n c - 0.5(n_f - n_b)\delta_n^2 c\right\},\end{aligned} \tag{C.7}$$

$$H_{ij} = \frac{1}{a}(H_1 - \alpha H_2)b + 2\frac{H_2}{a}\left\{\delta_s b - 0.5(s_f - s_b)\delta_s^2 b\right\} - \frac{1}{b}K_2 c, \tag{C.8}$$

$$K_{ij} = \frac{1}{b}(K_1 - \alpha K_2)a + 2\frac{K_2}{b}\left\{\delta_n a - 0.5(n_f - n_b)\delta_n^2 a\right\} - \frac{1}{a}H_2 d, \tag{C.9}$$

$$L_{ij} = \frac{b}{a}H_2 + \frac{a}{b}K_2 \tag{C.10}$$

and

$$\begin{aligned} F_{ij} &= \left[1 + \frac{1}{a}(H_1 - \alpha H_2)\delta_s + \frac{1}{b}(K_1 - \beta K_2)\delta_n \right.\\ &+ \frac{1}{a}\left\{H_2 - 0.5(s_f - s_b)(H_1 - \alpha H_2)\right\}\delta_s^2 \\ &+ \left.\frac{1}{b}\left\{K_2 - 0.5(n_f - n_b)(K_1 - \beta K_2)\right\}\delta_n^2\right] f, \end{aligned} \tag{C.11}$$

with

$$\alpha = \frac{1}{a}\left[2\left\{\delta_s a - 0.5(s_f - s_b)\delta_s^2 a\right\} - c\right], \quad \beta = \frac{1}{a}\left[2\left\{\delta_n b - 0.5(n_f - n_b)\delta_n^2 b\right\} - d\right],$$

$$H_1 = \frac{1}{6}\left\{2a(s_f - s_b) - c s_f s_b\right\}, \quad H_2 = \frac{a}{12}\left(s_f^2 + s_b^2 - s_f s_b\right),$$

$$K_1 = \frac{1}{6}\left\{2b(n_f - n_b) - d n_f n_b\right\} \quad \text{and} \quad K_2 = \frac{b}{12}\left(n_f^2 + n_b^2 - n_f n_b\right).$$

We have already applied this on small problems in polar co-ordinates with moderate success. Further research is required to completely establish the scheme which is beyond the scope of this dissertation and can go a long way in efficiently solving incompressible viscous fluid flows in curvilinear co-ordinates as well.

Bibliography

[1] S. Abarbanel and A. Kumar. Compact higher-order schemes for the Euler equations. *Journal of Scientific Computing*, 3:275–288, 1988.

[2] F. Alavyoon. On natural convection in vertical porous annulus due to prescribed fluxes of heat and mass at the vertical boundaries. *International Journal for Heat Mass Transfer*, 36:2479–2498, 1993.

[3] F. Alavyoon, Y. Masuda, and S. Kimura. On natural convection in vertical porous annulus due to opposing fluxes of heat and mass prescribed at the vertical boundaries. *International Journal for Heat Mass Transfer*, 36:195–206, 1994.

[4] U. Ananthakrishnaiah, R. Monahar, and J. W. Stephenson. Fourth-order finite difference methods for three-dimensional general linear elliptic problems with variable coefficients. *Numerical Methods for Partial Differential Equations*, 3:229–240, 1987.

[5] D. A. Anderson, J. C. Tannehil, and R. H. Pletcher. *Computational Fluid mechanics and Heat Transfer*. Hemisphere Publishing Corporation, New York, 1984.

[6] J. D. Anderson, Jr. *Computational Fluid Dynamics*. McGraw-Hill, Inc., New York, 1995.

[7] B. F. Armaly, F. Durst, J. C. Pereira, and B. Schönung. Experimental and theoritical investigation of backward facing step flow. *Journal of Fluid Mechanics*, 127:473–496, 1983.

[8] K. S. Ball and D. C. Kuo. Spectral simulation of thermal convection using a vorticity-velocity formulation. *Journal of Heat Transfer*, 2:313–318, 1994.

[9] A. Balzano. Mosquito: An efficient finite difference scheme for numerical simulation of 2D advection. *International Journal for Numerical Methods in Fluids*, 31:481–496, 1999.

[10] H. Beji, R. Bennacer, R. Duval, and P. Vasseur. Double-diffusive natural convection in vertical porous annulus. *Numerical Heat Transfer*, 36:153–170, 1999.

[11] R. Bodenmann and H. J. Schroll. Higher order discretization of initial boundary value problems for mixed systems. In *Proceedings Seminar für Angewandte Mathematik, ETH-Zurick*, number 96-05, May 1996.

[12] Charles-Henri Bruneau and Claude Jouron. An efficient scheme for solving steady incompressible Navier-Stokes equations. *Journal of Computational Physics*, 89:389–413, 1990.

[13] Y. Chen, S. Yang, and J. Yang. Implicit weighted essentially non-oscillatory schemes for the incompressible Navier-Stokes equations. *International Journal for Numerical Methods in Fluids*, 31:747–765, 1999.

[14] D. R. Chenoweth and S. Paolucci. Natural convection in an enclosed vertical air layer with large horizontal temperature differences. *Journal of Fluid Mechanics*, 169:173–210, 1986.

[15] A. J. Chorin. Numerical solution of the Navier-Stokes equation. *Mathematics of Computation*, 22:747–762, 1968.

[16] G. Comini, G. Cortella, and M. Manzan. A stream function-vorticity based finite element formulation for laminar convection problems. *Numerical Heat Transfer*, 28:1–22, 1995.

[17] D. C. Dalal, N. Datta, and S. K. Mukherjea. Unsteady natural convection of a dusty fluid in an infinite rectangular channel. *International Journal for Heat Mass Transfer*, 41(3):547–562, 1998.

[18] G. De Vahl Davis. Natural convection in a square cavity: A benchmark numerical solution. *International Journal for Numerical Methods in Fluids*, 3:249–264, 1983.

[19] G. De Vahl Davis and I. P. Jones. Natural convection in a square cavity: A comparison exercise. *International Journal for Numerical Methods in Fluids*, 3(1):227–248, 1983.

[20] S. C. R. Dennis and J. D. Hudson. Compact h^4 finite difference approximations to operators of Navier-Stokes type. *Journal of Computational Physics*, 85:390–416, 1989.

[21] J. K. Dukowicz and J. D. Ramshaw. Tensor viscosity method for convection in numerical fluid dynamics. *Journal of Computational Physics*, 32:71–79, 1979.

[22] E. C. Gartland, Jr. Discrete weighted mean approximation of a model convection-diffusin equation. *SIAM Journal on Scientific and Statistical Computing*, 3(4):460–472, 1982.

[23] D. K. Gartling. A test problem for outflow boundary conditions-flow over a backward facing step. *International Journal for Numerical Methods in Fluids*, 11:953–967, 1990.

[24] U. Ghia, K. N. Ghia, and C. T. Shin. High-Re solutions for incompressible flow using the Navier-Stokes equation and a multigrid method. *Journal of Computational Physics*, 48:387–411, 1982.

[25] M. M. Gupta and J. Koutchou. Symbolic derivation of finite difference approximations to three dimensional poisson equation. *Numerical Methods for Partial Differential Equations*, 18(5):593–606, 1998.

[26] M. M. Gupta, R. M. Manohar, and J. H. Stephenson. A single cell high order scheme for the convection-diffusion with variable coefficients. *International Journal for Numerical Methods in Fluids*, 4:641–651, 1984.

[27] M. A. Havstad and P. J. Burns. Convective heat transfer in a vertical cylindrical annuli filled with a porous medium. *International Journal for Heat Mass Transfer*, 25:1755–1766, 1982.

[28] R. S. Hirsh. Higher order accurate solution of fluid mechanics problems by a compact differencing technique. *Journal of Computational Physics*, 9:90–109, 1975.

[29] C. J. Ho and F. H. Lin. Simulation of natural convection in a vertical enclosure by using a new incompressible flow formulation- pseudovorticity-velocity formulation. *Numerical Heat Transfer*, 31:881–896, 1997.

[30] J. D. Hoffman. *Numerical methods for Engineers and Scientiests.* McGraw-Hill, Inc., Singapore, 1993.

[31] M. Hortmann, M. Peric, and G. Scheure. Finite volume multigrid prediction of laminar natural convection: benchmark solutions. *International Journal for Numerical Methods in Fluids*, 11:189–207, 1990.

[32] R. J. A. Janssen and R. A. W. M. Henkes. Accuracy of finite volume discretizations for bifurcating natural convection in a square cavity. *Numerical Heat Transfer*, 24:191–207, 1993.

[33] J. John. Evaluation of FIDAP on some classical laminar and turbulent benchmarks. *International Journal for Numerical Methods in Fluids*, 8:1469–1490, 1988.

[34] Jiten C. Kalita, D. C. Dalal, and Anoop K. Dass. Fully compact higher-order computation of steady-state natural convection in a square cavity. *Physical Review E*, 64(6):066703 (1–13), 2001.

[35] Jiten C. Kalita, D. C. Dalal, and Anoop K. Dass. A class of Higher Order Compact schemes for the unsteady two-dimensional convection-diffusion equation with variable coefficients. *International Journal for Numerical Methods in Fluids*, 38(12):1111–1131, 2002.

[36] Jiten C. Kalita, Anoop K. Dass, and D. C. Dalal. An HOC scheme for steady convection-diffusion for nonuniform grids without transformation. *Journal of Computational Physics*, (revision under review).

[37] C. T. Kelley. *Iterative methods for linear and nonlinear equations.* SIAM Publications, Philadelphia, 1995.

[38] J. Kim and P. Moin. Application of fractional step method to incompressible Navier-Stokes equations. *Journal of Computational Physics*, 59:308–323, 1985.

[39] S. K. Lele. Compact finite difference schemes with spectral like resolution. *Journal of Computational Physics*, 103:16–42, 1992.

[40] M. Li, T. Tang, and B. Fornberg. A compact fourth order finite difference scheme for the steady incompressible Navier-Stokes equations. *International Journal for Numerical Methods in Fluids*, 20:1137–1151, 1995.

[41] R. J. Mackinnon and G. F. Carey. Analysis of material interface discontinuities and superconvergent fluxes in finite difference theory. *Journal of Computational Physics*, 75(1):151–167, 1988.

[42] R. J. Mackinnon and R. W. Johnson. Differential equation based representation of truncation errors for accurate numerical simulation. *International Journal for Numerical Methods in Fluids*, 13:739–757, 1991.

[43] M. Mamou, P. Vasseur, and E. Bilgen. Multiple solutions for double-diffusive convection in vertical porous annulus. *International Journal for Heat Mass Transfer*, 38(10):1787–1798, 1995.

[44] M. Marcoux, M.-C. Charrier-Mojtabi, and M. Azaiez. Double-diffusive convection in annular vertical porous layer. *International Journal for Heat Mass Transfer*, 42:2313–2325, 1999.

[45] B. J. Noye and H. H. Tan. A third order semi implicit method for solving the one-dimensional convection-diffusion equation. *International Journal for Numerical Methods in Engineering*, 26:1615–1629, 1988.

[46] B. J. Noye and H. H. Tan. Finite difference methods for solving two-dimensional advection diffusion equation. *International Journal for Numerical Methods in Fluids*, 9:75–98, 1989.

[47] S. Patankar. *Numerical Heat Transfer and Fluid Flow.* Hemisphere Publishing Corporation, New York, 1980.

[48] V. Prasad and F. A. Kulacki. Natural convection in a vertical porous annulus. *International Journal for Heat Mass Transfer*, 27(2):207–219, 1984.

[49] V. Prasad and F. A. Kulacki. Natural convection in porous media bounded by short concentric vertical cylinders. *International Journal for Heat Mass Transfer*, 107:147–154, 1985.

[50] V. Prasad, F. A. Kulacki, and M. Keyhani. Natural convection in porous media. *Journal of Fluid Mechanics*, 150:89–119, 1985.

[51] V. Prasad, F. A. Kulacki, and A. V. Kulkarni. Free convection in a vertical, porous annulus with constant heat flux on the inner wall-experimental results. *International Journal for Heat Mass Transfer*, 29:713–723, 1986.

[52] P. Le Quéré. Accurate solutions to the square thermally driven cavity at high Rayleigh numbers. *Computers and Fluids*, 1:29–41, 1991.

[53] M. M. Rai and P. Moin. Direct simulations of turbulent flow using finite difference schemes. *Journal of Computational Physics*, 96:15–53, 1991.

[54] B. Ramaswamy, T. C. Jue, and J. E. Akin. Finite element analysis of oscillatory flow with heat transfer inside a square cavity. *AIAA Journal*, 30:412–421, 1992.

[55] D. C. Reda. Natural convection experiments in a liquid saturated porous medium bounded by vertical coaxial cylinders. *Journal of Heat Transfer*, 105:795–802, 1983.

[56] P. Roache. *Computational Fluid Dynamics.* Hermosa Press, NM, 1972.

[57] T. Saitoh and K. Hirosh. High accuracy benchmark solutins to natural convection in a square cavity. *Computational Mechanics*, 4:417–427, 1989.

[58] R. Schreiber and H. B. Keller. Driven cavity flow by efficient numerical techniques. *Journal of Computational Physics*, 49:310–333, 1983.

[59] Jörn Sesterhenn. A characteristic-type formulation of the Navier-Stokes equations for high order upwind schemes. *Computers and Fluids*, 30(1):37–68, 2001.

[60] P. W. Shipp, M. Shoukri, and M. B. Carver. Double-diffusive natural convection in a closed annulus. *Numerical Heat Transfer*, 24:339–356, 1993.

[61] P. W. Shipp, M. Shoukri, and M. B. Carver. Effect of thermal Rayleigh and Lewis numbers on double-diffusive natural convection in a closed annulus. *Numerical Heat Transfer*, 24:451–465, 1993.

[62] G. L. G. Sleijpen and H. A. van der Vorst. Hybrid bi-conjugate gradient methods for CFD problems. *Computational Fluid Dynamics Review*, pages 457–476, 1995.

[63] G. D. Smith. *Numerical solutions of partial differential equations: finite difference methods.* Clarendon Press, Oxford, 1984.

[64] W. F. Spotz. Accuracy and performance of numerical wall boundary conditions for the 2D incompressible stream-function vorticity. *International Journal for Numerical Methods in Fluids*, 28:737–757, 1998.

[65] W. F. Spotz. *High order compact finite difference schemes for computational mechanics.* PhD thesis, University of Texas at Austin, December, 1995.

[66] W. F. Spotz and G. F. Carey. High Order Compact Finite Difference Methods with Applications to Viscous Flows. Technical Report 94-03, Texas institute of Computational and applied mechanics, The university of Texas at Austin, 1994.

[67] W. F. Spotz and G. F. Carey. High-order compact scheme for the steady stream-function vorticity equations. *International Journal for Numerical Methods in Engineering*, 38:3497–3512, 1995.

[68] W. F. Spotz and G. F. Carey. A high-order compact formulation for the 3D Poisson equation. *Numerical Methods for Partial Differential Equations*, 12:235–243, 1996.

[69] W. F. Spotz and G. F. Carey. Formulation and experiments with high-order compact schemes for nonuniform grids. *International Journal of Heat and Fluid Flow*, 8(3):288–303, 1998.

[70] K. Srinivasan and S. G. Rubin. Segmented multigrid domain decomposition procedure for incompressible viscous flows. *International Journal for Numerical Methods in Fluids*, 15:1333–1355, 1992.

[71] J. C. Strikwerda. High-order accurate schemes for incompressible viscous flow. *International Journal for Numerical Methods in Fluids*, 24:715–734, 1997.

[72] Toshio Tagawa and Hiroyuki Ozoe. Effect of Prendtl number and computational schemes on the oscillatory natural convection in an enclosure. *Numerical Heat Transfer*, 30:272–282, 1996.

[73] Osvair V. Trevisan and Adrian Bejan. Natural convection with combined heat and mass transfer buoyancy effects in a porous medium. *International Journal for Heat Mass Transfer*, 28:1597–1611, 1985.

[74] Osvair V. Trevisan and Adrian Bejan. Mass and heat transfer by natural convection in a vertical slot filled with porous medium. *International Journal for Heat Mass Transfer*, 29(3):403–415, 1986.

[75] J. O. Wilkes and S. W. Churchill. The finite difference computation of natural convection in a rectangular enclosure. *AIChE Journal*, 12:161–166, 1966.

[76] J. O. Wilkes and C. P. Thomson. An evaluation of higher-order upwind differencing for elliptic flow problems. In *In proceedings of the Third International Conference on Numerical Methods for Laminar and Turbulent Flows*, pages 248–257, 1983.

[77] H. H. Wong and G. D. Raithby. Improved finite difference methods based on a critical evaluation of the approximation errors. *Numerical Heat Transfer*, 2:139–163, 1979.

[78] M. Yanwen, F. Dexun, T. Kobayashi, and N. Taniguchi. Numerical solution of the incompressible Navier-Stokes equations with an upwind compact difference scheme. *International Journal for Numerical Methods in Fluids*, 30:509–521, 1999.

[79] J. Zhang. An explicit fourth-order compact finite difference scheme for three dimensional convection-diffusion. *Communication in Numerical Methods for Engineering*, 14:209–214, 1998.